CCMS-93-15
VPI-E-93-09

CENTER FOR COMPOSITE MATERIALS AND STRUCTURES

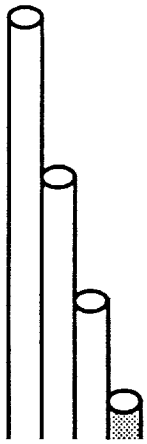

Verification of a Two-Dimensional Infiltration Model for the Resin Transfer Molding Process

Vincent H. Hammond
Alfred C. Loos
H. Benson Dexter
Gregory H. Hasko

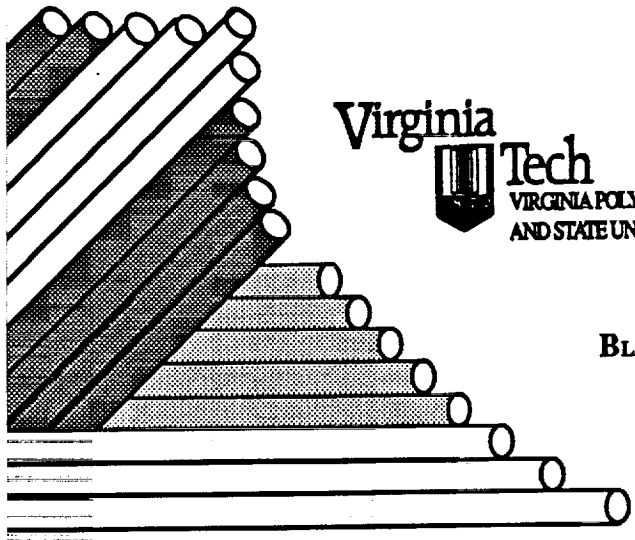

Virginia Tech
VIRGINIA POLYTECHNIC INSTITUTE AND STATE UNIVERSITY

BLACKSBURG, VIRGINIA
24061

August 1993

College of Engineering
Virginia Polytechnic Institute and State University
Blacksburg, Virginia 24061

August 1993

CCMS-93-15
VPI-E-93-09

Verification of a Two-Dimensional Infiltration Model for the Resin Transfer Molding Process

Vincent H. Hammond[1]
Alfred C. Loos[2]
H. Benson Dexter[3]
Gregory H. Hasko[4]

Department of Engineering Science and Mechanics

NASA Grant NAG-1-343

Interim Report 94

The NASA-Virginia Tech Composites Program

Prepared for: Polymeric Materials Branch
National Aeronautics and Space Administration
Langley Research Center
Hampton, VA 23681-0001

---

1. Graduate Research Assistant, Department of Engineering Science and Mechanics, Virginia Polytechnic Institute and State University
2. Associate Professor, Department of Engineering Science and Mechanics, Virginia Polytechnic Institute and State University
3. Senior Materials Research Engineer, Polymeric Materials Branch, NASA Langley Research Center, Hampton, VA
4. Principal Engineer, Lockheed Engineering and Sciences Company, Hampton, VA

ABSTRACT

A two-dimensional finite element model for the infiltration of a dry textile preform by an injected resin has been verified. The model, which is based on the finite element/control volume technique, determines the total infiltration time and the pressure increase at the mold inlet associated with the RTM process. Important input data for the model are the compaction and permeability behavior of the preform along with the kinetic and rheological behavior of the resin.

The compaction behavior for several textile preforms was determined by experimental methods. A power law regression model was used to relate fiber volume fraction to the applied compaction pressure. Results showed a large increase in fiber volume fraction with the initial application of pressure. However, as the maximum fiber volume fraction was approached, the amount of compaction pressure required to decrease the porosity of the preform rapidly increased.

Similarly, a power law regression model was used to relate permeability to the fiber volume fraction of the preform. Two methods were used to measure the permeability of the textile preform. The first, known as the steady state method, measures the permeability of a saturated preform under constant flow rate conditions. The second, denoted the advancing front method, determines the permeability of a dry preform to an infiltrating fluid. Water, corn oil, and an epoxy resin, Epon 815, were used to determine the effect of fluid type and viscosity on the steady state permeability behavior of the preform. Permeability values measured with the different fluids showed that fluid viscosity had no influence on the permeability behavior of 162 E-glass and TTI IM7/8HS preforms.

Permeabilities measured from steady state and advancing front experiments for the

warp direction of 162 E-glass fabric were similar. This behavior was noticed for tests conducted with corn oil and Epon 815. Comparable behavior was observed for the warp direction of the TTI IM7/8HS preform and corn oil.

Fluid/fiber interaction was measured through the use of the single fiber pull-out test. The surface tension of both the corn oil and Epon 815 was determined. The contact angle between these two fluids and glass and carbon fibers was also measured. These tests indicated that the glass fiber had a lower contact angle than the carbon fiber and therefore is wet out better than the carbon fiber by both fluids. This result is attributed to the sizing commonly used on the carbon fibers.

Mold filling and flow visualization experiments were performed to verify the analytical computer model. Frequency dependent electromagnetic sensors were used to monitor the resin flow front as a function of time. For the flow visualization tests, a video camera and high resolution tape recorder were used to record the experimental flow fronts. Comparisons between experimental and model predicted flow fronts agreed well for all tests. For the mold filling tests conducted at constant flow rate injection, the model was able to accurately predict the pressure increase at the mold inlet during the infiltration process. A kinetics model developed to predict the degree of cure as a function of time for the injected resin accurately calculated the increase in the degree of cure during the subsequent cure cycle.

ACKNOWLEDGEMENTS

The financial support of this research by NASA Langley Research Center through grant NAG-1-343 is greatly appreciated.

TABLE OF CONTENTS

LIST OF FIGURES

LIST OF TABLES

1.0 INTRODUCTION

In recent years, Resin Transfer Molding (RTM) has become a popular processing technique for the manufacture of composite structures, particularly in the aerospace and automotive industries. One reason for this increase in popularity is the ability to manufacture complex shape high performance composite structures near net shape and with little, if any, surface finishing necessary. By using foam cores, full three-dimensional parts may be produced. Because it is a low pressure operation, large components can be manufactured with low tonnage presses. Another attractive feature of RTM is the low cost associated with the initial capital investments along with the low cost of parts and labor.

There are several variants to the RTM process. The main variants are Pressure Injection RTM, Vacuum-Assisted Resin Injection (VARI), Preform Molding, Structural Reaction Injection Molding (SRIM), and High-Speed Resin Transfer Molding (HSRTM) [1]. Since the Pressure Injection RTM process was used in this study, a short description of it is provided.

In the Pressure Injection RTM process, the preform or a stack of individual fabric plies is placed with the desired fiber orientation into a matched cavity mold. The thermosetting resin system is then injected into the mold through one or more inlet ports using high injection pressures. If desired, a vacuum is applied to aid in the removal of air from the fiber bed in order to reduce void content. After the fiber bed is saturated by the resin, the required cure cycle is applied to cure the resin matrix and produce the final part.

Due to the many variables involved in the RTM process - resin viscosity, preform permeability, resin/preform interaction, and port location - an iterative approach

would be extremely costly in determining such details as optimum port location, time required to fully saturate the preform, and the time to completely cure the composite part.

Instead, a simulation model of the infiltration/cure process would prove more beneficial and cost-effective. Through such a model, the effects of changes in fluid viscosity, preform permeability, and/or port location could be determined analytically as opposed to the more costly experimental techniques.

In order for analytical models to be accepted as valid replacements for experimental results, the accuracy of the model must be verified. This can be accomplished by comparing experimental flow fronts as a function of time to those predicted by the model during mold filling. The pressure distribution in the mold during infiltration provides another measure of verifying model accuracy. If the experimental and predicted pressures are in good agreement, then the actual and predicted velocity values are likewise in good agreement, provided accurate permeability measurements of the porous medium are made.

Due to the very nature of the pressure injection RTM process, an accurate measurement of the permeability is critical for success in modeling the infiltration process. The permeability of a porous media is the ease with which a fluid can flow through it. Small changes in permeability can result in very different infiltration behavior and times. Therefore, it is important to accurately measure the permeability of the fabric preforms used in the RTM process. In this work, two methods were used to measure the permeability of these preforms. The first, known as the steady state method, measures the permeability of a saturated preform. The second, denoted as the advancing front method, determines the permeability of a dry preform to an advancing fluid.

Therefore, it is the objective of this research to experimentally verify an analytical computer model for the pressure injection RTM process. This consists of the following steps:

1) Determine the porosity versus compaction pressure behavior for different fabric types
2) Determine the permeability versus porosity behavior for different fabrics with respect to different fluids
3) Determine the fluid/solid interaction between the resin and the preform
4) Perform flow visualization experiments to determine how the fluid actually infiltrates the fabric preform and compare these results to model predictions
5) Develop accurate models of the chemo-rheological behavior of the injected resin

Recent work performed by other researchers in the area of permeability and process modelling are presented in Chapter 2. The materials used in this study are discussed in Chapter 3. Experiments done to characterize the behavior of the fiber preforms used in this study are detailed in the following three chapters. The compaction characteristics of the preforms are presented in Chapter 4. The method used to determine the steady state permeability behavior and the results from these tests are discussed in Chapter 5. Likewise, the tests performed in order to determine the dry permeability of the fiberglass material are presented in Chapter 6. Tests done to evaluate the fiber/resin interaction through the measurement of surface tension and contact angle are the focus of Chapter 7.

The theory of the flow infiltration model and the set-up used for the flow visualization and mold filling experiments are explained in Chapter 8. Also,

experimental results of these tests are compared to model predicted flow patterns and infiltration times. The kinetics and rheological models for the epoxy resin used in actual panel production are presented in Chapter 9. Conclusions and summaries drawn from this work along with suggestions concerning possible work for the future are given in Chapter 10.

2.0 LITERATURE REVIEW

Over the past few years, much work has focused on the basic science of Resin Transfer Molding (RTM). The majority of the work has involved the effect of ply orientation/stacking sequence and resin flow direction on preform permeability. Some work has also been done in the area of fiber/resin interaction; e.g., surface tension, contact angle, and capillary pressure. Several researchers have also attempted to model the RTM process using various numerical and analytical techniques.

2.1 GOVERNING RELATIONSHIPS

The equation generally accepted as governing flow through a porous media was first proposed by Darcy [2]. By studying water flow through porous sand beds, he arrived at the following relationship

$$Q = \frac{S\,A}{\mu}\,\frac{\Delta\,P}{L} \qquad (2.1.1)$$

where

Q = volumetric flow rate

S = permeability of the porous medium

A = cross sectional flow area

μ = fluid viscosity

ΔP = applied pressure difference over length (L) of the porous medium.

The permeability of the fabric preform has generally been accepted as the most important parameter in RTM. E. Gali [3] has defined permeability as "that property

of a porous material which characterizes the ease with which a fluid may be made to flow through the material by an applied pressure gradient." Permeability is a tensor quantity which may vary by direction within a given medium.

Many models have been suggested to relate the permeability of the preform to its fiber volume fraction, v_f, and average fiber diameter, D_f. The most widely used are conduit flow models of which the one generally accepted is the Kozeny-Carman equation [4]

$$S = \frac{D_f^2}{16\ C} \frac{(1 - v_f)^3}{v_f^2} \qquad (2.1.2)$$

where C is the Kozeny constant which accounts for tortuosity and pore nonuniformity. However, the conduit models are limited because idealized structures are assumed and the models depend primarily on fiber volume fraction and fiber diameter.

In an attempt to overcome the shortcoming of the Kozeny-Carmen equation, Gutowski et al. [5] proposed modifying the equation for unidirectional reinforcements with different Kozeny constants in different directions. The Kozeny-Carman equation then has the form

$$S_{ii} = \frac{D_f^2}{\kappa_{ii}} \frac{(1 - v_f)^3}{v_f^2} \qquad (2.1.3)$$

where κ is the Kozeny constant and the subscript i refers to the x, y, or z direction.

Gutowski et al. [6] proposed the following heuristic model for the transverse permeability for a fiber bundle

$$S = \frac{R^2}{4\,k'} \frac{\left(\sqrt{\frac{v_a'}{v_f}} - 1\right)^3}{\left(\sqrt{\frac{v_a'}{v_f}} + 1\right)} \qquad (2.1.4)$$

where k' and v_a' are empirical parameters. The equation agrees well with the Kozeny-Carman equation when v_a' is equal to 1; but gives a much lower value for permeability when v_a' is less than 1.

Gebart [7] has presented models for through-the-thickness permeability which are dependent on the fiber packing in the preform. In the model, the flow resistance is assumed to be a result of the pressure drop across the gaps between individual fibers. For a preform composed of aligned quadrilaterally packed fibers, the equation is written as

$$S_z = \frac{16}{9\pi\sqrt{2}} \left(\sqrt{\frac{V_{f\,max}}{V_f}} - 1\right)^{5/2} R^2 \qquad (2.1.5)$$

where $V_{f\,max}$ is the maximum fiber volume fraction, $\pi/4$, and R is the fiber radius.

For hexagonal fiber bed packing, the relationship between fiber volume fraction and permeability may be written as

$$S_z = \frac{16}{9\pi\sqrt{6}} \left(\sqrt{\frac{V_{f\,max}}{V_f}} - 1 \right)^{5/2} R^2 \qquad (2.1.6)$$

where $V_{f\,max}$ in this case is $\pi/(2\sqrt{3})$.

Because most preforms are not made up of either quadrilateral or hexagonal fiber packing arrangement, but rather are random in nature, the following equation was suggested to relate through-the-thickness permeability and fiber volume fraction.

$$S_z = C \left(\sqrt{\frac{V_{f\,max}}{V_f}} - 1 \right)^{5/2} R^2 \qquad (2.1.7)$$

where the constant C depends on fiber arrangement and can be determined experimentally.

For flow parallel to the fibers, Gebart proposed the following equation

$$S = \frac{8R^2}{c} \frac{(1 - V_f)^3}{V_f^2} \qquad (2.1.8)$$

where c is a shape factor and is dependent on both fiber arrangement and fiber volume fraction.

Gebart also indicated that the Kozeny-Carman equation is strictly valid for flow parallel to the fiber direction in an unidirectional preform. He also stated that the

Kozeny constant should be considered a weak function of fiber volume fraction and, therefore, is not a constant.

Recently, Skartsis, Kardos, and Khomami [8] reviewed theoretical and experimental studies concerned with resin flow through porous media. They concluded that the Kozeny-Carman equation does not accurately describe the permeability behavior even though the flow might be Newtonian and at low Reynolds numbers. They also noted that the Kozeny constant differed dramatically from the theory and attributed this to a dependence on bed nonuniformities. They noted that the Kozeny constant is constant valued over narrow porosity ranges. However, for perfectly spaced and aligned cylinder arrays, the theoretical models satisfactorily described transverse permeability behavior but only for porosity values greater than 0.6. The predicted permeabilities for axial flow in aligned fiber beds and randomly arranged fibers was much lower than that actually observed during experiments.

2.2 IN-PLANE PERMEABILITY

The dependence of the above equations for permeability on the fiber radius is important because different preforms can have different permeabilities even though their fiber diameters and porosity values may be similar. Factors such as flow direction, weave type, and fluid/surface interactions can influence the permeability behavior of preforms. This section will discuss experimental work done to characterize in-plane permeability behavior for various fiber assemblies.

Work done by Adams, Miller, and Rebenfeld [9] measured parallel and transverse permeability values for three fabric types: (1) biaxially woven monofilament, (2) bi- and triaxially woven multifilament, and (3) several nonwoven fabrics. For the monofilament fabrics, the effect of mesh size and weave type, plain versus twill, on

permeability was studied. The permeability values were found to be larger for the larger mesh fabric and the fabric with the twill weave pattern due to the larger pore structures of these materials.

For the bi- and triaxially woven fabrics, permeability behavior was anisotropic when 2 plies were layered with the weave direction of each layer coincident. The permeability behavior became isotropic when the weave directions were laid perpendicular to one another. The authors noted that, in the case of nonwoven fabrics, isotropic flow patterns can be attributed to a completely random distribution of fiber orientations. If the fiber orientation is not random, the resulting flow will tend to be anisotropic in nature. They also saw a decrease in permeability values as the porosity decreased for the nonwoven fabrics.

Lam and Kardos [10] studied the effects of flow direction, fiber orientation, and bed thickness on the permeability behavior of graphite fiber preforms. For the case of flow perpendicular to the fibers in a unidirectional preform, the authors noted that the data fit well to the Kozeny-Carman equation for porosity values of 0.25 to 0.5. Flow parallel to the fibers in the unidirectional preform also followed the Kozeny-Carman equation. In both cases, bed thickness was shown to have no effect on the permeability behavior. Lam and Kardos also saw that the permeability decreased as more alternating plies were laid down at increasing angles. For the off-axis experiments, the plies of fibers were laid in a $[0°,\alpha]_n$ where α was 30°, 45°, and 90° and n was either 10 or 15. The 0°-90° layups had the lowest values of permeability. This resulted from the flow path becoming more tortuous and convoluted as the plies were rotated further off-axis.

Molnar, Trevino, and Lee [11] preformed experiments on flow direction permeabilities for random, unidirectional, and bidirectional fiber mats. They noted

that the permeability was higher for the bidirectional mats as opposed to the random mats for similar fiber volume fractions. If the porosity of the random mat was much higher than the bidirectional mat, then the permeability in the random mat was greater than the bidirectional mat. Likewise, the permeability of the unidirectional fiber mats for flow along the fibers was higher than that of the bidirectional mats.

Adams and Rebenfeld [12] reported on the effects of preform homogeneity on the in-plane permeability behavior. Homogeneous preforms were defined as assemblies with two or more layers of the same fabric orientated in the same in plane direction. Heterogeneous assemblies consisted of layers that have different directional permeabilities and degree of anisotropy.

For the homogeneous preforms, Adams and Rebenfeld noticed that the permeability of fabrics with minimal surface undulations showed no dependence on the presence of multiple layers. Usually these fabrics were nonwoven or unidirectional in nature. However, woven fabrics contained surface undulations caused by weaving and were not easily removed by compressive loads. In this case, as the number of layers present increased so did the permeability. This behavior was attributed to the large interlaminar pores created by the surface undulations present after the compressive load was applied.

In the heterogenous preforms, it was determined that in-plane permeability could be enhanced by replacing low permeability layers with higher permeability layers. The location of the high permeability layer helped to determine the amount of permeability increase. When the more permeable layers were placed at or near the centerline, the permeability increased more than when the more permeable layers were placed at the edge of the preform. The increase in permeability was attributed to transverse flow from the high to low permeability layers. This behavior was

thought to be the result of a pressure gradient generated as the fluid moved further ahead in the more permeable layer as opposed to the low permeability layer.

Kim et al. [4] studied in-plane permeability behavior for 0°-90° cloths and random mats. Their tests showed that the 0°-90° cloths had higher permeabilities than the random mats at the same fiber volume fractions. Their tests also showed that the permeability of the random mats increased slightly as the flow rate was increased. However, the 0°-90° cloth showed no change as the flow rate was increased. They attributed this behavior to the possibility of fiber movement in the random mat.

Like Adams and Rebenfeld [12], Kim et al. [4] also studied the effect of additional layers on permeability. Their research indicated that permeability increased in the 0°-90° cloth as layers were added. This was not the case for the random mat assembly. This behavior was attributed to an increase in the relative proportion of interlaminar pores at low fiber volume fraction as the number of layers was increased. This multilayer effect was reduced as the fiber volume fraction increased.

From their studies, Kim et al. [4] proposed that the permeability of a multilayer assembly could be calculated from the permeability of individual layers, as shown in the following equation

$$S_{avg} = \frac{\sum_{i=1}^{n} S_i A_i}{\sum_{i=1}^{n} A_i} \qquad (2.2.1)$$

where S_i is the permeability of each layer at the desired fiber volume fraction and A_i is the cross-sectional flow area for layer i. The predicted values were slightly

higher than the experimental values with the difference being attributed to a possible under estimation of the fiber volume fraction in each layer due to the absence of interfacial considerations.

Work done by Trevino, et al. [13] focused on measuring the permeability behavior of three types of glass fiber mats: (1) a continuous random mat, (2) a stitched bidirectional mat, and (3) a stitched unidirectional mat. For unidirectional mats, the x direction is along the fiber direction. For bidirectional mats, the x direction is perpendicular to the stitching and y is parallel to the stitching. In the case of the random mats, the x direction is the direction of flow while the y direction is perpendicular to flow. Their research showed that the x direction permeability was the same as the y direction for the random fiber mats. The x direction permeability for the random mat was similar to the bidirectional mat at low porosity and similar to unidirectional mat at high porosity values. The x direction permeability was found to be higher for the bidirectional fiber mats than for the unidirectional mats. It was found that the y direction permeability of the random mat was the highest, followed by the bidirectional and then the unidirectional mats. For all the fabrics, the permeability decreased as the porosity decreased.

2.3 THROUGH-THE-THICKNESS PERMEABILITY

During the RTM process, flow occurs through-the-thickness of the fabric as well as in the in-plane directions. Therefore, it is necessary to understand how stacking sequence and preform assembly can affect the through-the-thickness permeability behavior. This section will discuss work done in this area.

Molnar, Trevino, and Lee [11,14] looked at through-the-thickness permeability behavior for random and unidirectional mats. For a pure unidirectional mat, the

close packing of the individual layers was found to greatly reduce the permeability. However, by adding random mats with a higher through-the-thickness permeability to the unidirectional assembly, the fluid was able to quickly reach the unidirectional layers. Once the unidirectional layers were saturated, flow was able to penetrate through-the-thickness of the preform.

Trevino, et al. [13] also studied through-the-thickness permeability behavior for various fiber mats. It was determined that the through-the-thickness permeability, S_z, was independent of preform thickness for random fiber mats. They also found that S_z is smaller for unidirectional mats than in random and bidirectional mats at the same porosity values. In addition, z-direction permeability for the random mats was found to always be higher than that for bidirectional mats at identical porosity values.

Experiments also showed that through-the-thickness permeability was less than the x-direction permeability for all three glass fabrics. However, the difference between the two was larger for the bidirectional fiber mats than for the unidirectional and random mats.

Weideman [15] characterized the through-the-thickness permeability behavior for preforms composed of Hexcel Hi-Tech Multiaxial warp knit fabric and TTI IM7/8HS fabric. The Hexcel fabric was tested in an unstitched, a lightly stitched, and a knitted/stitched arrangement to determine the effects of stitching on the permeability. The TTI fabric was tested in preforms composed of 6, 8, 12, and 20 plies to determine the effect of preform thickness on permeability.

For the Hexcel material, it was found that knitted/stitched preforms had a significantly higher through-the-thickness permeability than the fully unstitched samples at similar porosities. This was attributed to the through-the-thickness

stitching providing a low flow resistance pathway for fluid movement in the knitted/stitched material. In the case of the TTI material, it was discovered that sample thickness had a negligible effect on the through-the-thickness permeability behavior.

The permeability behavior of the TTI fabric and the knitted Hexcel fabric was found to be very similar. This was due to both preforms being composed of fiber perpendicular to the flow direction with the rate of flow controlled by both the fiber bed packing arrangement and the gap distance between the individual fibers.

2.4 FACTORS WHICH INFLUENCE PERMEABILITY

As can be seen from the preceding two sections, it is apparent that permeability is highly dependent on flow direction and preform orientation. To predict the average permeability for the preform, knowledge of the in-plane and transverse permeability behavior is required. However, other factors can influence resin flow through the preform. These factors can be either physical or chemical in nature and include degree of preform saturation, capillary pressure, and wetting behavior.

Often in RTM, the preform is composed of individual plies stacked up in the desired orientation. By stacking the plies, interfaces are created which can severely influence the in-plane and through-the-thickness permeability behavior of the preform as a whole. Batch and Cumiskey [16] investigated this situation and presented three possible cases for the compression of a multi-ply preform. The cases were

(1) no interfacial effects

(2) interface has higher pore content than adjoining layers

(3) interface has lower pore content than adjoining layers.

Batch and Cumiskey [16] presented the following equation for the average fiber volume fraction, V_{avg}, to describe all three cases

$$V_{avg} = \left(\sum_{i=1}^{n} \frac{W_i}{V_{f,i}} + \sum_{j=1}^{n-1} \frac{W_{inter,\,j}}{V_{inter,\,j}} \right)^{-1} \qquad (2.4.1)$$

where W_i = weight fraction of layer i after removal of the portion contained in the interlayer

$W_{inter,j}$ = weight fraction of each interlayer j

$V_{f,i}$ = fiber volume fraction of layer i

$V_{inter,j}$ = fiber volume fraction of interlayer j.

Batch and Cumiskey also noted that the packing at the interface of different reinforcements can affect the fiber volume fraction distribution. The interlayer packing at the interface can influence the flow behavior in three ways:

(1) interlayer packing changes axial permeability due to high fiber volume fraction at the interface

(2) interlayer packing affects the fiber volume fractions and thicknesses of each layer in the cavity

(3) interlayer restricts transverse flow from layer to layer.

Another influence on the permeability behavior is the capillary pressure that can occur at the fluid/air interface. Several researchers [7,16,17,18] have integrated the one-dimensional form of Darcy's law and included the capillary pressure at the resin flow front. The integrated expression is useful for determining the permeability of a dry preform at a chosen porosity value and is known as the advancing front technique. However, Batch and Cumiskey [16], Williams et al. [17], and Foley and

Gutowski [18] do not include the porosity when calculating the advancing front permeability whereas Gebart [7] does. In both cases, the pressure term was written as

$$\Delta P + \frac{\sigma \cos \theta}{m} \qquad (2.4.2)$$

where the second term denotes the capillary pressure and is composed of the surface energy, σ, the wetting angle, Θ, and the mean hydraulic radius, m. The mean hydraulic radius is defined as the cross-sectional area normal to the flow divided by the perimeter presented to the fluid and can be determined from the expression [17]

$$m = \frac{d_f}{4}\left(\frac{1 - V_f}{V_f}\right) \qquad (2.4.3)$$

where V_f is the fiber volume fraction and d_f is the fiber diameter.

Ahn et al. [19] derived an equation for capillary pressure based on the porosity of the preform which is expressed as

$$P_c = \frac{F}{D_f}\frac{(1 - \phi)}{\phi}\sigma \cos \theta \qquad (2.4.4)$$

where D_f is the fiber diameter, ϕ is the porosity, σ is the surface energy, Θ is the contact angle, and F is called the form factor.

The form factor depends on fiber alignment and flow direction. For flow along the fiber direction in an unidirectional preform, the form factor is equal to 4. For flow perpendicular to the fibers, the form factor is equal to 2. Often the form factor must

be determined experimentally. In their work on resin flow through glass fiber preforms, Peterson and Robertson [20] calculated the form factor in equation (2.4.3) to be $16/\pi$. They noted that the capillary pressure increased with increasing fiber volume fraction and decreasing fiber diameter.

Skartsis, Khomami, and Kardos [21] have proposed a new analytical model for the effects of capillary pressure on the infiltration of a fiber preform by resin. The model incorporated the effect of pore structure of the preform and the effect of parallel-type nonuniformities (regions of varying permeability connected in parallel). Their analytical expression was dependent on the ratio of the Kozeny constant to the ideal Kozeny constant for the fiber bed. The ideal Kozeny constant is determined from steady-state flow through a bed with statistically uniform pore size distribution. Their experimental results matched well with theoretical values and showed that the contribution of the capillary forces to the infiltration process is significantly reduced when parallel type nonuniformities are present.

Recently, work has shown that preform saturation influences the permeability behavior of the preform. Dave and Houle [22] have suggested that, for flow through unsaturated porous media, the permeability is not constant but is defined as

$$S = S_e = S_i S_r \qquad (2.4.5)$$

where S_e is the effective permeability. The intrinsic permeability, S_i, depends on fabric geometry and was defined by the Kozeny-Carman equation. The relative permeability, S_r, varies from 0 to 1 depending on preform saturation.

Work done by Bear et al. [23] on a three dimensional orthogonal network of capillary tubes provided information concerning the behavior of both effective and

relative permeability. Their work indicated that the influence of saturation on effective permeability depends on the direction of flow. Also, their results showed that the components of relative permeability as commonly defined (ratio of effective to intrinsic permeability) do not constitute a second order tensor. They state that there is no advantage in extending the definition and concept of relative permeability to anisotropic media.

Odeh [24] discovered that the relative permeability of a core sample from a consolidated rock to the wetting phase was not affected by the viscosity ratio between the wetting (water) and non-wetting fluid (oil). The relative permeability for the non-wetting phase increased with an increase in the viscosity ratio. The non-wetting fluids were four different types of oil; naphtha oil, Socony Mobil oil, and two viscous mineral oils, with a viscosity ranging from 0.42 to 71.30 centipoise. The two wetting phases, water with different sodium chloride concentrations, had a viscosity range of 0.86 to 0.96 centipoise.

McCaffery and Bennion [25] performed relative permeability measurements on consolidated cores with 6 different fluids to determine the effect of wettability on values for relative permeability. Their work indicated that, for a given core saturation, the relative permeability in the core was higher for higher contact angles.

Dave and Houle [22] and Dave [26] stated that saturation in an initially dry preform depended on the capillary number, C_a, which was defined as

$$C_a = \frac{\mu V}{\gamma_{LV}} \qquad (2.4.6)$$

where μ is the resin viscosity, V is the velocity, and γ_{LV} is the surface tension of the

resin.

Experimental work by Williams et al. [17] and Martin and Son [27] support Dave's theory on effective permeability. Their experiments showed that permeability in an unsaturated preform was approximately 20% higher than in the saturated preform.

Work by Foley and Gutowski [18] on permeability measurements by the steady state and advancing front technique also show the same trend. They evaluated the permeability behavior of a plain and satin weave carbon fabric and Kevlar fabric when tested with water and oils. In virtually all of the tests, the permeability of the dry preform was found to be higher than that of the saturated preform. They proposed that channelling which occurs during mold filling as the fluid seeks preferential paths could be responsible for this behavior.

Experimental work by Pollard [28] indicated that the ratio of the permeability of a dry fiber mat to a wet fiber mat was greater than 1.0 for graphite mats. However, his work showed that this ratio was below 1.0 for most glass mats.

Surface tension can play an important role in composite processing because it determines the wettability of the reinforcing fibers by the resin [19]. A high surface tension increases the difficulty of removing voids during infiltration. Work done by Williams et al. [17] showed an increase in the apparent value of the Kozeny constant as the surface tension of the liquid increased.

Wettability has been defined as the ability of a liquid to spread itself over a surface [29]. Complete wetting is critical for the manufacture of quality composite parts. In addition, full wet out helps to improve the mechanical properties of the composite. The contact angle between the resin and the fiber is an indication of the wettability

of the liquid. The greater the contact angle, the lower the wettability of the liquid on the solid surface.

Experiments by Patel, Perry, and Lee [30] demonstrated the importance of wetting on tensile properties. Different injection pressures and mold temperatures were used to determine the effect of fiber-resin wetting. The higher tensile strengths were found to occur when the greatest degree of wetting occurred.

Recent work by Patel, Rohatgi, and Lee [31] showed that slower injection rates resulted in favored wetting behavior of individual fibers and that high molding temperatures resulted in better bonding and wetting. This improvement in wetting and bonding was directly correlated to improved tensile strength in the composite.

Patel, Rohatgi, and Lee also noticed that, for the same value of injection pressure, a higher fiber temperature resulted in higher tensile strength. Likewise, for the same value of fiber/mold temperature, a lower injection pressure resulted in better wetting.

Patel, Rohatgi, and Lee performed experiments on single filament composites that indicated that other conditions being identical, a resin with a larger gel time resulted in a stronger interface bonding. This behavior is attributed to the greater degree of diffusion of the resin molecules into the filament sizing that occurs with the longer gel times, as diffusion of the resin is much faster in the liquid state as compared to the solid state.

2.5 PERMEABILITY MODELS

Due to the complexity of fiber architecture and the lack of a standardized permeability test method, many researchers have attempted to determine analytical expressions for the permeability.

Gauvin and Chibani [32] presented theoretical expressions for permeability that included the effect of shear flow losses and the drag forces on the rovings. The expressions for the above mentioned losses were derived from the continuity and momentum equations using Lamb theory to estimate the drag coefficient. Good agreement was found between experiments and theoretical predictions.

Work by Greve and Soh [33] presented an analytical solution for the permeability behavior of anisotropic fiberglass preforms. Mold filling experiments were performed with a corn syrup/water mixture and fiberglass preforms to compare with the theoretical predictions. The experimental results correlated well with the analytical expressions. The authors also proposed a relationship between the Kozeny constant and the fiber arrangement.

Parnas and Phelan [34] and Phelan [35] have been successful in using the Brinkman equation to model the microscopic flow behavior in RTM. Parnas and Phelan used the Brinkman equation to model the effect of heterogeneities on the resin flow during the RTM process. The first heterogeneity, porous fiber bundles in the preform, was found to lead to void formation and higher effective permeabilities in unsaturated preforms. Channelling caused by boundary heterogeneities was found to result in the resin bypassing part of the preform during injection.

Phelan [35] also used the Brinkman equation to model axial and transverse flow

through square arrays of solid and porous cylinders. Calculations showed that the flow rate can be enhanced by the cylinder permeability. Preliminary experimental results also indicated that the permeability could affect the fluid mechanics of the flow around the fiber.

Sadiq, Parnas, and Advani [36] recently published experimental results of fluid flow in an ideal fiber bed consisting of cylindrical rods, either aluminum or nylon, in a square array which verified the air entrapment mechanism assumed in the model published by Parnas and Phelan [34]. Their experiments showed that voids formed when the fiber bundles were encompassed by the resin flow front and tended to remain stable afterwards. The fluid was injected into the mold transverse to the rods. Lower volume fractions inside the tows produced smaller voids. The experimental permeability of the fiber bundles was higher than that of solid rods with the same diameter.

The measured permeability values also showed excellent agreement with predicted values from the asymptotic model. This model is generated by using a lubrication solution for the lower porosity range. Over the higher porosity range, a cell model approach was used. By using transcendental functions for the intermediate porosity range, a hybrid model over the entire porosity range can be generated from the two separate models. Further details concerning this model can be found in reference [37]. The agreement existed for volume fractions ranging from 40% to 60%. The expression of S/r^2 was found to be constant for different fiber radii at the same volume fraction.

Gebart [7] presented equations for permeability in unidirectional preforms for flow parallel and perpendicular to the fibers. The equations were derived for an idealized unidirectional reinforcement with either a quadratic or hexagonal packing

arrangement. Numerical simulation for the case of flow perpendicular to the fibers was conducted using a finite difference based computer code. Excellent agreement was found between the numerical and approximate solutions at high fiber volume fractions. Agreement was also good at lower volume fractions.

Berdichevsky and Cai [38] used the self-consistent method and finite element simulation to estimate the permeability of an aligned fiber bundle. From the self-consistent method, equations were generated for both the longitudinal and transverse permeabilities as function of fiber volume fraction. In this method, the flow and energy balance of the insertion of a micro-level physical medium into a homogeneous medium was considered. The normalized longitudinal permeability is expressed as

$$S_x^* = \frac{1}{8V_f}\left[\ln\frac{1}{V_f^2} - (3 - V_f)(1 - V_f)\right] \qquad (2.5.1)$$

where V_f is the fiber volume fraction. Likewise, the expression for the normalized transverse permeability is given by

$$S_z^* = \frac{1}{8V_f}\left(\ln\frac{1}{V_f} - \frac{1 - V_f^2}{1 + V_f^2}\right) \qquad (2.5.2)$$

The finite element simulation considered the effect of four (4) idealized packing structures on the permeability. The packing structures considered were square, hexagonal, hollow square, and hollow hexagonal. The results of the simulation indicated that knowledge of fiber bundle characteristics other than the fiber volume fraction is required to accurately represent the permeability behavior for the fiber assembly.

A unified model, composed of both the self-consistent method and finite element simulation, was proposed which evaluates the permeability as a function of two variables, the ultimate fiber volume fraction and the actual fiber volume fraction. This model accurately portrays flow passing through obstacles, and therefore, different fiber packing arrangements can be considered.

Astrom, Pipes, and Advani [39] developed expressions for the flow rate - pressure drop relationship for the flow of Newtonian fluids through spherical and cylindrical beds. They also presented an equation for the flow rate of a power law fluid through a spherical bed and for the flow of a Carreau fluid through a cylindrical bed.

2.6 RTM PROCESS MODELING

Due to the complicated nature and the many processing variables of RTM, it would prove highly ineffective to determine optimum processing cycles through an iterative trial and error technique. A more effective method would be to analytically model the RTM process. This section will present relevant work in this important area.

Weideman [15] and Loos and Weideman [40] have developed a one-dimensional finite element model for the resin film infusion process. The model is divided into two submodels. One deals with heat transfer in the preform and the cure kinetics and viscosity behavior of the resin. The second submodel is concerned with the through the thickness infiltration of the resin into the porous preform. Numerical predictions of infiltration times and final fiber volume fractions compared well with experimental results.

Much work has also been done to model the mold filling aspect of RTM. Young et al. [41] presented numerical simulation results of flow front progression and pressure

traces during mold filling. Their model accurately predicted the flow front position and the filling pressure when random fiber mats with a high through the thickness permeability were used. When bidirectional mats were used, the model is accurate only when a hole was cut in the mat under the flow entrance. This difference was attributed to the reduced transverse permeability of the bidirectional mats which caused an increase in filling pressure and a decrease in fluid velocity not accounted for in the model.

Chan and Morgan [42] have modeled the infiltration of unidirectional preforms by resin flowing parallel to the fibers. The model considered both global flow, or flow parallel to the fiber axis along the large pore spaces formed among the fiber tows, and radial resin flow, or flow from large pore spaces into the smaller pore spaces formed among the individual filaments within the fiber tow. A difference in the void formation process was predicted for RTM when the resin flow was parallel to as opposed to across the fiber axis.

Cai [43] derived closed form solutions for wet length, mold filling time, and pressure distributions in simple mold shapes. One dimensional Darcy's law was used to model the resin flow in rectangular, trapezoidal, and circular molds. Results from the model indicated that the shorter flow path should be chosen whenever possible and that flow should occur from the large to the small side of the mold.

Several researchers have used the boundary fitted finite difference method for modeling the RTM process. Coulter and Guceri [44-46] and Li and Gauvin [47] have reported good agreement between numerical and experimental results for the resin flow in the preform.

Recently, however, Trochu and Gauvin [48] have pointed out possible shortcomings

for the boundary fitted finite difference method. They noted that for irregularly shaped molds, numerical instabilities might hinder convergence of the algorithm and for molds with interior obstacles or multiple ports the complexities of merging several resin front lines cannot be easily accomplished. They concluded that finite difference methods might provide a reliable first approximation for a simplified mold but that it may prove necessary to use finite elements for more complicated cases.

An alternative to the finite difference method is the use of finite element analysis in modeling the RTM process. Chan and Hwang [49] used finite elements to model resin flow for nonisothermal injection of a reactive polymer resin into a fibrous preform. Their model incorporated heat transfer, expressions for resin kinetics and viscosity, and various possibilities for resin/fiber types and mold layouts. A least squares finite element method was created for the solution of convection dominated mass balance and energy balance equations for the resin. Simulated flow patterns for the structural resin injection molding of polyurethane/glass fiber composites were presented to highlight the type of information provided by the model.

Another method used to model the flow behavior during RTM processing is the finite element/control volume technique. This approach uses the finite element method combined with nodal control volumes to solve the equations of motion and track the resin flow front as it moves through the mold. Early work by Fracchia, Castro, and Tucker [50] and Osswald and Tucker [51] showed good agreement between the analytical predictions and experimental results for both two dimensional thin molds and more complex shapes.

Bruschke and Advani [52,53] and Loos et al. [54] have published recent work in which they reported good agreement between experimental and theoretical results. Bruschke and Advani successfully modeled mold filling in anisotropic fiber mats with

both inserts and regions of varying permeability present in the mold. Loos et al. effectively simulated the flow behavior in a flat mold resulting from both a center port injection and dual side port injection. Model predictions compared favorably with actual flow patterns and fill time measured by dielectric sensors.

3.0 MATERIALS

This chapter will detail the materials used in this research. Two fabrics, style 162 E-glass and TTI IM7/8HS, were the materials of primary interest. The fiberglass was used in the flow visualization tests while the carbon fabric was used to make graphite/epoxy composite panels via the RTM process. Fiberite HMF 2474, a carbon fabric composed of high modulus fibers, was characterized to compare with the TTI fabric. Two stitched uniweave preforms, one manufactured for Douglas Aircraft Company and the other by Saerbeck, were also evaluated. A hat stiffened wing preform currently under evaluation by NASA Langley was also tested to determine its compaction and permeability behavior.

Fluids with different viscosities were used in the permeability testing to determine what effect, if any, the fluid viscosity and type would have on permeability behavior. The fluids used were tap water, Mazola corn oil, and Epon 815, a low viscosity epoxy resin.

3.1 FABRICS

Two types of fabric preforms were used extensively in this experimental investigation. The first, used primarily in the flow visualization tests, was a fiberglass fabric manufactured by Clark-Schwebel Fiberglass Corporation. The fabric was a plain weave known as Style 162 and consisted of tows woven in the warp and fill directions. There were 28 yarns in the warp direction and 16 yarns in the fill direction for a one inch square sample.

The second fabric was an eight (8) harness satin carbon fabric supplied by Textile Technologies Incorporated (TTI). The fabric, denoted TTI IM7/8HS, consisted of

6k tows of IM7 carbon fibers woven in a 0°/90° orientation. There were an equal number of tows in the warp (0°) and fill (90°) directions, with single Kevlar tows placed at 4 cm intervals to determine the orientation of individual plies.

A third fabric, Fiberite HMF 2474, was tested to determine the compaction and permeability behavior. Fiberite HMF 2474 is an eight (8) harness satin weave with glass stitches placed in the warp direction to aid in identification of fiber directions. It was desired to compare the differences between HMF 2474 and TTI IM7/8HS.

3.2 PREFORMS

Preforms tested included the Douglas uniweave preform, a preform manufactured by Saerbeck, and the NASA hat-stiffened preform. The NASA hat-stiffened preform is composed of four different fabrics laid up on a foam mandrel. All of these preforms are of interest for possible use in aerospace structures.

The Douglas uniweave preform is composed of (0°,+45°,90°,-45°) subgroups [55]. Six 9-ply subgroups are used to construct the preform. All the plies are composed of 3k tows with 44% of the fibers in the 0° direction, 44% in the ±45° direction, and 12% in the 90° direction. The preform is produced by lightly stitching 9 ply subgroups with a multineedle machine and subsequently stitching 6 of the 9 ply subgroups together with a heavy duty single needle. The Kevlar stitching is in the 0° direction, nominally 3/16" apart with approximately 8 stitches per inch.

The preform manufactured by Saerbeck is composed of six 4-ply subgroups [55]. The stacking sequence in each subgroup is (0°,+45°,90°,-45°). AS4 fibers are used in the preform and arranged such that 44% of the fibers are in the 0° direction, 44% in the ±45° direction, and 12% in the 90° direction. The 0° fibers are made of 12k

tows, those in the 90° direction are made of 3k tows, and those in the ±45° directions are made of 6k tows. The subgroups are stitched together with a polyester alternating tricot/chain knit. The tricot knit is normally used when 0° plies are on the preform surface. The damage tolerance of the preform has been improved by adding 1500 denier Kevlar through-the-thickness stitching. The Kevlar stitching is in the 0° direction, nominally 3/16" apart with approximately 8 stitches per inch. An unstitched Saerbeck preform was also tested to determine the effects of Kevlar stitching on the through-the-thickness permeability behavior of the preform.

The NASA hat-stiffened preform is a complex preform composed of different fabric types and orientations. The preform is constructed by inserting the Rohacell foam mandrel into a fabric "sleeve". The mandrel is 2.029 cm wide at the top and 7.35 cm wide at the base with a total height of 3.193 cm. The length of the mandrel is 109.22 cm. The interior angles at the base are 50.2°.

The stiffeners were constructed with a 5 harness satin (5HS) weave carbon fabric, a 3k unidirectional carbon fabric, and a 6k braided carbon preform. The skin of the preform is composed of [±45°/90°/±45°/0°]$_s$ layup. The 0° and 90° layers are made of the uniweave material while the ±45° layers are 5HS carbon.

The foam mandrel was first wrapped with the ±45° braided preform. The cap of the mandrel section was then partially completed by placing a 0° uniweave, a half ply of the 90° uniweave, and then another 0° uniweave ply. The wall of the mandrel was constructed by adding a half ply of the 90° uniweave. Then, the cap and wall were completed by adding ±45° layers of the 5HS carbon preform.

The preform below the mandrel, hereafter referred to as the core preform, was comprised of the following layers. First, starting at the ±45° braid surrounding the

mandrel, a half ply of the 90° uniweave was added. Then, ±45° layers of the 5HS carbon were added followed by two 0° uniweave layers. This was followed by ±45° layers of the 5HS carbon, a 90° uniweave layer, and then another ±45° layer. Kevlar stitching was used to hold the base preforms together. Tackifier was used to hold the 0° and 90° layers on top of the mandrel. A schematic diagram of the NASA hat-stiffened preform is given in Figure 3.1.

3.3 FLUIDS

Three fluids with different viscosity values were used to determine the influence of viscosity on permeability behavior of the Style 162 E-glass and the TTI IM7/8HS carbon preforms. The first was tap water obtained from a wall source at room temperature. The second was a corn oil manufactured by Mazola to which small amounts of Oil Red O dye (purchased from Sigma Chemical Company) were added to assist in observing the flow behavior of the fluid in the different preforms. In-plane permeability tests were also conducted on the 162 E-glass and the TTI IM7/8HS preforms with Epon 815.

Single fiber pull-out tests were conducted to measure the interaction between the fiber and infiltrating fluid. For these tests, both the corn oil and the Epon 815 were used. The epoxy was also used to perform some dry permeability tests on the glass fabric. In this case, some Oil Red O dye was added to increase the contrast between the fluid and the fabric.

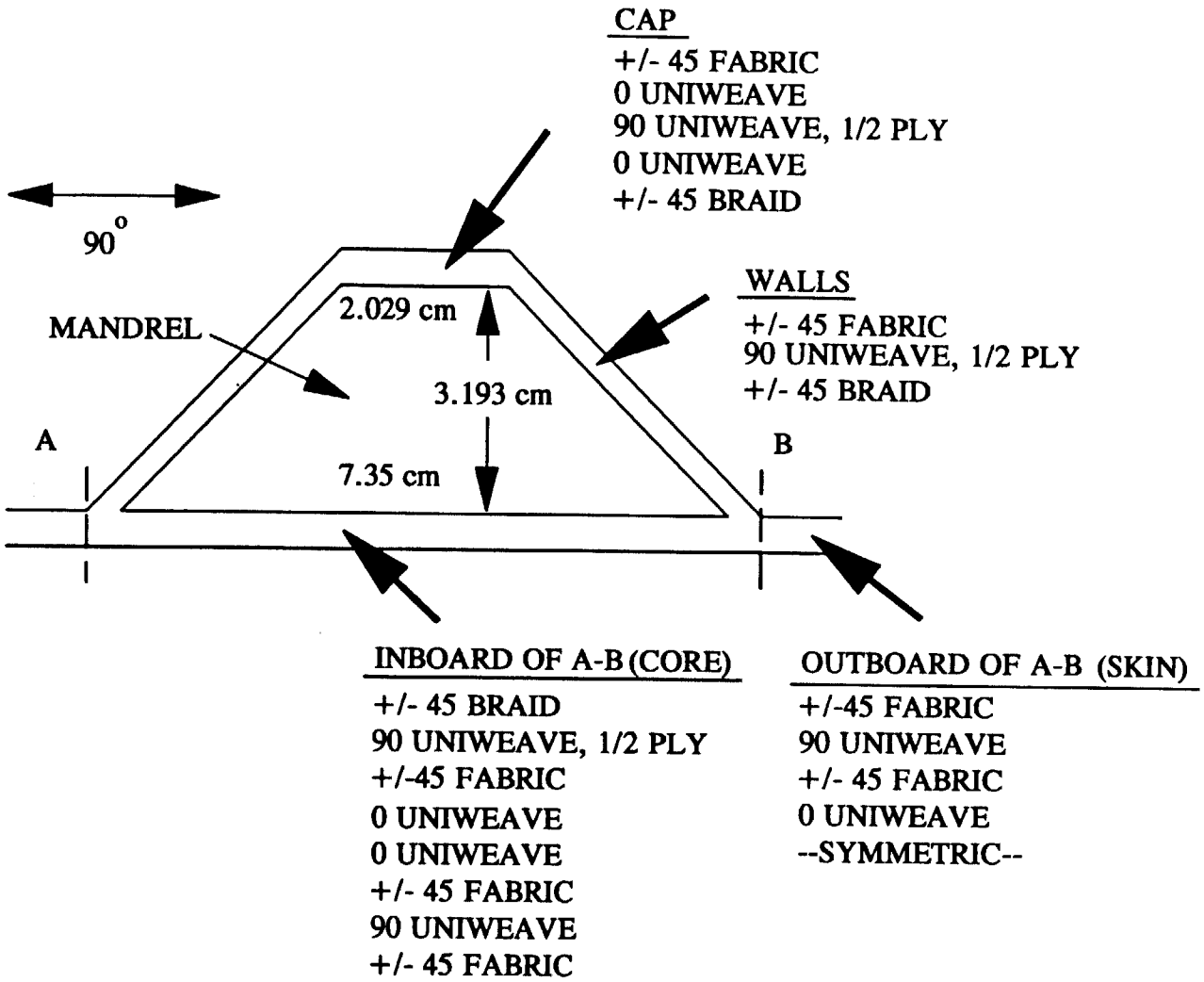

Figure 3.1: Schematic Diagram of NASA hat-stiffened preform.

4.0 COMPACTION BEHAVIOR

In this chapter, an explanation of the technique used to determine the relationship between fiber volume fraction and compaction pressure will be presented. Also, results from these tests will be given for the different types of fabrics investigated during this study.

4.1 AREAL WEIGHT DETERMINATION

As mentioned earlier, several fabric preforms were tested to determine their behavior under an applied compaction load. They were TTI IM7/8HS, Style 162 E-glass, Fiberite HMF 2474, the Saerbeck preform, the Douglas uniweave preform, and the NASA hat-stiffened preform. For the first three, the desired number of plies were cut and stacked with the desired orientation to form the preform. This was 10 plies for the 162 E-glass and Fiberite HMF 2474 and 12 plies for the TTI IM7/8HS. For the two preforms, only a single piece was cut from the pre-assembled preform. In the case of the NASA hat-stiffened preform, a different approach was taken. Samples taken from the skin and core preforms were tested individually. For the individual fabric types in the stiffener, a 4 ply preform of each material was tested.

In all cases, the samples were cut to size using a razor blade and a 5.08 cm x 5.08 cm template. Each piece was carefully cut in order to minimize damage to the sample. The weight of the assembled preform was determined and the initial uncompacted thickness measured. The areal weight was then found by simply dividing this weight by the total area of the sample. An average areal weight and initial thickness for each complete preform assembly is presented in Table 4.1. Due to the complex layup of the NASA hat-stiffened preform, the areal weights and initial thicknesses for the different fabrics used in the panel are given in Table 4.2.

Table 4.1: Areal weights and initial thicknesses of fabric preforms.

Fabric Type	Areal Weight (g/m^2)	Initial Thickness (mm)
162 E-glass	3861.0	3.81
TTI IM7/8HS	5028.0	9.00
Fiberite HMF 2474	3680.0	4.32
Saerbeck	7619.6	8.00
Douglas	7986.3	10.80

Table 4.2: Areal weights and initial thicknesses for the different components of the NASA hat-stiffened preform.

Preform	Areal Weight (g/m^2)	Initial Thickness (mm)
Skin	2286.3	3.30
Braided	1918.1	2.67
$\pm 45°$ 5HS	1763.1	2.45
Core	1821.2	2.39

With the increasing use of through-the-thickness stitching to improve damage tolerance in these preforms, it could prove necessary to consider the effect of this stitching on the areal weight of the preform. For the individual fabrics tested in this study, there was a minimal amount of stitching present in the assembled preform. Therefore, the effects of stitching was considered to be negligible.

4.2 COMPACTION TESTS

4.2.1 Experimental Set-up

The porosity/compaction pressure behavior of various preforms was determined by measuring the load required to reach a desired fiber volume fraction. The sample preforms consisted of the desired number of plies placed in a matched metal mold with a 5.08 cm x 5.08 cm test section. The thickness of the preform at each applied load was related to the fiber volume fraction through the areal weight equation expressed below

$$v_f = \frac{\xi}{\rho_f t_p} \qquad (4.2.1)$$

where v_f is the fiber volume fraction, ξ is the areal weight of the sample, ρ_f is the density of the fiber, and t_p is the thickness of the preform. As mentioned in the previous section, the areal weight is the weight of the sample divided by its area. For heavily stitched preforms, a total density should be used based on the density of the fibers and stitching material and the percentage of each within the total preform.

Compaction pressure was slowly applied until the first desired fiber volume fraction was reached at which point loading was stopped and the load level allowed to achieve equilibrium. The equilibrium load was recorded and the load was reapplied

until the next fiber volume fraction was reached. This procedure was repeated until the entire test had been completed. For each fabric preform tested, a minimum of two (2) tests was conducted to ensure repeatability.

The fiber volume fraction, v_f, can be related to the porosity, ϕ, by the following equation

$$v_f = 1 - \phi \tag{4.2.2}$$

The loads required to reach fiber volume fractions ranging from approximately 40 to 60% were recorded.

4.2.2 Results

After all tests had been completed, the applied compaction pressure was calculated by dividing the load at each fiber volume fraction by the area of the sample (25.81 cm^2). A graph was then made of fiber volume fraction as a function of applied compaction pressure.

For each case, a power law regression model was used to establish a relationship between the fiber volume fraction and applied pressure. The equation had the form

$$v_f = a\ (\textit{Compaction Pressure})^b \tag{4.2.3}$$

where a and b are constants that are determined by regression analysis. Table 4.3 lists these constants for each of the five fabric preforms previously mentioned. The experimental constants for the NASA hat-stiffened preform are given in Table 4.4.

The resulting curve for the 162 E-glass preform is shown in Figure 4.1. The curves

Table 4.3: Experimental constants for fiber volume fraction as a function of applied compaction pressure.

Fabric Type	a	b
162 E-glass	0.2745	0.1052
TTI IM7/8HS	0.3671	0.1056
Fiberite HMF 2474	0.4275	0.1138
Saerbeck	0.4523	0.0546
Douglas	0.2604	0.1241

Table 4.4: Experimental constants for fiber volume fraction as a function of applied compaction pressure for the NASA hat-stiffened preform.

Fabric Type	a	b
Skin	.3938	.1013
Braided	.223	.1956
±45°	.1619	.2615
Core	.2202	.2132

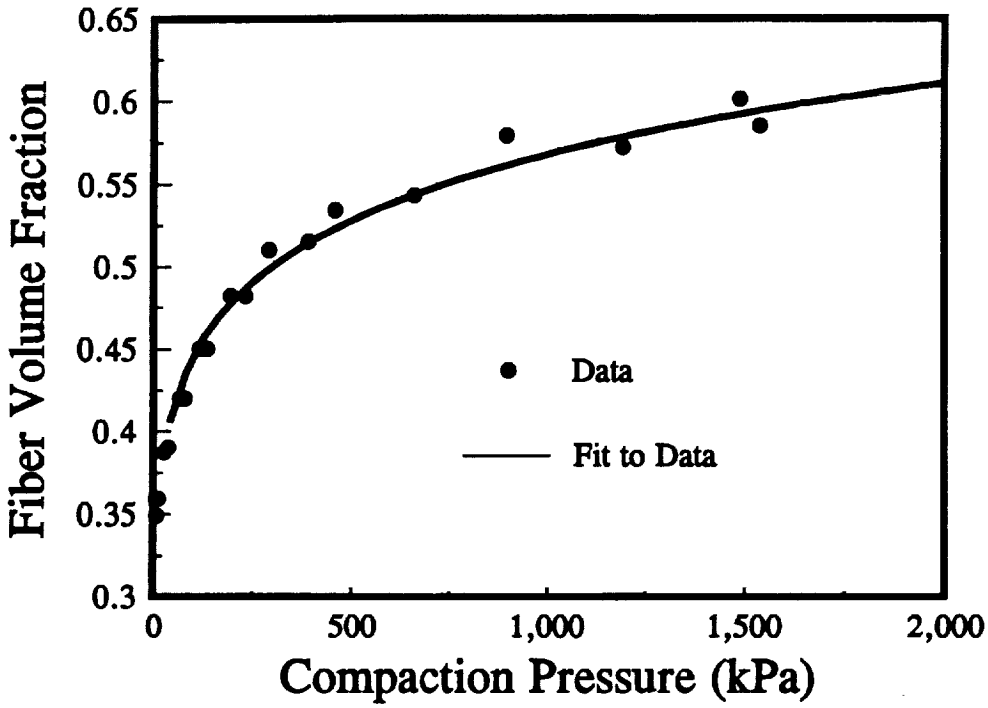

Figure 4.1: Fiber volume fraction as a function of applied compaction pressure for 162 E-glass preform.

for the TTI IM7/8HS preform, the Fiberite HMF 2474 preform, the Saerbeck preform, and the Douglas preform are shown in Figures 4.2, 4.3, 4.4, and 4.5, respectively.

Each preform shows an initially non-linear increase in fiber volume fraction as the load is applied. As the maximum preform deflection is reached, a significantly greater load is required to increase the fiber volume fraction. This is reflected in each curve by the linear relationship at higher loads.

The compaction pressure necessary to reach a desired fiber volume is lower for both the Fiberite and TTI IM7/8HS assemblies than that of the 162 E-glass. This is the result of the complex weave pattern found in the two carbon preforms. The waviness of the eight harness satin weave results in gaps between adjacent layers. As the compaction load is applied, these gaps are eliminated and the fiber are able to move and achieve an optimal state of compaction. Therefore, the compaction loads remain low.

Due to the simple biaxial weave used in the 162 E-glass fabric, there is very little fiber waviness in each layer. Therefore, the layers start out with a larger degree of contact than the TTI IM7/8HS preform. As the load is applied, less fiber movement occurs and the load increases more rapidly.

Other factors that may explain the difference in compaction behavior between the TTI and the 162 E-glass is the stiffness of the individual fibers. Also, there may be a rate dependence involved as the plies may relax at different rates.

The tightly stitched structure of both the Saerbeck and Douglas preforms account for

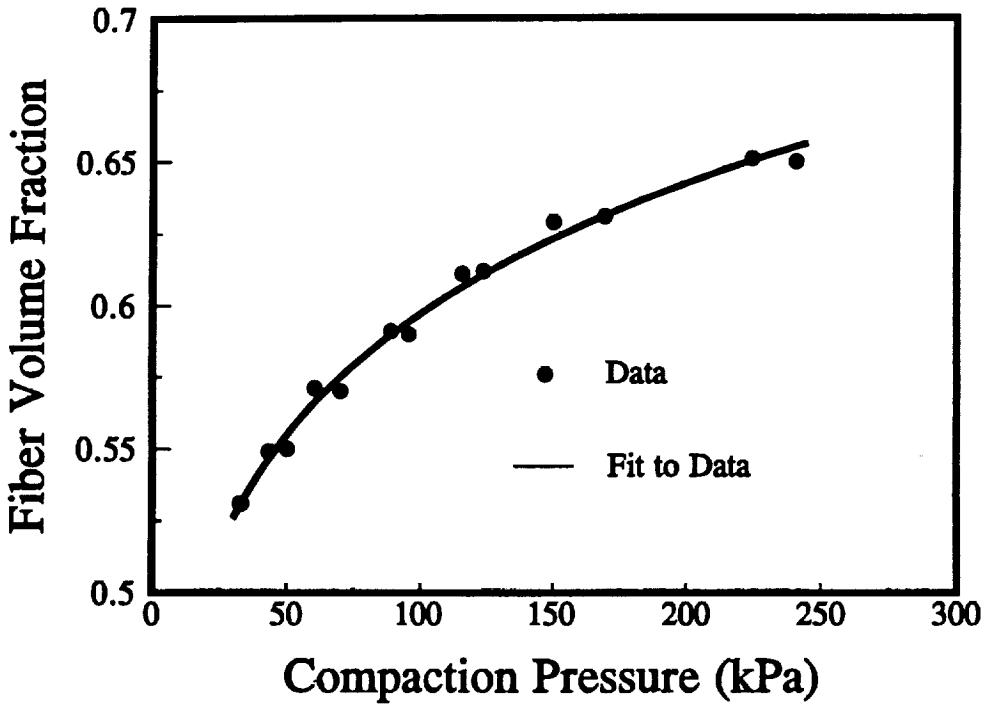

Figure 4.2: Fiber volume fraction as a function of applied compaction pressure for TTI IM7/8HS preform.

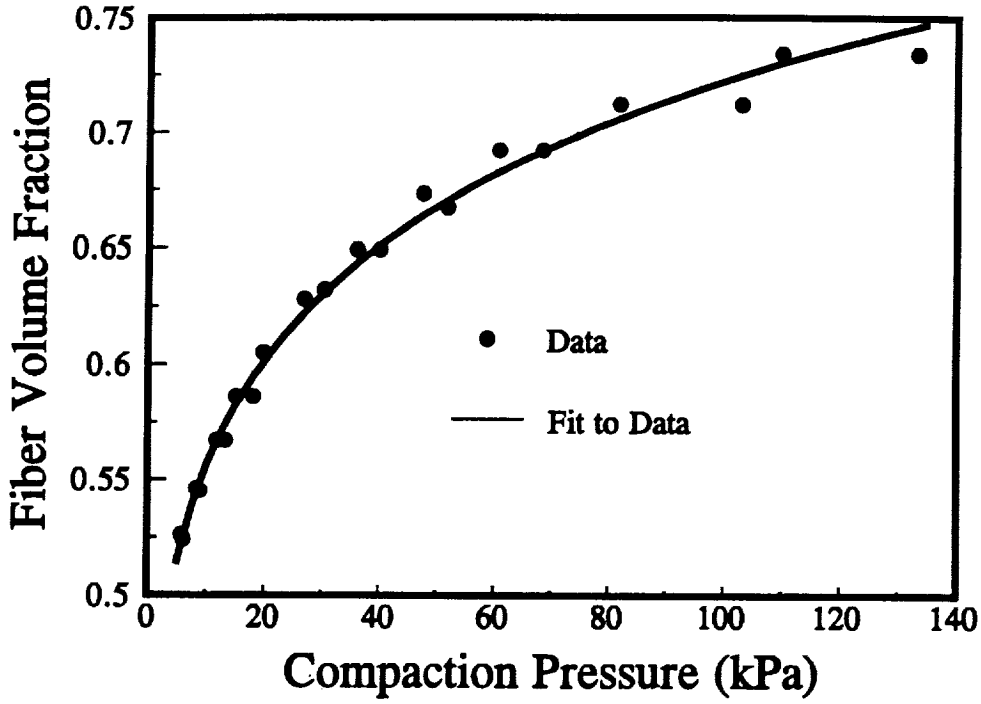

Figure 4.3: Fiber volume fraction as a function of applied compaction pressure for Fiberite HMF 2474 preform.

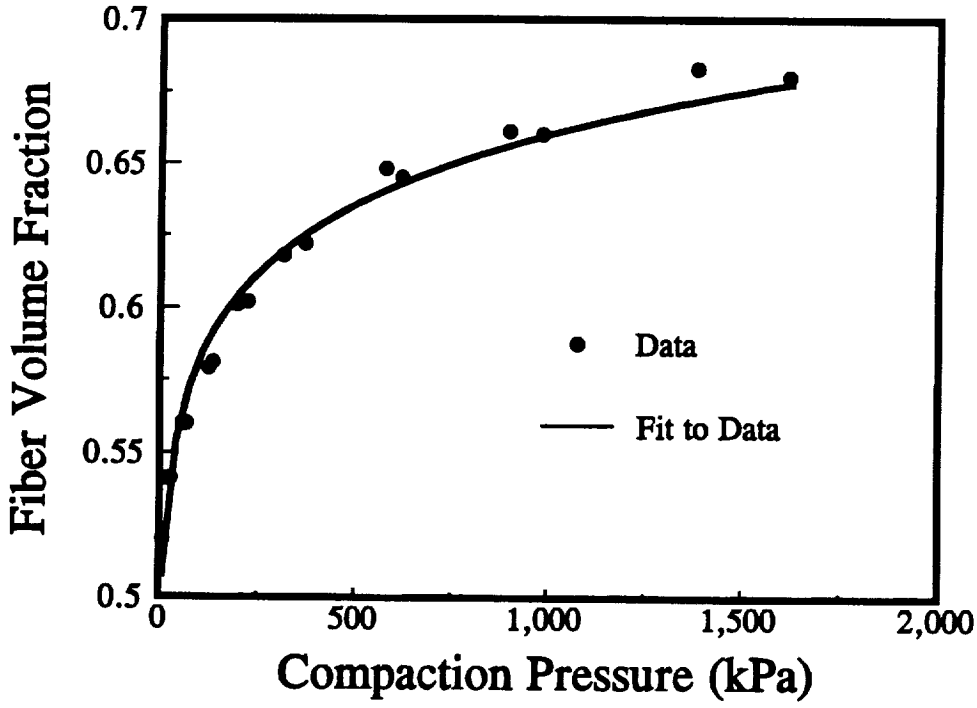

Figure 4.4: Fiber volume fraction as a function of applied compaction pressure for Saerbeck preform.

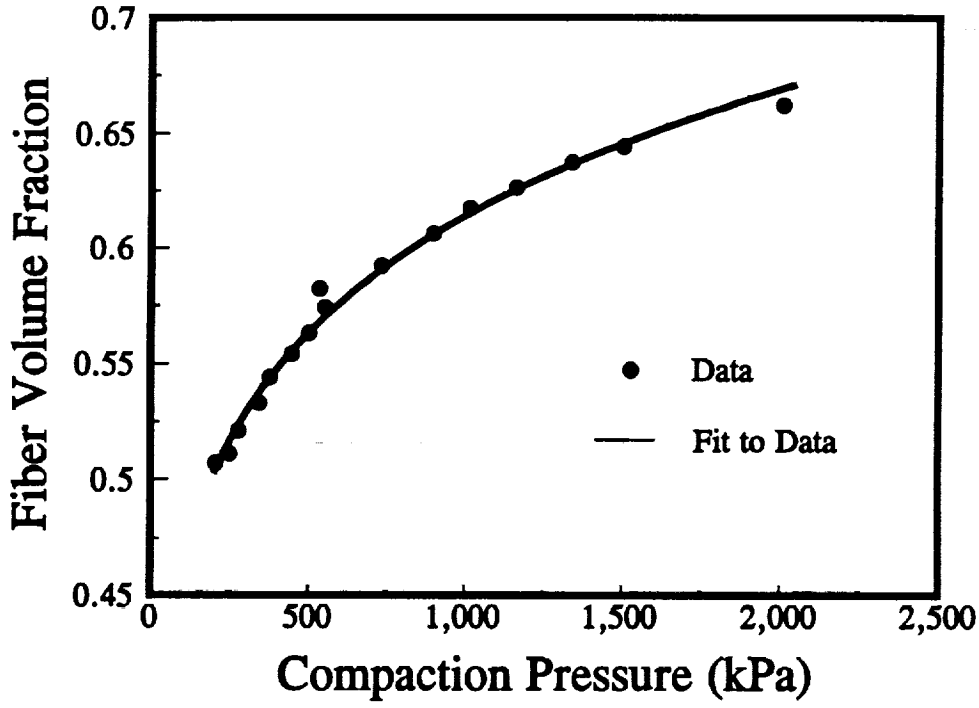

Figure 4.5: Fiber volume fraction as a function of applied compaction pressure for Douglas Uniweave preform.

the high compressive load required to reach higher fiber volumes. The tight stitching allows for no gaps to exist between plies and little relaxation during the compaction process. Therefore, high loads are required to reach the higher fiber volume fractions.

The compaction curves for the different components of the NASA hat-stiffened preform are shown in Figures 4.6-4.9. All of the fabrics used in the preform have very little through-the-thickness stitching. Therefore, the fibers are able to move during compaction to achieve the preferred orientation. Hence, the pressure needed to achieve a fiber volume fraction of 60% remains fairly low.

The relationship between compaction pressure and fiber volume fraction is very important in the RTM process. By knowing this relationship, the preform can be compacted to the desired fiber volume fraction prior to resin injection. Also, the power law relationship between the compaction pressure and the fiber volume fraction was used in the model to determine the approximate fiber volume fraction that would result from applied loads.

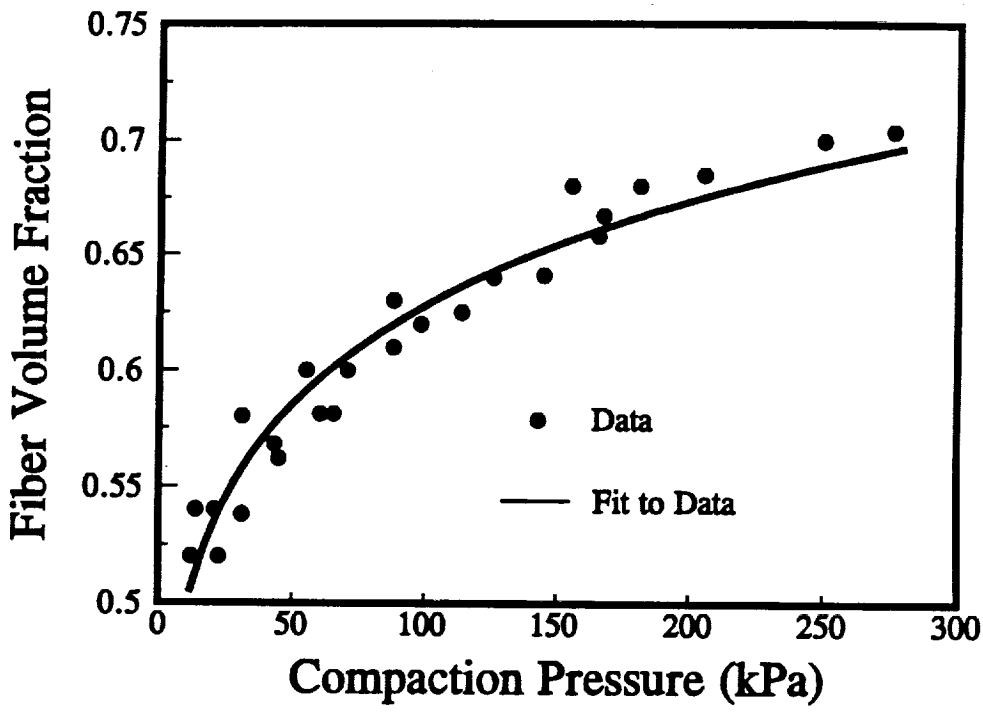

Figure 4.6: Fiber volume fraction as a function of applied compaction pressure for the skin of the NASA hat-stiffened preform.

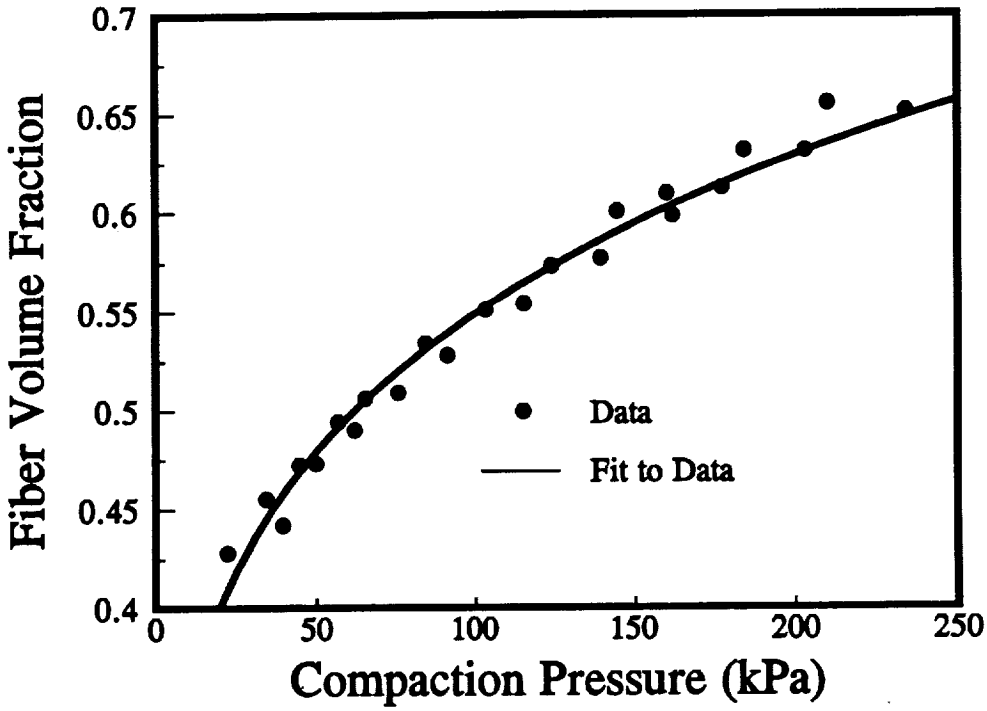

Figure 4.7: Fiber volume fraction as a function of applied compaction pressure for the braided preform of the NASA hat-stiffened preform.

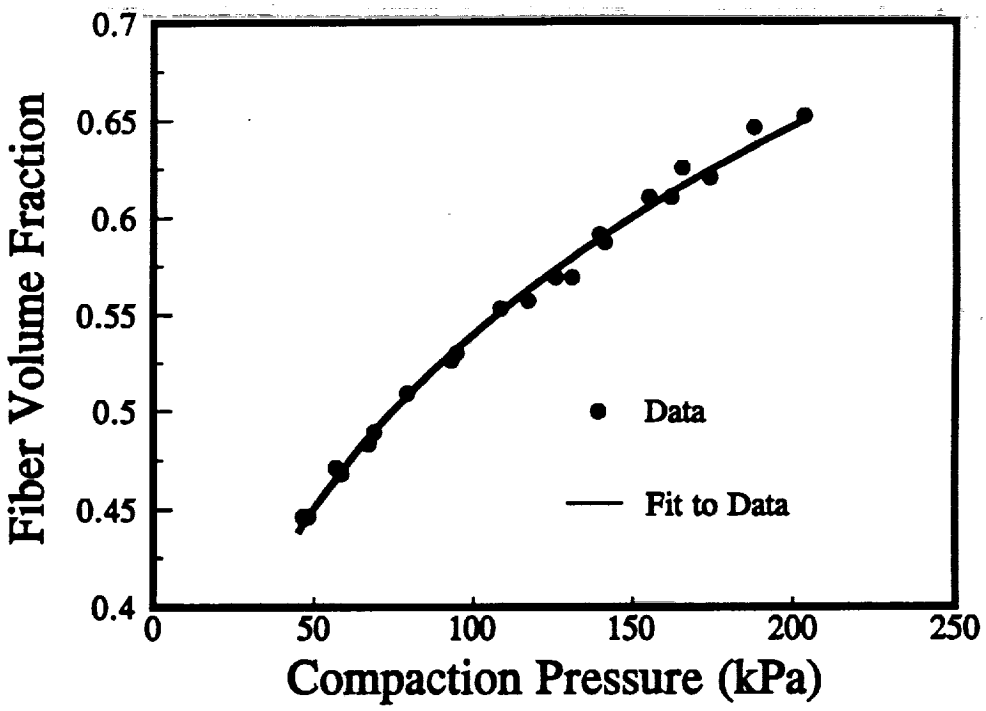

Figure 4.8: Fiber volume fraction as a function of applied compaction pressure for the ±45° preform of the NASA hat-stiffened preform.

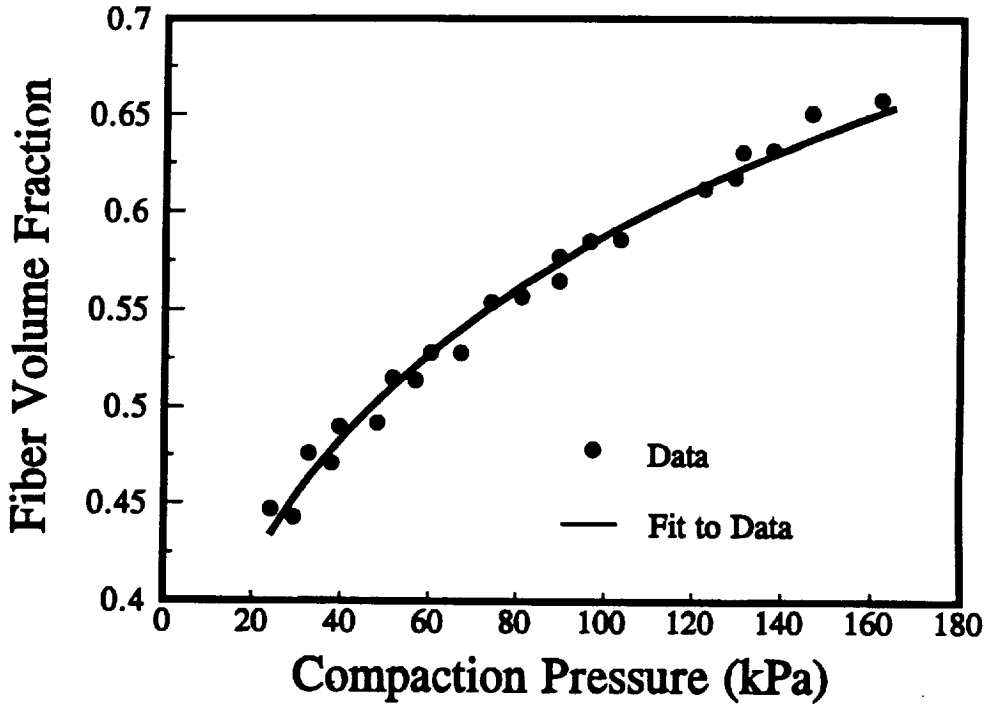

Figure 4.9: Fiber volume fraction as a function of applied compaction pressure for the core preform of the NASA hat-stiffened preform.

5.0 STEADY STATE PERMEABILITY BEHAVIOR

As explained earlier, permeability is the ease with which a fluid moves through a porous medium. The permeability of the medium is directly related to the amount of porosity present in the medium. Therefore, it is important to understand the relationship between the applied compaction pressure and the porosity behavior of the fiber preforms as presented in the previous chapter. Also, to ensure complete infiltration prior to cure, knowledge of the preform's permeability behavior is essential.

This chapter will discuss results generated from tests performed to characterize the steady state permeability behavior of the various preforms. Steady state permeability is the permeability of a saturated preform to an infiltrating fluid. The preforms were tested in both the through-the-thickness and in-plane directions. One-dimensional Darcy's Law was used as the governing relationship to determine the permeability behavior of the respective preforms. The resulting data were fit using a power law regression model.

5.1 EXPERIMENTAL

For the steady state permeability tests, an equilibrium fluid flow rate is established through a fiber preform compacted to the desired fiber volume fraction. Both the upstream and downstream pressures are recorded through the use of dial pressure gauges. The flow rate was determined by measuring the time necessary for a specified volume of fluid to accumulate in a graduated cylinder.

Both in-plane and through-the-thickness permeabilities of various preforms were determined. The through-the-thickness measurements were made in a test fixture

with a 5.08 cm x 5.08 cm test section. The in-plane measurements were conducted in either a fixture with a 15.24 cm x 15.24 cm test section or one with a 5.08 cm x 5.08 cm test section. For all tests, the preform was compacted to the minimum fiber volume fraction of interest and then saturated by allowing the fluid to slowly infiltrate and wet out the sample. The volume fraction was related to the sample thickness through the areal weight equation given in Chapter 4 (Eq. 4.2.1).

At each volume fraction of interest, several flow rates were used and the resulting pressure differentials associated with each flow rate were measured. Through the use of Darcy's Law (Eq. 2.1.1),the flow rate was related to the pressure drop measured at each fiber volume fraction. By plotting flow rate versus pressure drop and determining the slope of a linear least squares fit to the data, the permeability for each volume fraction could be determined by

$$S = \frac{slope\ \mu}{A} \qquad (5.1.1)$$

where μ is the viscosity of the fluid and A is the flow area. An example of this procedure can be found in reference 15.

The tests were conducted over several fiber volume fractions and the resulting graphs of permeability versus fiber volume fraction were fit with a power law regression model similar to that used for the porosity/compaction pressure data.

5.2 THROUGH-THE-THICKNESS TESTS

For through-the-thickness tests, a fabric preform with dimensions of 5.08 cm by 5.08 cm was placed into the test fixture. After compacting the preform to the desired fiber

volume fraction, four (4) different flow rates were passed through the preform. The equilibrium pressure difference was recorded along with the height of the preform. These two values were used to determine the pressure gradient that existed over the thickness of the preform. A schematic diagram of the experimental setup for the through-the-thickness tests is given in Figure 5.1.

All six fabric types were tested in the through-the-thickness direction. The fluids used were either tap water or corn oil. The viscosity of the water was 0.001 Pa·s while that of the corn oil was approximately 0.060 Pa·s. The Fiberite preform was tested with water while the other fabrics were tested with the corn oil.

After all tests were completed, permeability values were plotted as a function of fiber volume fraction. A power law regression model was then used to fit a smooth curve through the data. The power law had the form

$$\textit{Permeability} = a\ (\textit{Fiber Volume Fraction})^b \qquad (5.2.1)$$

where a and b were determined by the curve fitting program. Those constants, along with the fluid used to test each preform are presented in Table 5.1. Again, the results for the NASA hat-stiffened preform are presented separately due to the complexity of the preform. The constants for the NASA preform are presented in Table 5.2.

Figures detailing the relationship between the through-the-thickness permeability and fiber volume fraction are presented next. The permeability measurements for 162 E-glass tested with corn oil are given in Figure 5.2 while that of the TTI preform tested with corn oil are given in Figure 5.3.

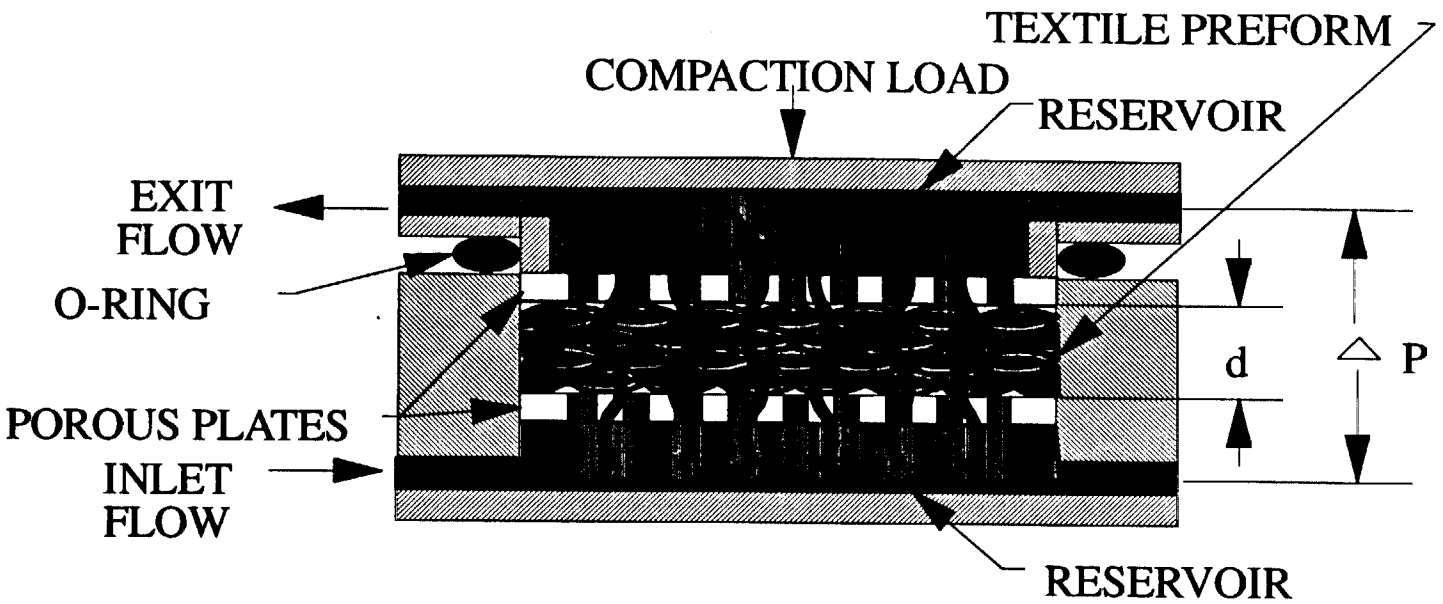

D'ARCY'S LAW:

$$Q = A \frac{S \Delta P}{\mu d}$$

WHERE:

Q = VOLUMETRIC FLOW RATE
S = PERMEABILITY CONSTANT
μ = VISCOSITY OF FLUID
$\Delta P/d$ = PRESSURE GRADIENT
A = AREA NORMAL TO FLOW

Figure 5.1: Schematic of through-the-thickness permeability experimental setup.

Table 5.1: Experimental constants for through-the-thickness permeability as a function of fiber volume fraction.

Fabric	a	b	Fluid Used
162 E-glass	4.7E-13	-5.103	Corn oil
TTI IM7/8HS	4.4E-15	-9.065	Corn oil
Fiberite HMF 2474	7.9E-15	-8.063	Water
Saerbeck	6.6E-15	-10.454	Corn oil
Douglas	4.1E-15	-10.162	Corn oil

Table 5.2: Experimental constants for through-the-thickness permeability as a function of fiber volume fraction for the NASA hat-stiffened preform.

Preform	a	b	Fluid
Skin	1.2E-13	-3.4807	Corn oil
Braided	2.1E-13	-4.5466	Corn oil
±45° 5HS	5.8E-13	-3.7970	Corn oil
Core	1.7E-13	-4.1114	Corn oil

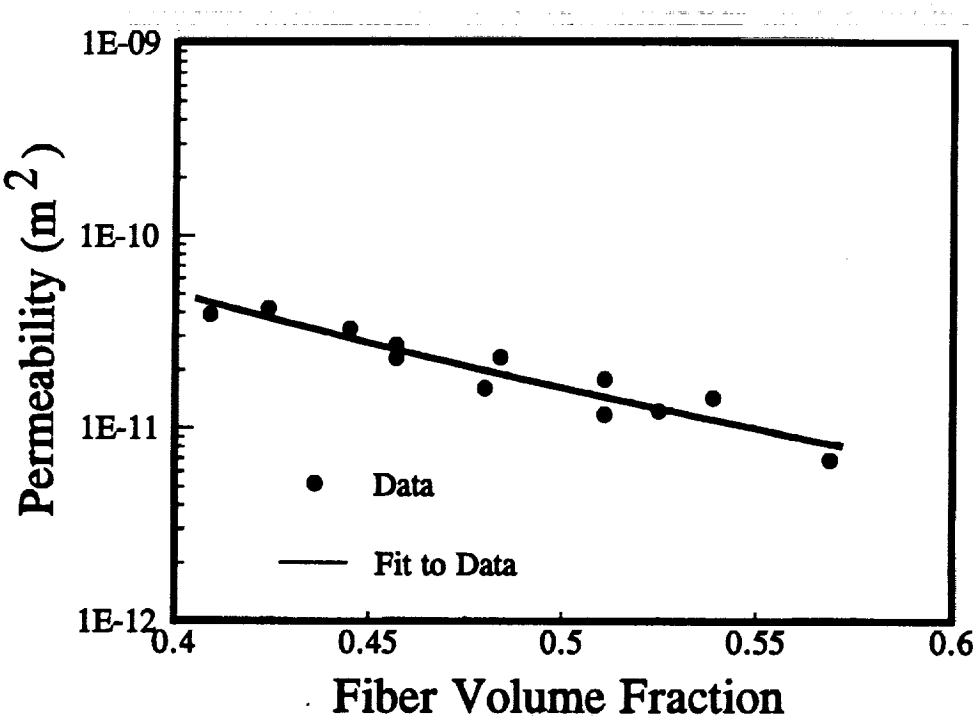

Figure 5.2: Permeability behavior for the 162 E-glass preform tested in the through-the-thickness direction with corn oil.

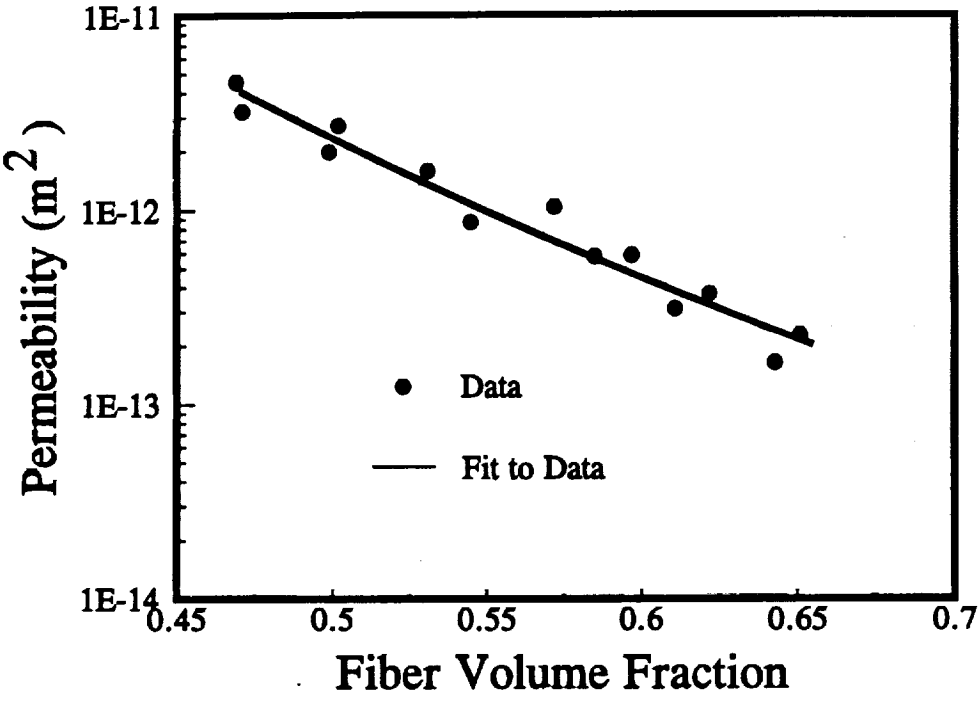

Figure 5.3: Permeability behavior for the TTI IM7/8HS preform tested in the through-the-thickness direction with corn oil.

It is interesting to note that for a given fiber volume fraction, the permeability of the 162 E-glass is approximately an order of magnitude higher than that of the TTI IM7/8HS preform. The reduction in permeability as fiber volume fraction is increased is also more pronounced in the TTI material. This may be attributed to the more complicated eight (8) harness satin weave of the TTI preform. Due to the complex weave pattern, the flow paths in the TTI preform are more convoluted and the fluid has a harder time passing through the preform. Therefore, the TTI preform has a lower permeability than that of the 162 E-glass preform. Also, as the more complex weave of the TTI preform is compressed, the flow paths close off at a faster rate than those of the 162 E-glass preform, resulting in a faster decrease in permeability for the TTI preform than the 162 E-glass preform.

The permeability behavior of the Fiberite material is shown in Figure 5.4. The through-the-thickness permeability behavior for the Fiberite fabric is similar to that of the TTI IM7/8HS preform. This is expected because both preforms utilize the same eight (8) harness satin weave. However, the large degree of similarity is surprising because the TTI preform was tested with corn oil while the Fiberite preform was tested with water. This suggests that the fluid used during testing is not critical provided accurate viscosity measurements are taken to determine the viscosity of the test fluid.

In Figure 5.5, the permeability behavior for the Saerbeck preform, both stitched and unstitched, is shown as a function of fiber volume fraction. The effects of the Kevlar stitching on the permeability behavior of the Saerbeck preform (Figure 5.5) is clearly seen. The preform with the Kevlar stitching has a much greater permeability over the entire range of fiber volume fractions tested than does the preform without the stitching. Obviously, the Kevlar stitching provides through-the-thickness flow paths that significantly increase the permeability.

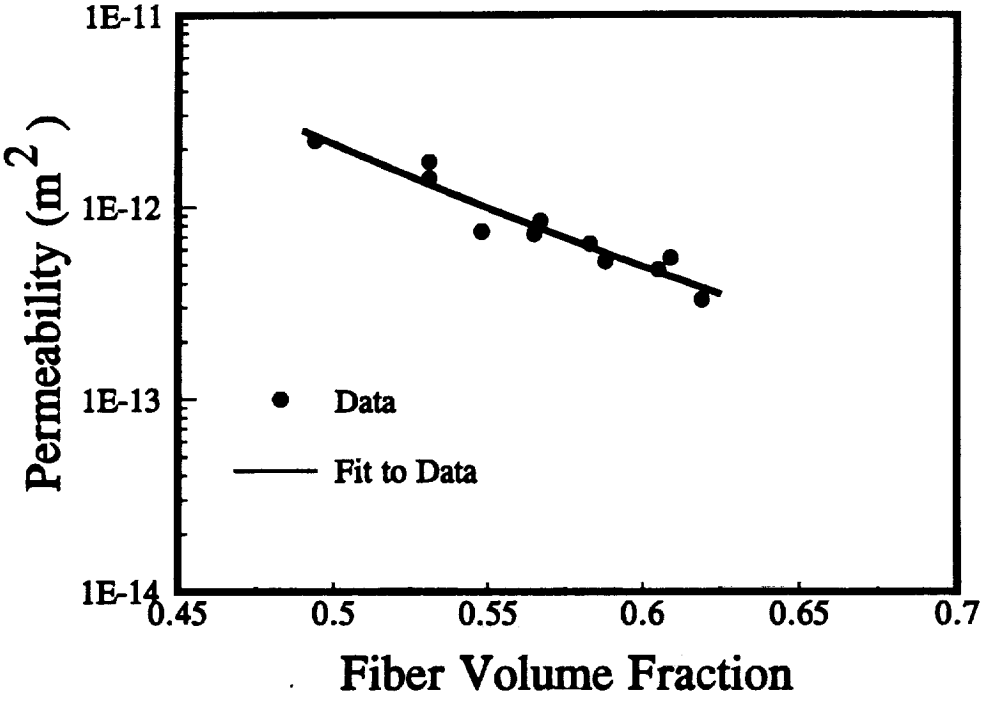

Figure 5.4: Permeability behavior for the Fiberite HMF 2474 preform tested in the through-the-thickness direction with water.

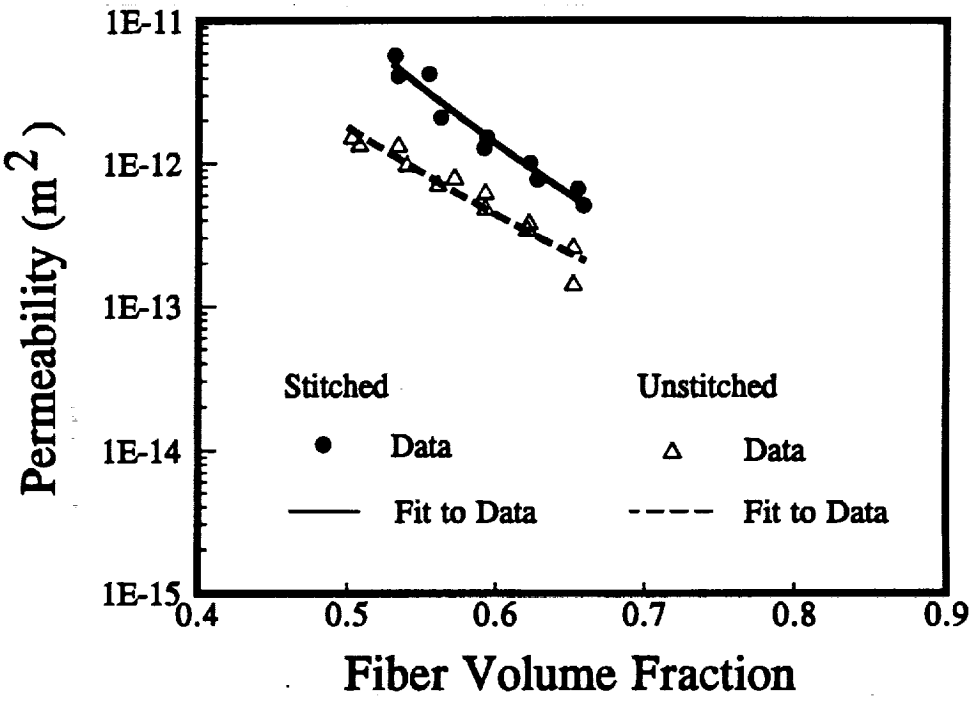

Figure 5.5: Permeability behavior for the Saerbeck preform tested in the through-the-thickness direction with corn oil.

The permeability behavior for the Douglas preform is shown in Figure 5.6. Comparing the results of the Douglas preform with that of the stitched Saerbeck preform (Fig. 5.5) indicates that, in general, the Saerbeck has a higher permeability than the Douglas preform. This might result from the greater number of plies present in the Douglas preform than in the Saerbeck preform (54 plies to 24 plies). The larger number of plies in the Douglas preform created more complicated flow paths than those found in the Saerbeck preform. Therefore, the permeability is lower in the Douglas preform than in the Saerbeck preform.

As mentioned earlier in Chapter 3, the different components of the NASA hat-stiffened preform were tested separately. The pre-assembled skin and core preforms were tested individually to determine their through-the-thickness permeability behavior. Four plies of the braided fabric were cut and stacked with the angles coincident to form a preform. The same procedure was used for the $\pm 45°$ 5HS fabric.

The through-the-thickness permeability behavior for the different components of the NASA hat-stiffened preform are given in Figure 5.7. The 5HS $\pm 45°$ weave preform has the highest permeability, followed by the braided preform, the core preform, and then the skin preform, respectively. The lower values of the skin and core preforms were expected due to the more complex nature of these preforms.

5.3 IN-PLANE PERMEABILITY

In-plane permeability tests were conducted in steel fixtures with test section dimensions of either 15.24 cm x 15.24 cm or 5.08 cm x 5.08 cm. The upstream and downstream pressures were measured with precision dial gauges. The flow rate was measured with a graduated cylinder and stopwatch. Preform thickness was monitored

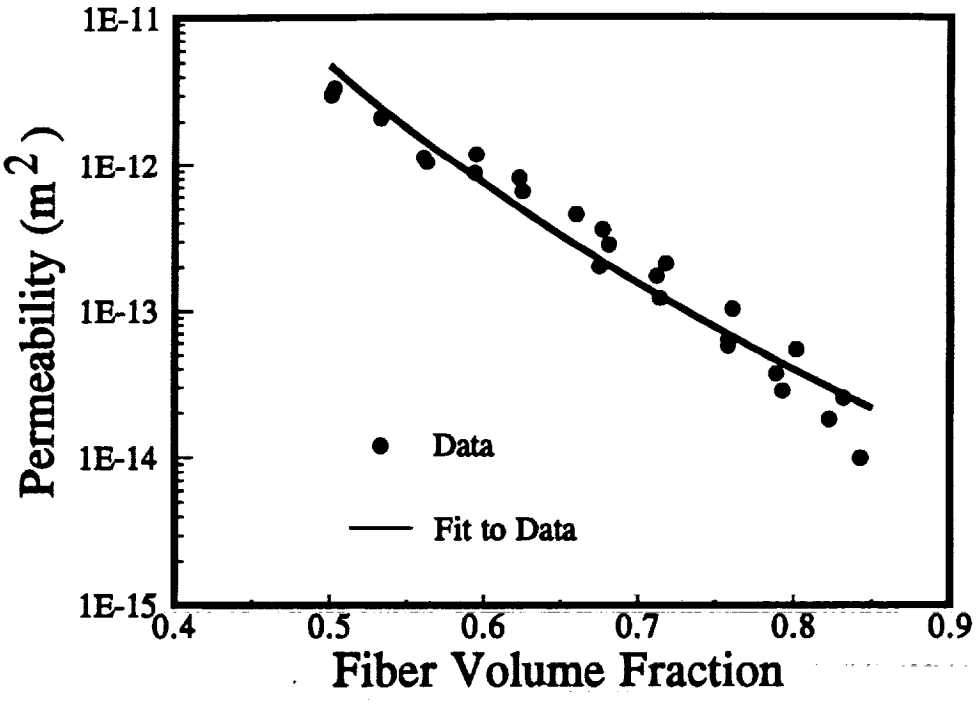

Figure 5.6: Permeability behavior for the Douglas Uniweave preform tested in the through-the-thickness direction with corn oil.

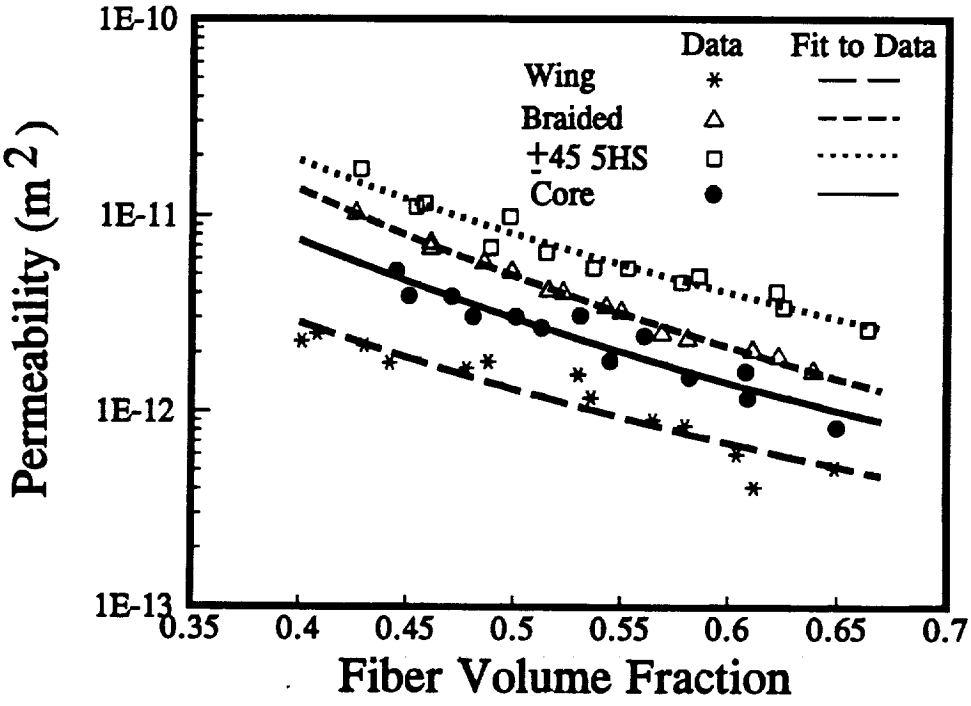

Figure 5.7: Permeability behavior for the NASA hat-stiffened preform tested in the through-the-thickness direction with corn oil.

using digital calipers and this thickness was related to the fiber volume fraction through the areal weight equation (Eq. 4.2.1). A schematic diagram of the in-plane permeability experimental setup is given in Figure 5.8.

For the 162 E-glass fabric, tests were conducted with both corn oil and water to determine the effect of fluid viscosity on permeability behavior. A limited number of tests were conducted with Epon 815. These tests are discussed at the end of the chapter.

The Fiberite HMF 2474 fabric was tested with tap water while the TTI IM7/8HS fabric, the Douglas preform, and the Saerbeck preform were tested with corn oil. The components of the NASA hat-stiffened preform were tested with corn oil. All preforms were tested in the warp and fill directions to determine the effect of flow direction on permeability.

5.3.1 Size Effects

Due to a limited amount material available for in-plane permeability measurements, some of the in-plane tests were performed in the small fixture with a 5.08 cm by 5.08 cm (2 in by 2 in) test section. For those fabrics where the quantity of material was not a problem, in-plane tests were conducted in a steel fixture with a 15.24 cm by 15.24 (6 in by 6 in) test section. A photograph of the 5.08 cm by 5.08 cm fixture is given in Figure 5.9 while a photograph of the 15.24 cm by 15.24 cm fixture is given in Figure 5.10.

To determine if there was a difference in the permeability measurements, in-plane tests were conducted with the 162 E-glass and TTI IM7/8HS fabrics in both fixtures. Corn oil was used in these experiments.

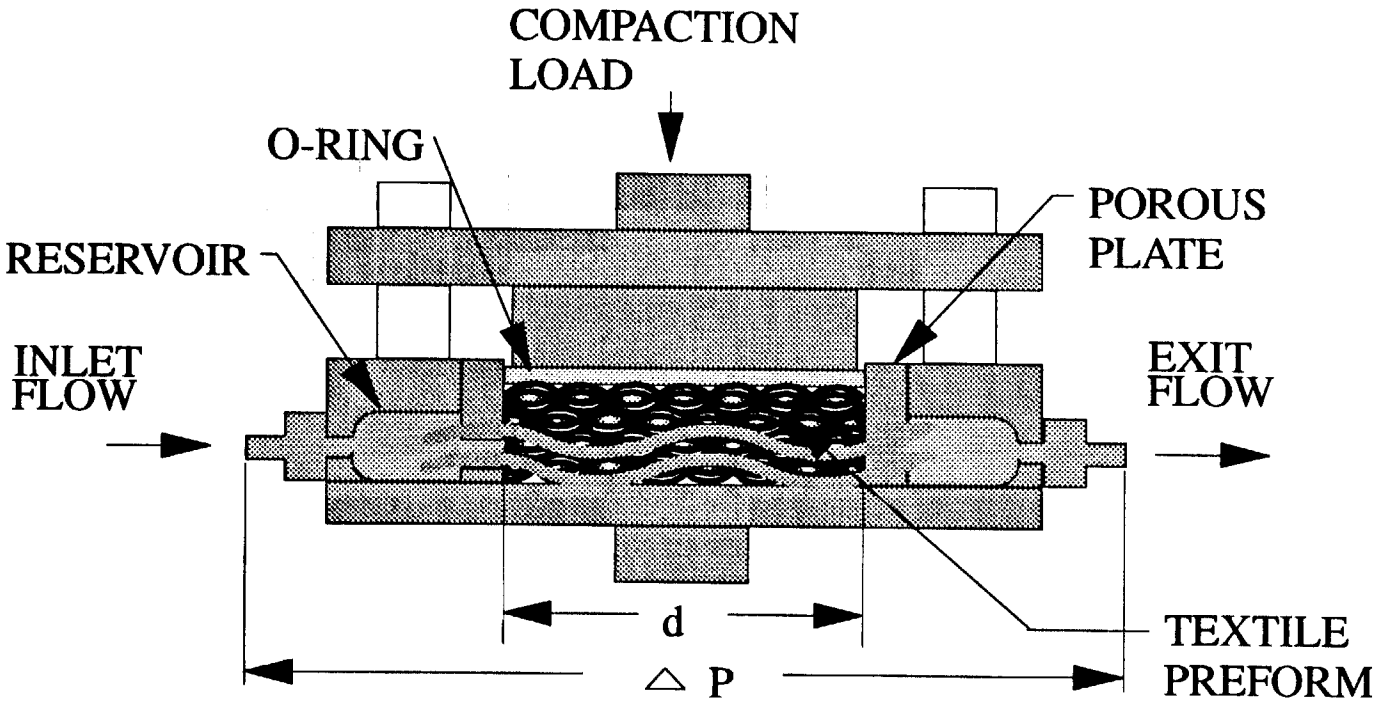

D'ARCY'S LAW:

$$Q = A \frac{S}{\mu} \frac{\triangle P}{d}$$

WHERE:

Q = VOLUMETRIC FLOW RATE
S = PERMEABILITY CONSTANT
μ = VISCOSITY OF FLUID
$\triangle$P/d = PRESSURE GRADIENT
A = AREA NORMAL TO FLOW

Figure 5.8: Schematic of in-plane permeability experimental setup.

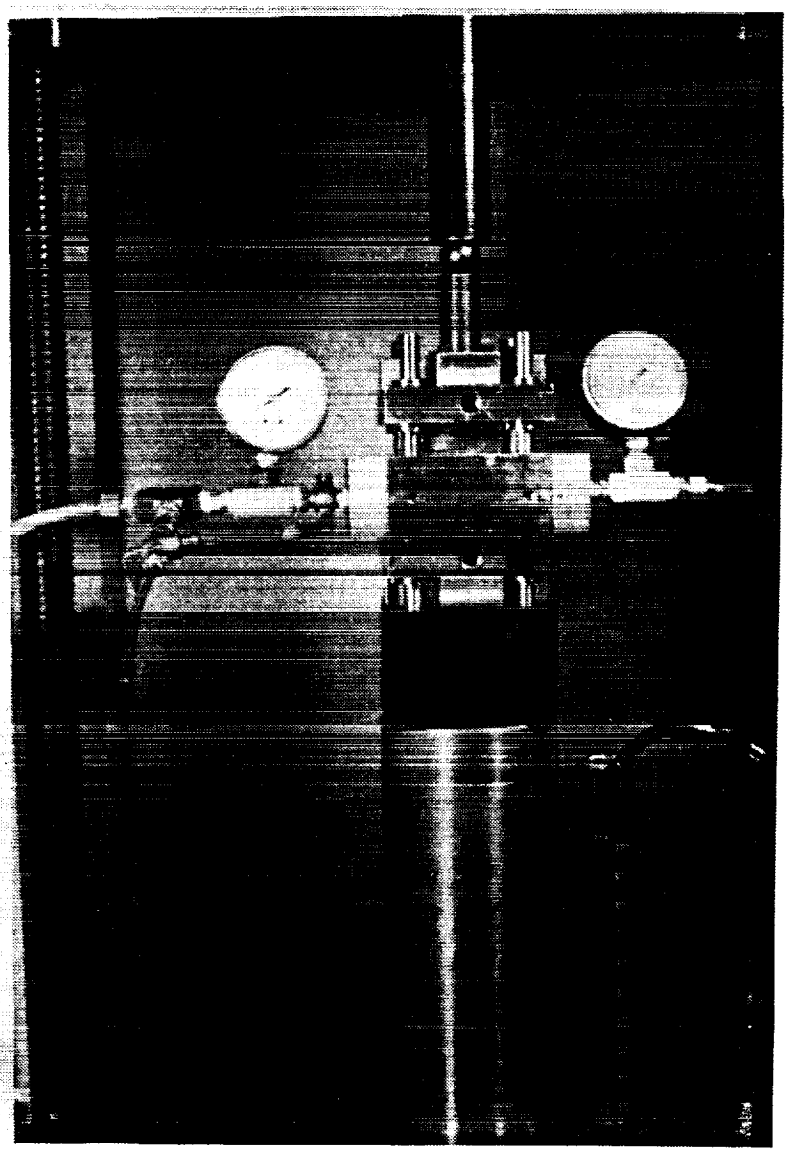

Figure 5.9: Photograph of 5.08 cm by 5.08 cm test fixture used in permeability tests.

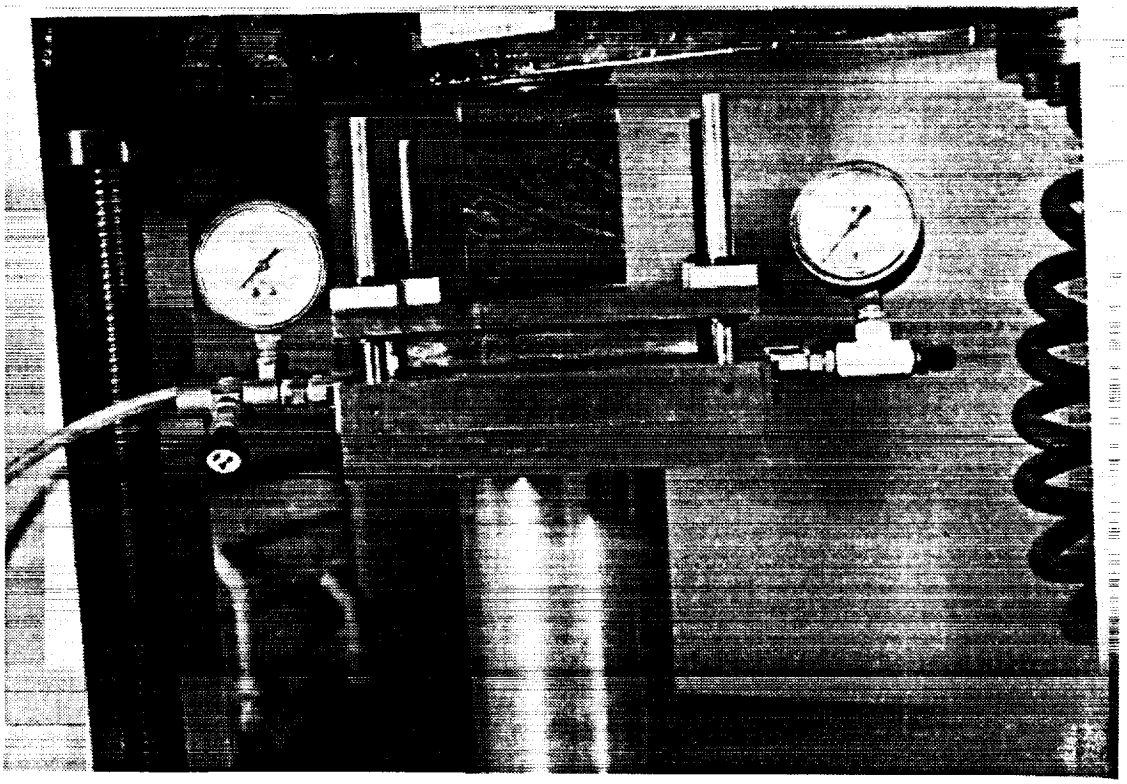

Figure 5.10: Photograph of 15.24 cm by 15.24 cm test fixture used in permeability tests.

Presented in Figure 5.11 are permeability data generated from both fixtures for the warp direction of the 162 E-glass fabric. Likewise, in Figure 5.12, the permeability data for the fill direction of the 162 E-glass fabric is shown. The permeability values measured in the 5.08 cm by 5.08 cm fixture are slightly higher than those from the 15.24 cm by 15.24 cm fixture for the warp direction. For the fill direction, the measured permeabilities from the two fixtures are virtually identical.

A comparison of permeabilities measured in the two fixtures for the warp direction of the TTI fabric is shown in Figure 5.13. Similarly, Figure 5.14 shows the comparison for the fill direction permeability behavior of the TTI fabric. From these two figures, it can be seen that the permeabilities measured in the 5.08 cm by 5.08 cm fixture are lower than those measured in the larger fixture.

The permeabilities measured in the 15.24 cm by 15.24 cm fixture are thought to be more accurate due to the larger sample used in the test. The larger specimen provides a more representative sample than the smaller sample. Also the larger fixture is not as susceptible to leakage as the smaller fixture. The permeability values measured in the large fixture agreed with results obtained from flow visualization and advancing front experiments. Whenever possible, the 15.24 cm by 15.24 cm fixture was used to perform the in-plane permeability experiments.

5.3.2 Results

The 162 E-glass, TTI IM7/8HS, Saerbeck, and Douglas fabrics were tested in the fixture with the 15.24 cm by 15.24 cm test section. The Fiberite fabric were tested in the fixture with a 5.08 cm by 5.08 cm test section. Due to the limited quantities of material available from the NASA hat-stiffened preform, all in-plane permeability tests were conducted with the smaller 5.08 cm by 5.08 cm test fixture.

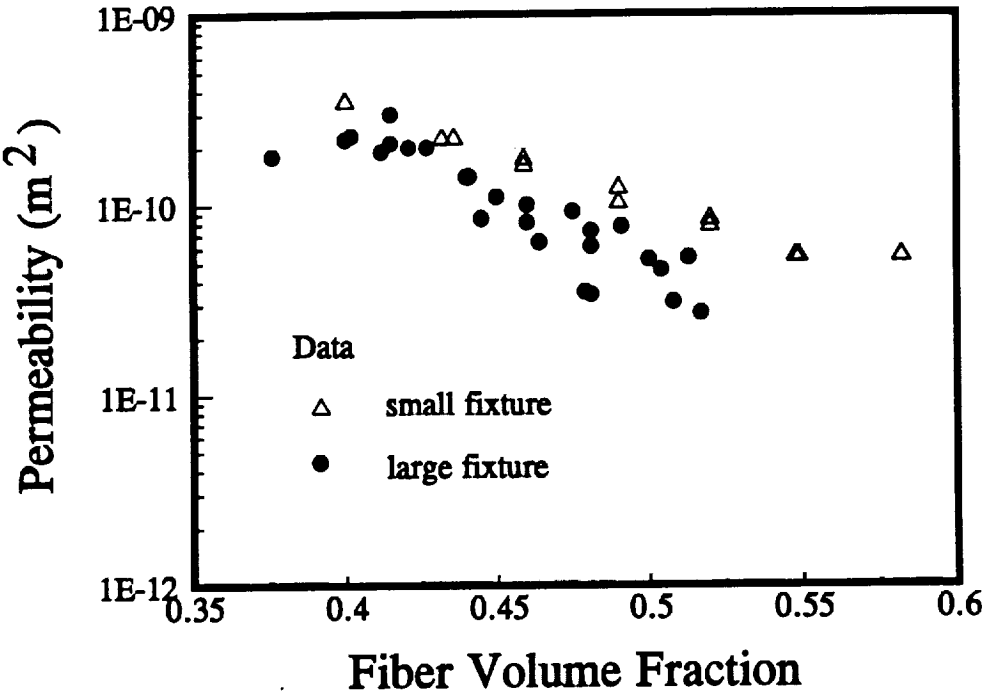

Figure 5.11: Comparison between permeability data measured in the two fixtures for the warp direction of 162 E-glass fabric.

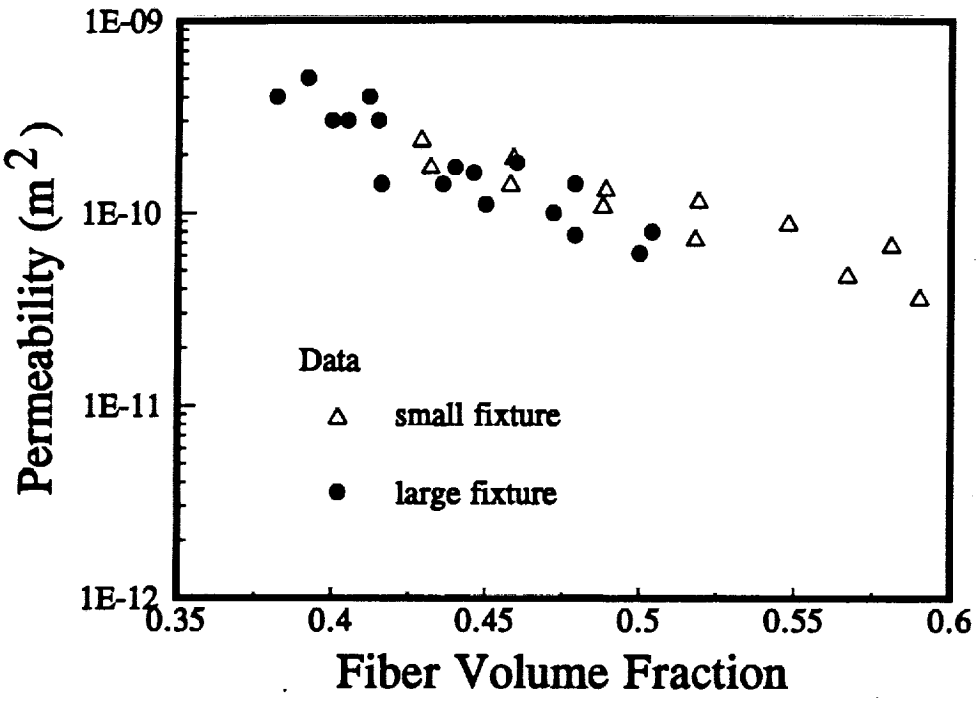

Figure 5.12: Comparison between permeability data measured in the two fixtures for the fill direction of 162 E-glass fabric.

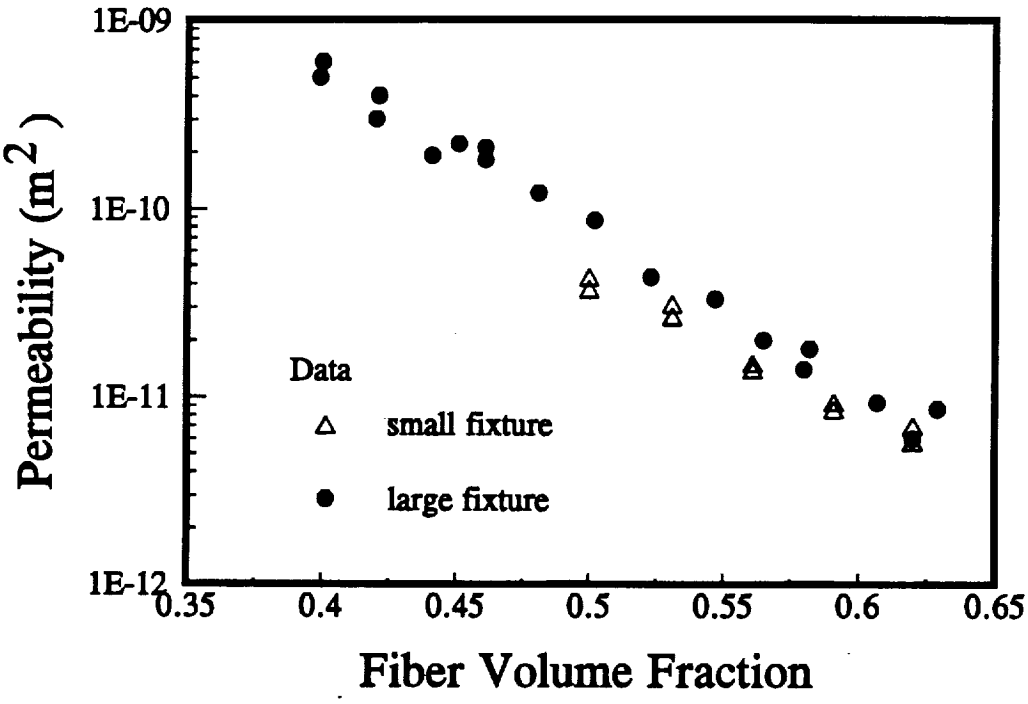

Figure 5.13: Comparison between permeability data measured in the two fixtures for the warp direction of TTI IM7/8HS fabric.

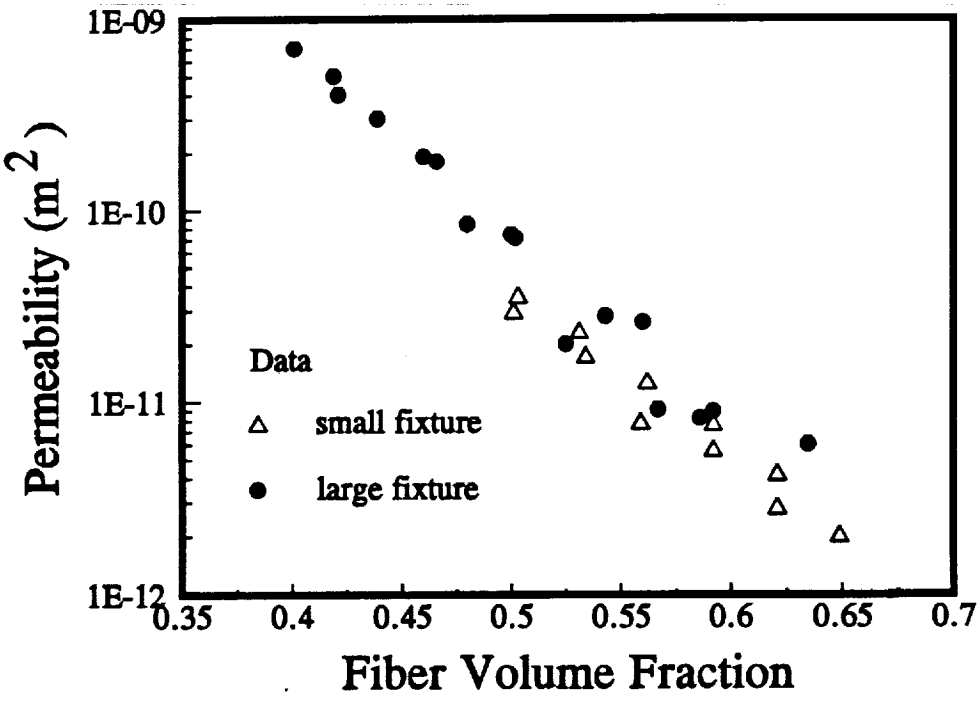

Figure 5.14: Comparison between permeability data measured in the two fixtures for the fill direction of TTI IM7/8HS fabric.

Once again, the permeability versus fiber volume fraction data were fit to a power law regression model. The equation was given in the preceding section (Eq. 5.2.1). The constants generated from the regression fit are given in Table 5.3 for the individual preforms. The constants for the NASA hat-stiffened preform are given in Table 5.4.

Shown in the Figures 5.15 and 5.16 are a comparison between the permeability behavior for the 162 E-glass fabric tested with water and corn oil. The data for the corn oil and water are similar for both the warp and fill directions except for the low fiber volume fractions in the warp direction. This difference may be the result of channeling, or fluid leaking around the fabric, at the low fiber volume fractions. There is virtually no difference between the permeability behavior for the corn oil and water. This tends to support the earlier statement that the fluid used during these tests is not critical provided accurate viscosity measurements are made.

The warp and fill direction permeability data for the TTI IM7/8HS fabric tested with corn oil are presented in Figures 5.17 and 5.18, respectively. For the TTI preform, the permeability curves for the two directions are approximately the same.

In Figure 5.19, the permeability as a function of fiber volume fraction for the Fiberite HMF 2474 fabric is shown. The fill direction has a higher permeability than the warp direction for values of fiber volume ranging from 45% - 60%. The difference in values is small at low fiber volume fractions but increases as the amount of porosity in the preform is reduced. This indicates that the flow paths in the warp direction are closed off faster than the paths in the fill direction as the fiber volume fraction is increased.

Table 5.3: Experimental constants for in-plane permeability as a function of fiber volume fraction.

Fabric	Warp		Fill		Fluid Used
	a	b	a	b	
162 E-glass	4.0E-13	-6.7901	7.4E-13	-6.5861	Corn oil / Water
TTI IM7/8HS	8.1E-14	-9.7706	2.7E-14	-11.1622	Corn oil
Fiberite HMF 2474	8.3E-14	-7.6209	2.9E-13	-6.1626	Water
Saerbeck	1.4E-15	-19.4906	3.1E-18	-29.8227	Corn oil
Douglas	8.4E-14	-9.4624	1.4E-14	-10.9987	Corn oil

Table 5.4: Experimental constants for in-plane permeability as a function of fiber volume fraction for the NASA hat-stiffened preform.

Fabric	Warp		Fill		Fluid Used
	a	b	a	b	
Skin	2.6E-13	-7.1564	2.5E-12	-4.3886	Corn oil
Braided	3.8E-12	-4.115	2.0E-11	-1.5693	Corn oil
±45° 5HS	1.3E-11	-3.5276	1.7E-11	-3.1768	Corn oil
Core	6.9E-12	-4.3095	8.0E-12	-3.2019	Corn oil

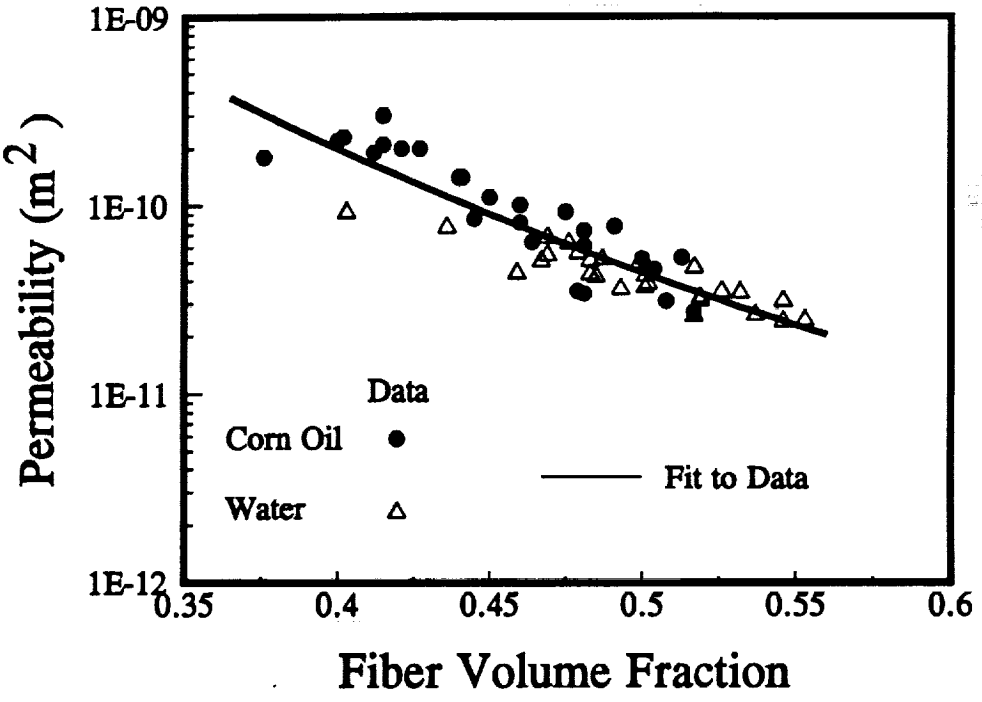

Figure 5.15: Permeability behavior for the 162 E-glass preform tested in the warp direction with corn oil and water.

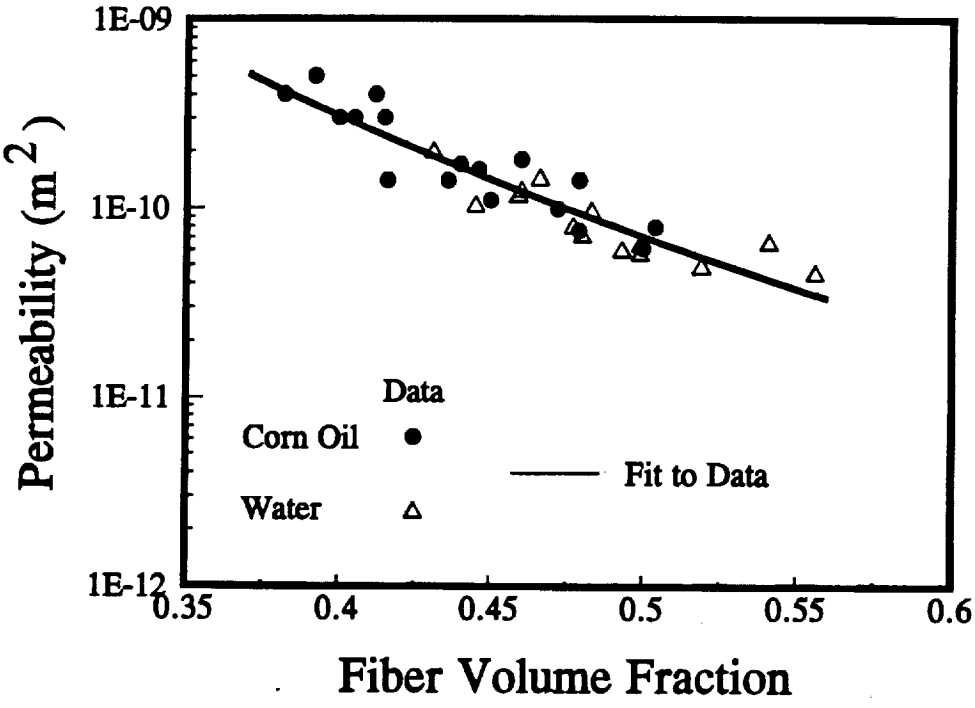

Figure 5.16: Permeability behavior for the 162 E-glass preform tested in the fill direction with corn oil and water.

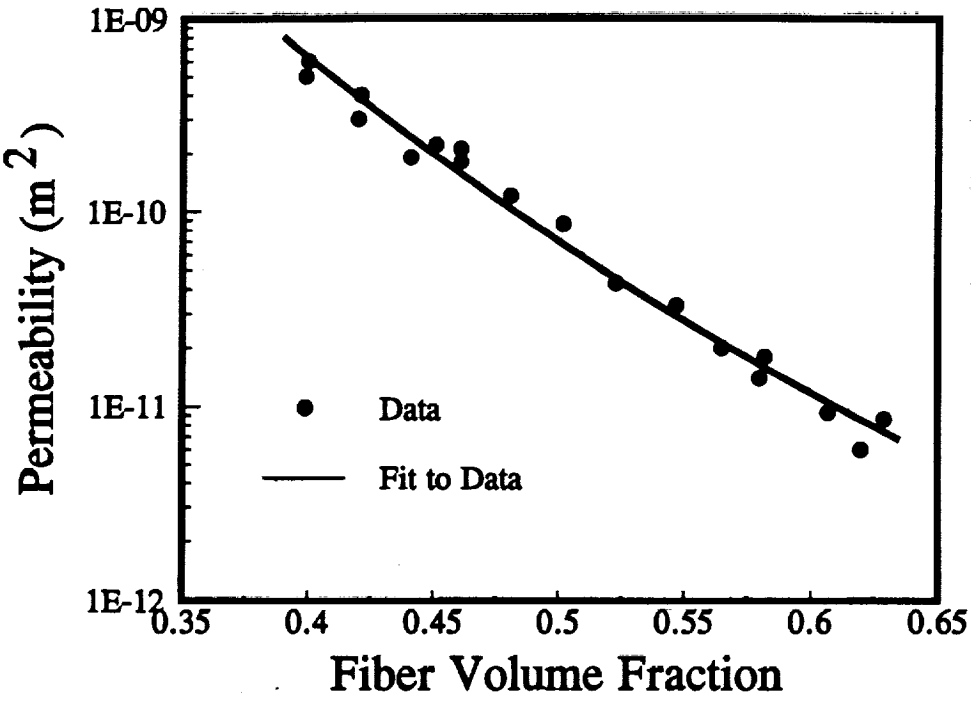

Figure 5.17: Permeability behavior for the TTI IM7/8HS preform tested in the warp direction with corn oil.

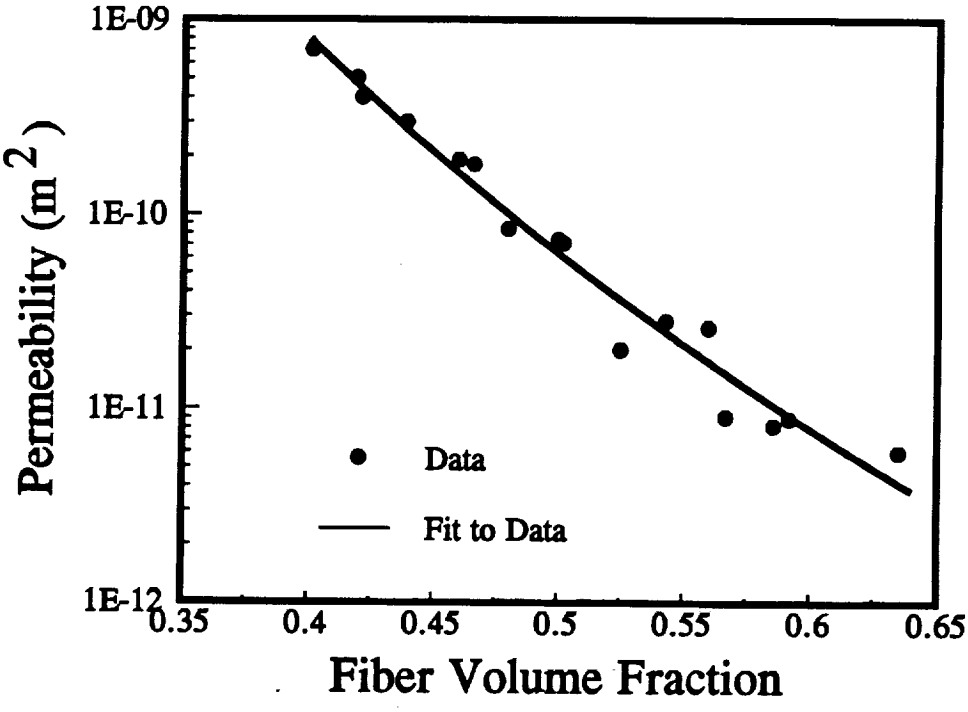

Figure 5.18: Permeability behavior for TTI IM7/8HS preform tested in the fill direction with corn oil.

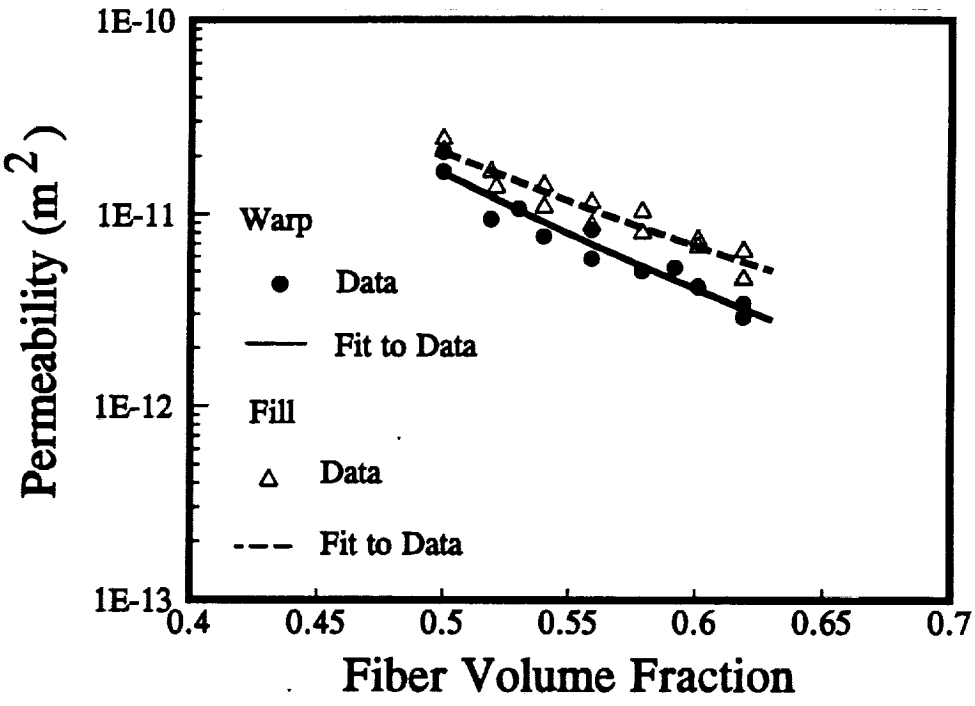

Figure 5.19: Permeability behavior for the Fiberite HMF 2474 preform tested in the warp and fill directions with water.

The permeability behavior of the Saerbeck preform is given in Figure 5.20. Due to a limited amount of material, only one test was performed in each direction. For flow normal or 90° to the Kevlar stitching, a drastic reduction in permeability occurs as the fiber volume fraction is increased. For the case of flow in the 0° direction or along the stitching, a more gradual reduction in permeability is observed. Initially, the permeability along the stitching is lower than that of the case for flow across the stitching. However, the permeability along the stitching becomes greater as the fiber volume fraction is increased.

This behavior may be a result of the layup pattern in which only 12% of the tows are placed in the 90° direction. The remaining 88% are split evenly between the 0° and ±45° direction. Flow normal to the Kevlar stitching encounters greater resistance than flow in the 0° direction due to the larger amount of tows in the 0° direction.

In-plane permeabilities for the Douglas preform are shown in Figure 5.21. It can be seen from these curves that the permeability along the stitching (0°) is higher than the permeability across the stitching (90°) for the range of volume fractions tested. Again, this is the result of the greater number of tows placed in the 0° direction.

The warp (along the Kevlar stitching) and fill (across the Kevlar stitching) permeability curves of the skin preform of the NASA hat-stiffened preform are shown in Figure 5.22. The fill direction permeability is greater than the warp direction permeability for fiber volume fractions greater than 0.45.

The warp and fill permeabilities of the braided fabric of the NASA hat-stiffened preform are shown in Figure 5.23. The curves indicate that the permeabilities are nearly the same for fiber volume fractions less than 0.57.

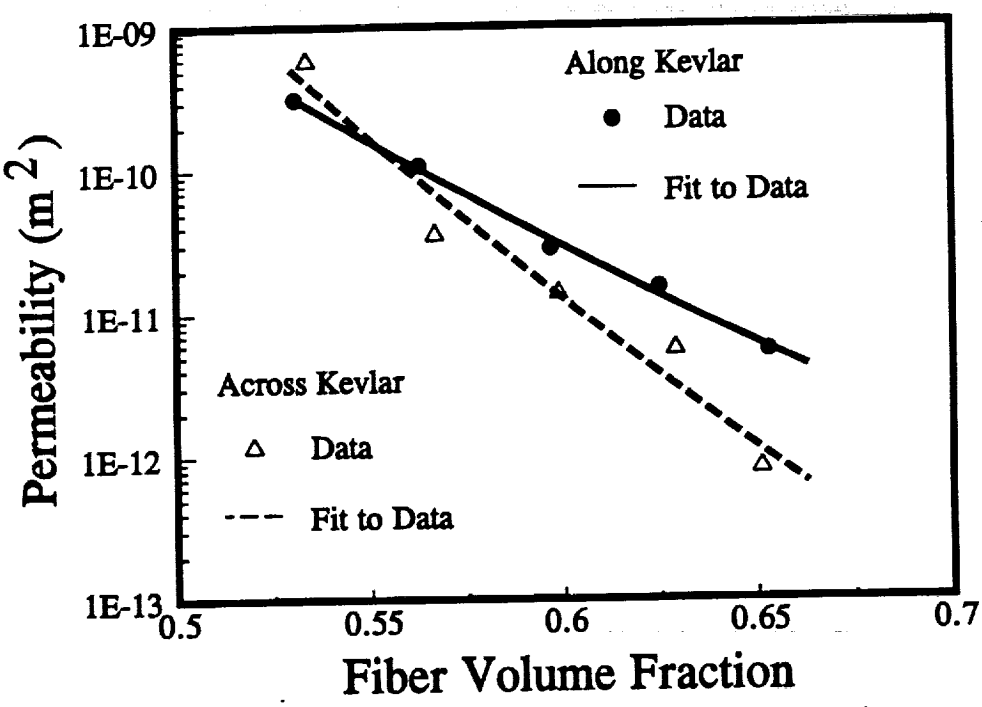

Figure 5.20: Permeability behavior for the Saerbeck preform tested along and across Kevlar stitching with corn oil.

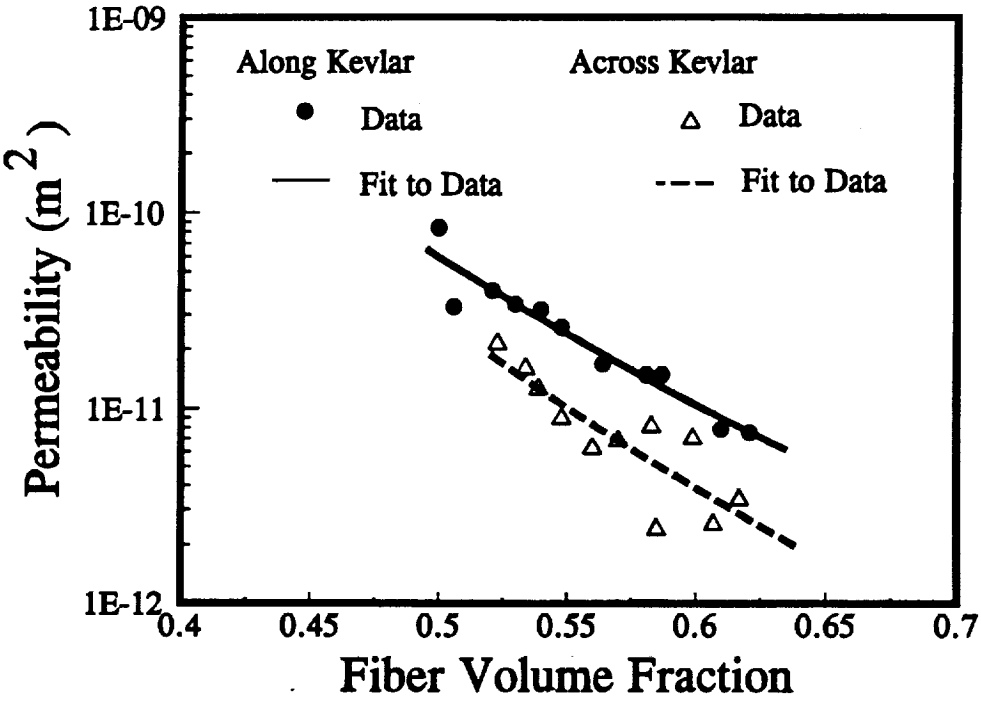

Figure 5.21: Permeability behavior for the Douglas Uniweave preform tested across and along fibers with corn oil.

C-2

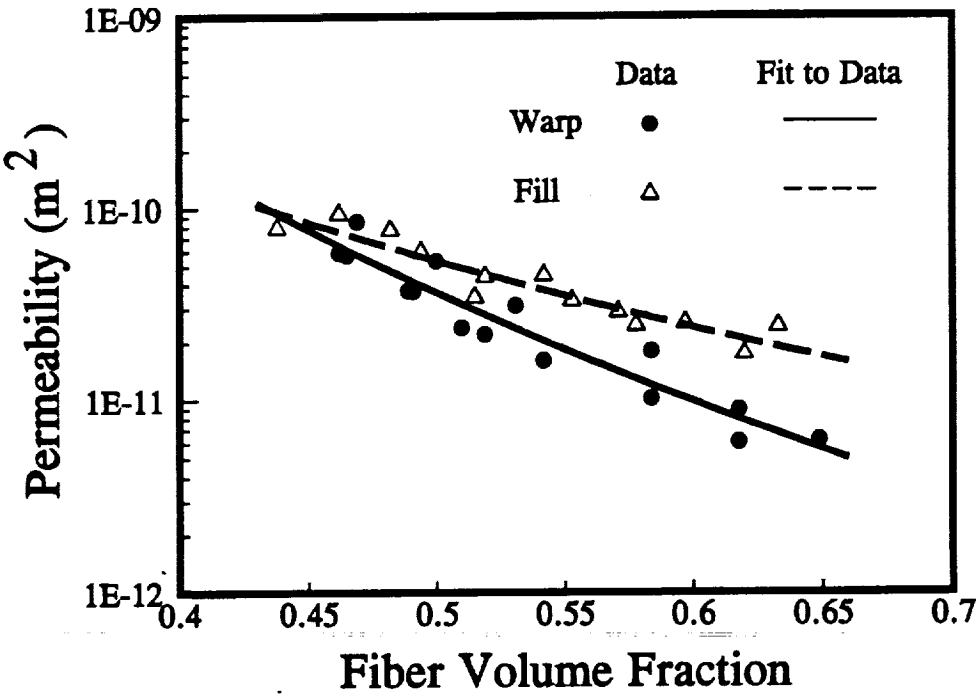

Figure 5.22: Permeability behavior for the skin preform of the NASA hat-stiffened preform tested with corn oil.

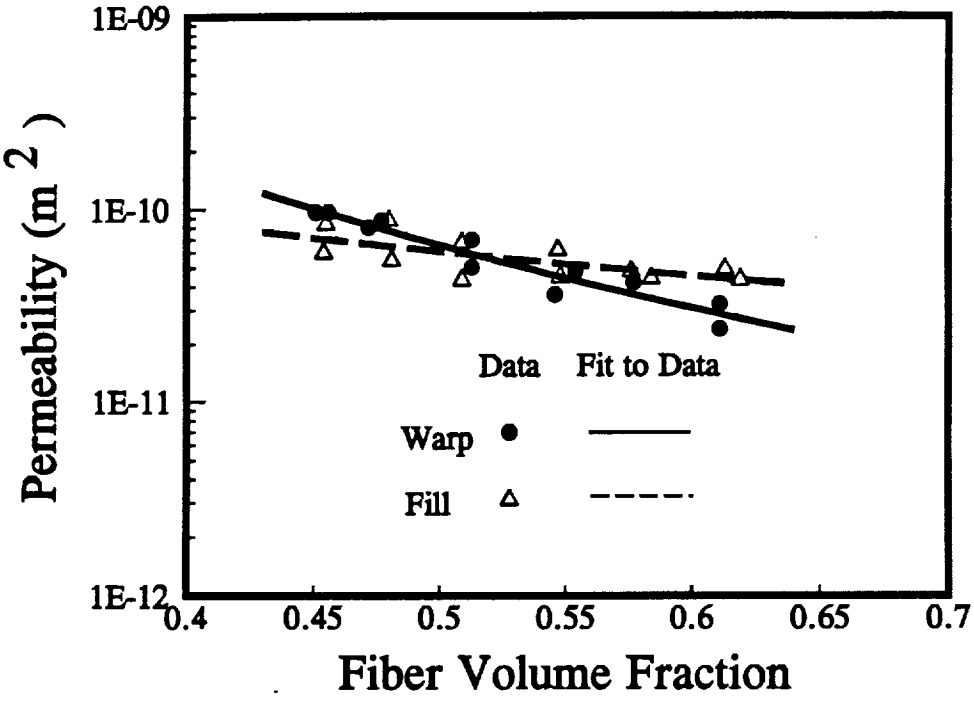

Figure 5.23: Permeability behavior for the braided fabric of the NASA hat-stiffened preform tested with corn oil.

The permeabilities for the ±45° 5HS fabric are presented in Figure 5.24. From the figure, it can be seen that there is virtually no difference between the permeability behavior in the two directions, as expected.

The permeability of the core preform is presented in Figure 5.25. Again, the warp direction is considered to be along the Kevlar stitching while the fill direction is normal to the Kevlar stitching. Unlike the skin preform, the permeability in the warp direction is higher than that in the fill direction.

5.3.3 In-plane Epoxy Tests

As mentioned earlier in the chapter, a limited number of steady state in-plane permeability tests were conducted with an epoxy resin. The epoxy used was Epon 815 with a measured viscosity of 1200 centipoise. All of these tests were conducted using a constant displacement injection pump and therefore the fluid was injected at a constant flow rate. The pressure associated with each flow rate was measured through the use of a pressure transducer. All tests were conducted in the warp direction of either the 162 E-glass or TTI IM7/8HS fabrics.

Shown in Figure 5.26 is a comparison between the permeability values for the warp direction of 162 E-glass when tested with corn oil and Epon 815. From the figure, it can be seen that the permeability measurements were similar for the two fluids. Although the permeabilities measured with Epon 815 were slightly higher at the higher fiber volume fractions, the data still fall within the scatter range of the corn oil data.

A comparison between the permeabilities measured with corn oil and Epon 815 in the warp direction of the TTI IM7/8HS preform is presented in Figure 5.27. The permeabilities measured with Epon 815 are similar to the permeabilities measured

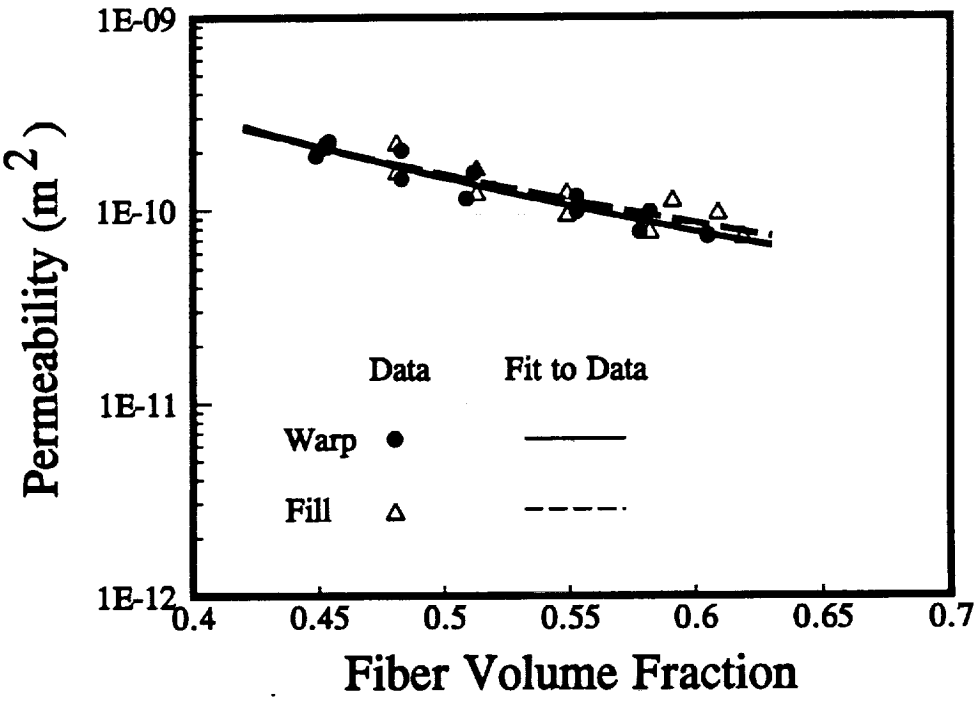

Figure 5.24: Permeability behavior for the ±45° 5HS fabric of the NASA hat-stiffened preform tested with corn oil.

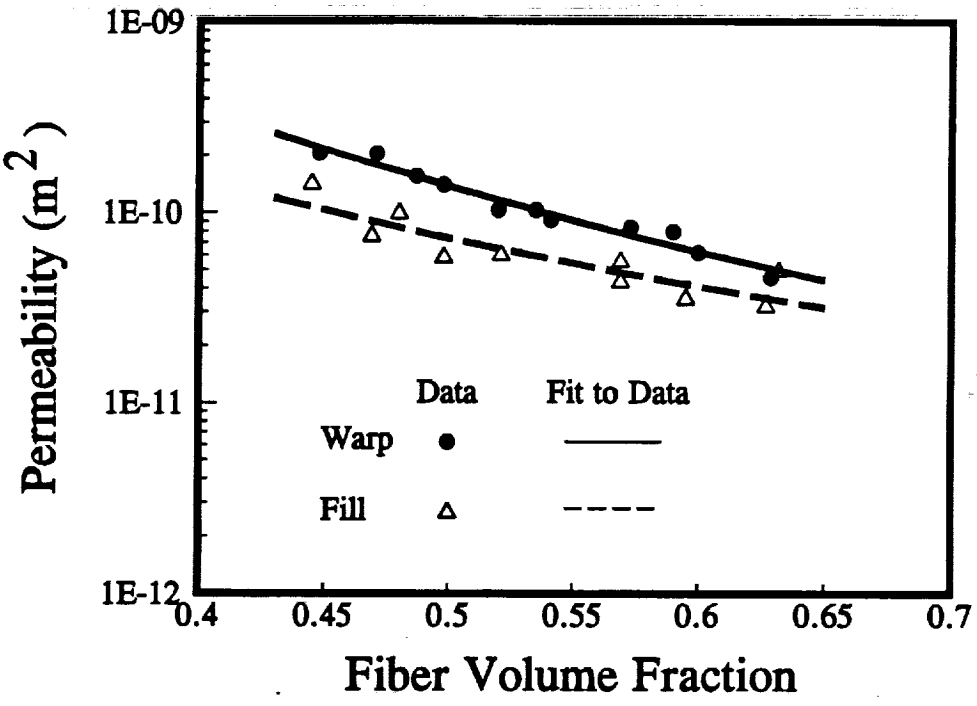

Figure 5.25: Permeability behavior for the core preform of the NASA hat-stiffened preform tested with corn oil.

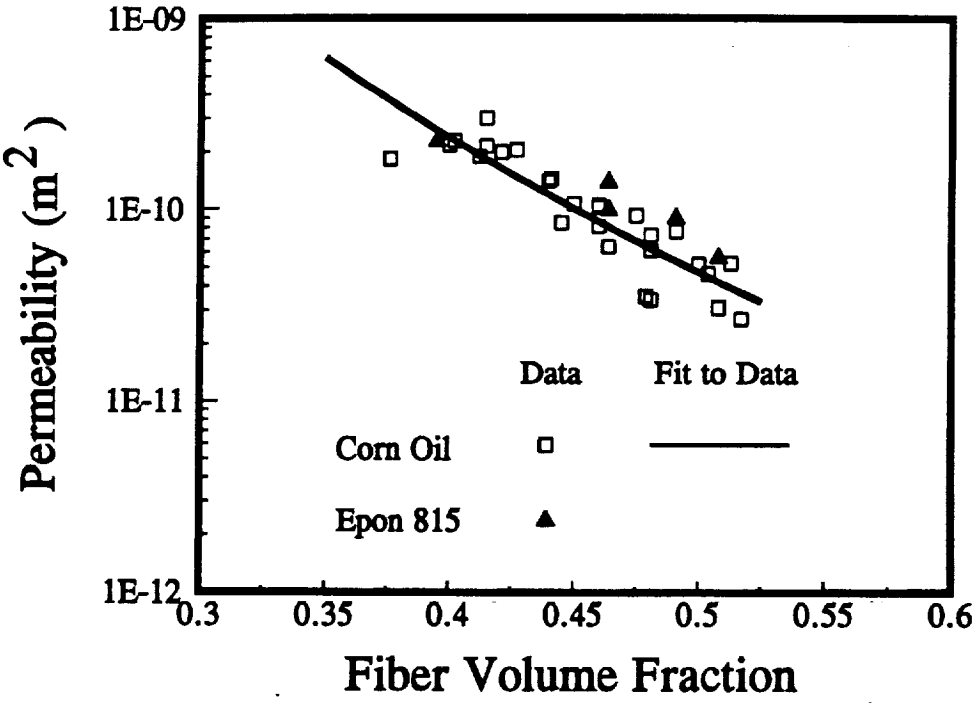

Figure 5.26: Comparison between the warp direction permeability of 162 E-glass measured with corn oil and Epon 815.

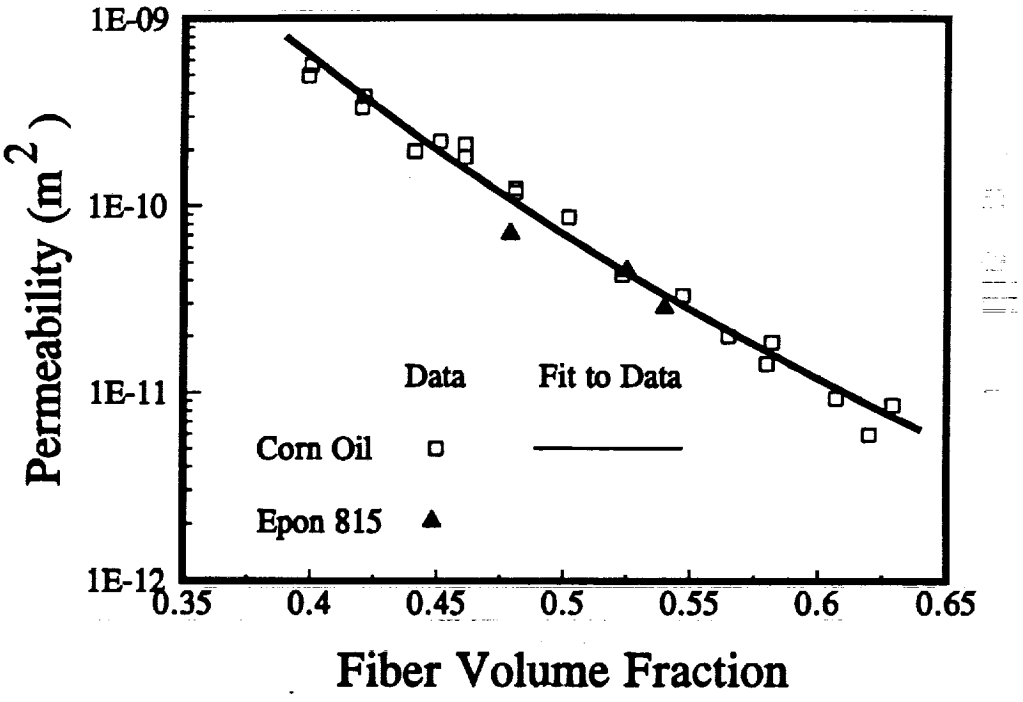

Figure 5.27: Comparison between the warp direction permeability of TTI IM7/8HS measured with corn oil and Epon 815.

with corn oil at three different fiber volume fractions.

The results from these two figures again supports the earlier observation that the fluid used to conduct the steady state permeability tests is not critical provided accurate viscosity measurements are made.

6.0 ADVANCING FRONT PERMEABILITY

Unlike the steady state permeability method which measures the permeability of a saturated preform, the advancing front test measures the permeability of the fluid infiltrating the dry preform. Tests were conducted with corn oil and Epon 815, both diluted and undiluted, to determine the permeability of dry 162 E-glass preforms. Tests were also conducted with TTI IM7/8HS fabric and corn oil. These values were then compared to results from the steady state method used in the previous chapter.

6.1 THEORETICAL BACKGROUND

Advancing front permeability is a measure of how a fluid infiltrates a dry preform. The governing relationship used in these experiments is one-dimensional Darcy's Law which is expressed as

$$\frac{Q}{A} = -\frac{S}{\mu}\frac{dP}{dx} \qquad (6.1.1)$$

where Q is the volumetric flow rate, A is the area, and S is the permeability constant. The fluid viscosity is denoted by μ.

Two methods were used for these experiments. In the first, the fluid was injected by a constant pressure paint pot. In the second method, a constant displacement injection pump was used. Thus, a constant flow rate into the mold was attained.

6.1.1 Constant Pressure Injection

Starting with the relationship between superficial velocity and interstitial velocity,

$$\frac{Q}{A} = q = v \frac{A_{flow}}{A_{total}} = v\,\phi = \frac{dx}{dt}\,\phi \qquad (6.1.2)$$

where q is the superficial velocity, v is the interstitial velocity, and ϕ is the porosity. Substituting this relationship into equation (6.1.1) and rewriting the pressure gradient, $\frac{dP}{dx}$, as $-\frac{\Delta P}{x}$ yields

$$\frac{dx}{dt}\,\phi = \frac{S}{\mu}\,\frac{\Delta P}{x} \qquad (6.1.3)$$

By integrating the above equation we obtain an expression for the flow front position, x, as a function of time t

$$x^2 = \left(\frac{2\,S\,\Delta P}{\mu\,\phi}\right) t \qquad (6.1.4)$$

The permeability of the preform can be determined by measuring the slope of the x^2 versus time t plot and performing the following calculation

$$S = \frac{slope\;\mu\;\phi}{2\Delta P} \qquad (6.1.5)$$

6.1.2 Constant Flow Rate Injection

For the case of constant flow rate injection, direct integration of equation (6.1.1) yields the following relationship between pressure and distance

$$P = \frac{Q\,\mu}{S\,A}\,x \qquad (6.1.6)$$

where the variables were defined in equation (6.1.1). By plotting the pressure, P, as a function of distance, x, and measuring the slope of the linear least squares fit to the data, the permeability can be expressed as

$$S = \frac{Q\,\mu}{slope\ A} \qquad (6.1.7)$$

6.2 EXPERIMENTAL SETUP

For these experiments, a matched metal mold with a fixed cavity depth of 0.635 cm was used. The mold had a length of 17.11 cm and a width of 15.13 cm. A plexiglass window was set into the top and side of the mold. Lines were etched in the window every 1.27 cm starting 1.27 cm from the inlet port. This allowed the fluid flow front position to be monitored with respect to time. A schematic diagram further explaining the advancing front test is given in Figure 6.1. A picture of the fixture used in this test is shown in Figure 6.2.

Fluid was injected into the mold by two methods. For the majority of the tests, the fluid was injected using a constant pressure pot injector system. For the 162 E-glass/Epon 815 and TTI IM7/8HS /corn oil tests, a constant flow rate injection pump (Radius Engineering, Floware 2100 RTM) was used. For both cases, the pressure was monitored at the inlet as the fluid infiltrated the preform. The time necessary for the fluid to progress 1.27 cm increments was recorded with a stop

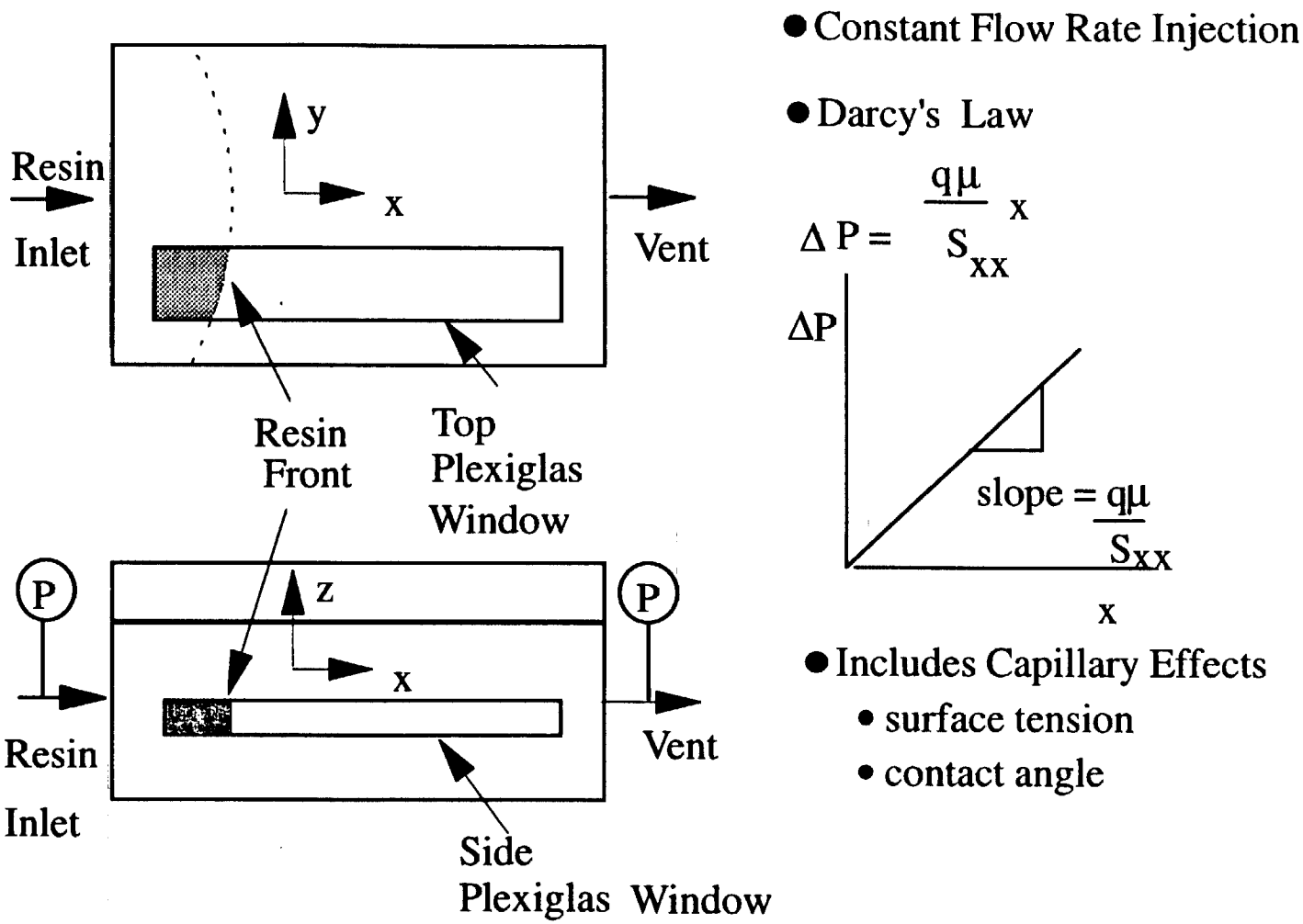

Figure 6.1: Schematic diagram of advancing front permeability experimental setup.

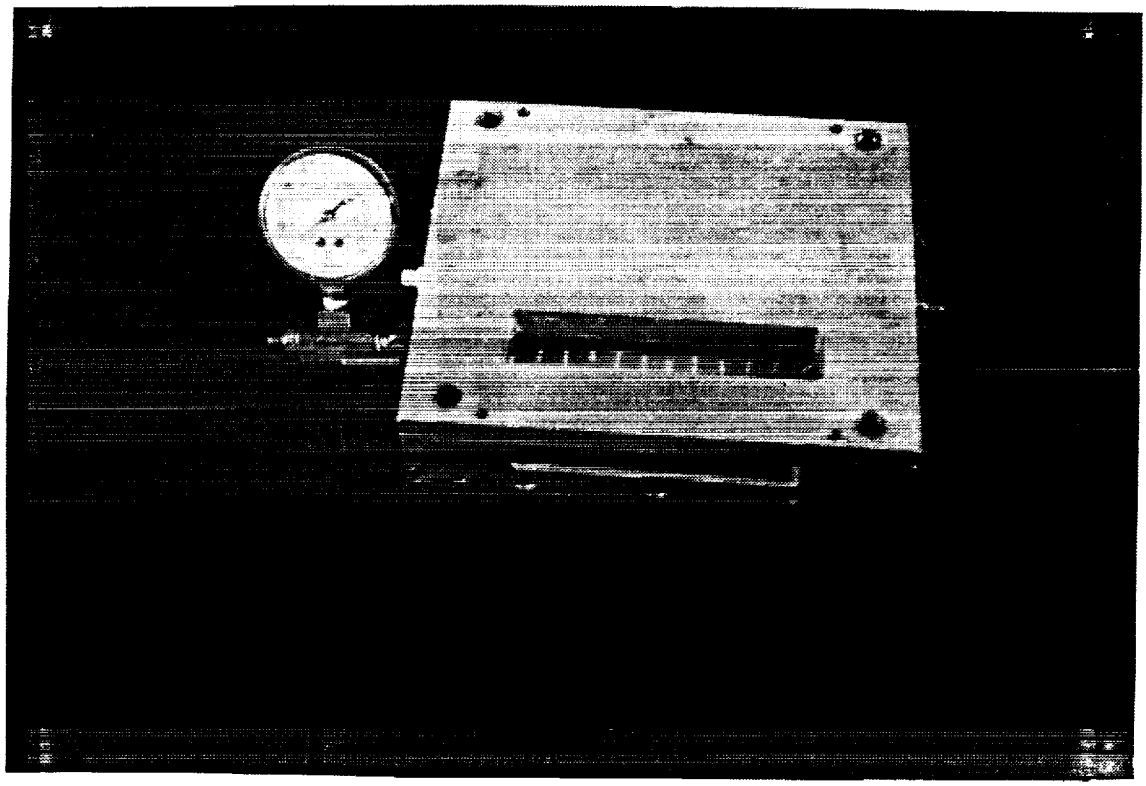

Figure 6.2: Photograph of test fixture used in advancing front permeability experiments.

watch along with the pressure setting at that time. The viscosity of the fluid was measured with a Brookfield DV-II viscometer prior to each test. Then, by following the procedures outlined in Section 6.1, the permeability of the dry preform could be determined.

6.3 RESULTS

Shown in Figure 6.3 is a comparison between steady state and advancing front permeability values for the 162 E-glass/corn oil system. All tests were conducted with the constant pressure pot injection system. The corn oil had an average viscosity of 60 centipoise and was dyed with Oil Red O dye to ensure contrast between the oil and the glass fabric.

The steady state permeability data are represented by the open circles. The solid line is a power law regression fit to the steady state data. Six advancing front tests were conducted at a fiber volume fraction of 43.1% while two tests were conducted at a fiber volume fractions of 47.9%. The solid diamonds represent the average of the advancing front data for a particular fiber volume fraction with the error bars representing the standard deviation.

Analysis of the data indicates that the advancing front data falls well within the scatter range of the steady state data. In particular, the advancing front data at 43.1% fall directly on the regression curve for the steady state data. The advancing front data at 47.9% are slightly higher than the steady state curve fit but still fall within the wide scatter range of the steady state values.

A comparison between the steady state and advancing front permeabilities for the 162 E-glass/Epon 815 system is shown in Figure 6.4. In this case, the steady state

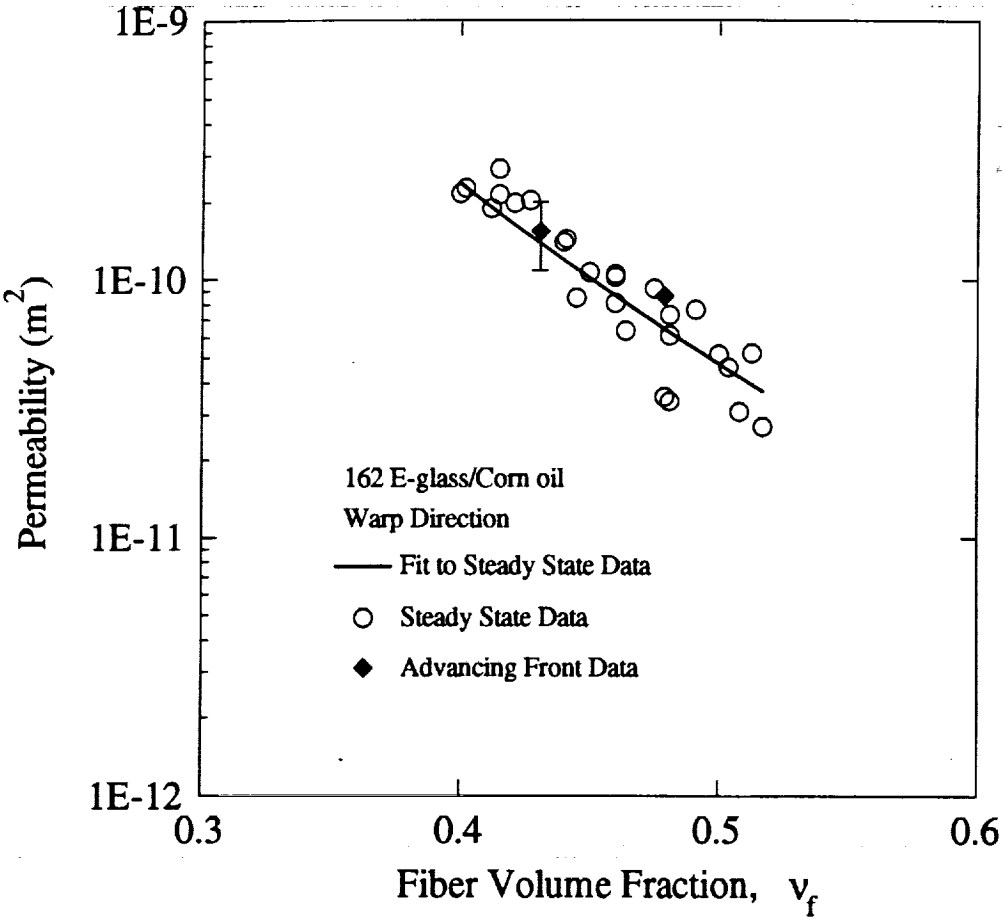

Figure 6.3: Comparison between steady state and advancing front permeability for the 162 E-glass/corn oil system.

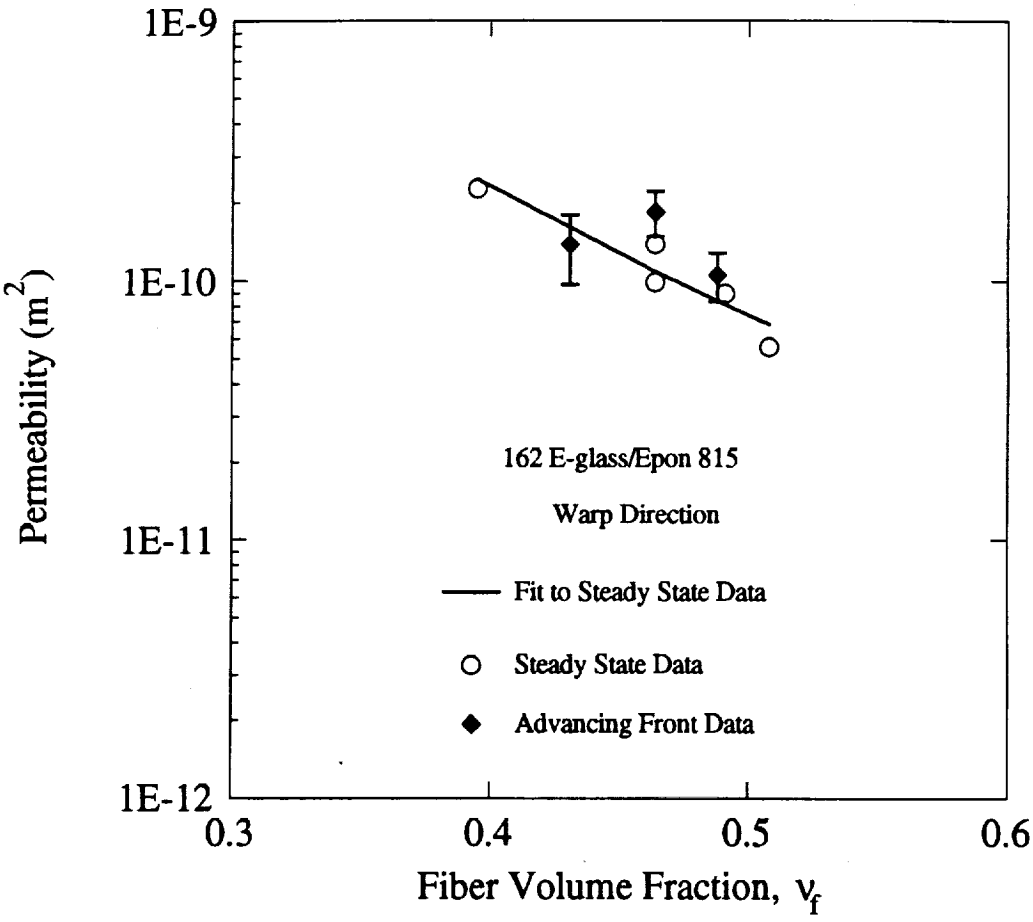

Figure 6.4: Comparison between steady state and advancing front permeability for the 162 E-glass/Epon 815 system.

and 43.1% fiber volume fraction advancing front tests were conducted with Epon 815 that had a nominal viscosity of 1200 centipoise. For these tests, the constant displacement injection pump was used. For the advancing front tests of 46.4% and 48.8% fiber volume fraction, the Epon 815 was diluted with Butyl Glycidyl Ether to a viscosity of 215 centipoise.

In this figure, the open circles again represent the steady state permeability data. The solid line is the curve fit to these data. The solid diamonds represent the average of the advancing front data with the error bars representing the standard deviation of the tests. There were four tests at a fiber volume fraction of 43.1%, two tests at a fiber volume fraction of 46.4%, and two tests at a fiber volume fraction of 48.8%.

From this figure, it can be seen that the advancing front data at 43.1% falls directly on the curve fit to the steady state data. The data at 46.4% and 48.8% fall somewhat above the steady state curve fit. By diluting the epoxy for the higher fiber volume fraction tests, the manner in which the glass fiber and epoxy interact may have changed which could have an effect on the permeability behavior.

A comparison between the steady state and advancing front permeability behavior for the TTI IM7/8HS - corn oil system is presented in Figure 6.5. In this case, the steady state permeability tests were conducted with the constant pressure injection system while the advancing front tests were conducted with the constant flow rate injection system. Again, the advancing front data are represented by the solid diamonds with the steady state data represented by the open circles. Two advancing front experiments were conducted at fiber volume fractions of 58.3% and 62.0%. From Figure 6.5, it can be seen that the advancing front values are similar to the steady state values.

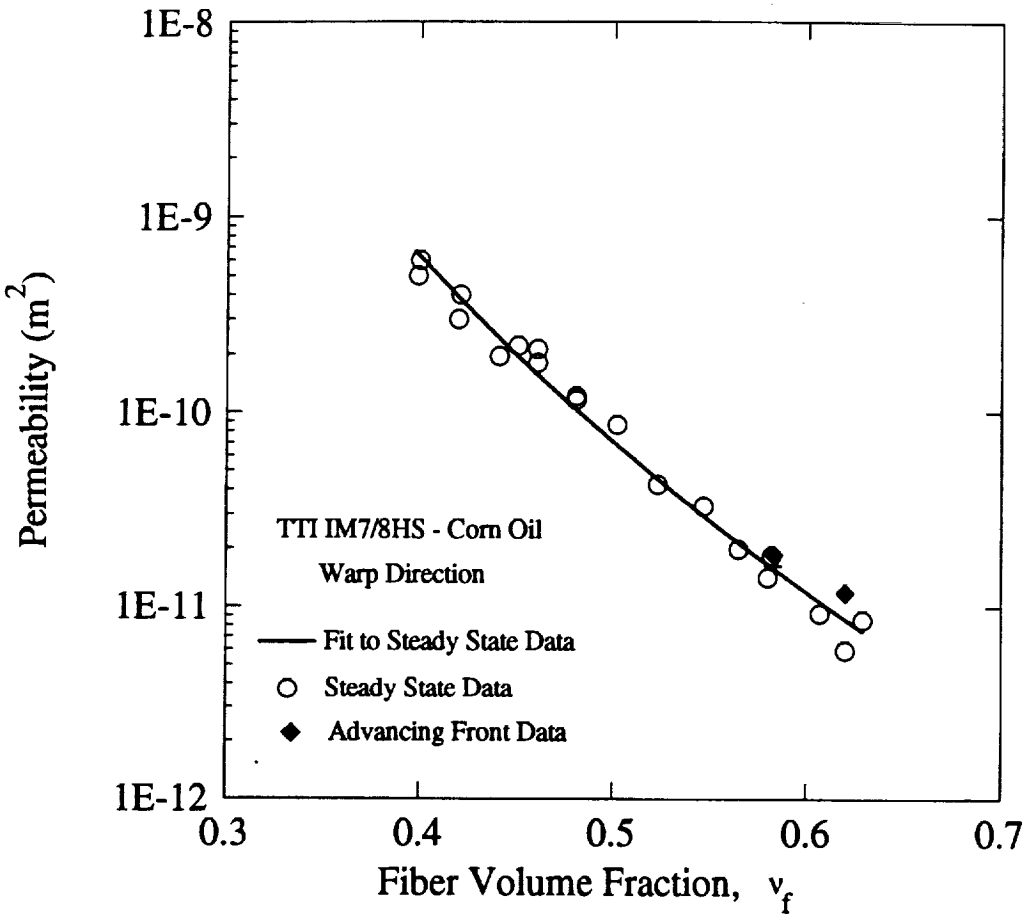

Figure 6.5: Comparison between steady state and advancing front permeability for the TTI IM7/8HS/Corn Oil system.

As mentioned in Section 2.4, the saturation of a medium infiltrated by the resin depends on the capillary number [25]. From equation (2.4.5), the capillary number can be written as

$$C_a = \frac{\mu V}{\gamma_{LV}} \tag{6.3.1}$$

where V is the resin interstitial velocity, μ is the resin viscosity, and γ_{LV} is the surface tension of the infiltrating fluid.

The capillary number was determined from equation (6.3.1) for the advancing front tests conducted at constant injection velocity. Likewise, the advancing front permeability for each test was calculated. Figure 6.6 shows the relationship between the advancing front permeability and capillary number. From this figure, it can be seen that the permeability is independent of capillary number for the range of values given. This is the case for both the corn oil and epoxy tests.

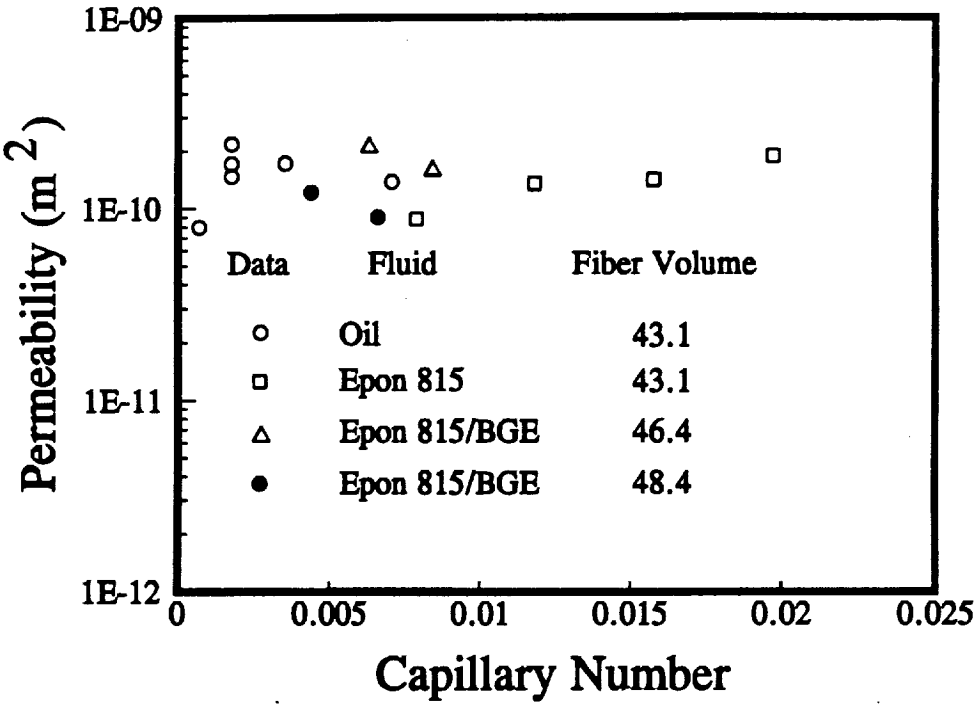

Figure 6.6: Advancing front permeability as a function of capillary number for constant flow rate injection tests.

7.0 SURFACE TENSION/CONTACT ANGLE MEASUREMENTS

Due to the nature of the RTM process, it is important to understand the interaction that occurs between the fiber and resin during injection. Therefore, surface tension and contact angle measurements were made to determine the extent of this interaction. As mentioned previously, a low contact angle implies that the resin wets out the fiber. Likewise, a low value of surface tension is desired as a low surface tension helps in the elimination of voids. Both contact angle and surface tension affect the amount of capillary pressure seen in the preform as the resin is injected. This chapter will discuss the experimental set up used in determining the above factors. Results for various fiber/resin systems will also be presented.

7.1 EXPERIMENTAL

The test chosen to measure the surface tension and contact angles for various systems was the single fiber pull out test. In this test, a single fiber is taken from a fiber tow and glued to the end of a copper wire hanger. This hanger is placed on a stirrup attached to a balance. The sample is then slowly lowered into a beaker full of the chosen fluid. The force exerted by the fluid on the fiber is measured by the balance. The contact angle can be calculated using the following expression

$$F_w = \frac{\sigma\, p \cos\theta}{0.981} \qquad (7.1.1)$$

where F_w is the wetting force in milligrams, σ is the surface tension in dyne/cm, p is the perimeter of the fiber in cm, and Θ is the contact angle between the fiber and resin. The value 0.981 is a conversion factor from milligrams to dynes.

As can be seen from the above equation, the fiber perimeter and surface tension of the test fluid need to be determined prior to any testing. The perimeter of the fiber is determined by immersing it in a fluid with a known surface tension. The fluid used in this case was hexane which has a contact angle of 0.0° with the fiber and a surface tension of 18.4 dyne/cm. From equation (7.1.1), the perimeter of the fiber is determined.

The surface tension of the test fluid is then determined by lowering a glass plate into the liquid. The glass plate has a contact angle of 0°. Then, by using the same equation, the surface tension of the fluid is determined.

Once the surface tension of the fluid and the fiber perimeter were known, tests were conducted to determine the contact angle between the various fibers and fluids used in this study. A Cahn Dynamic Contact Angle Analyzer, model DCA 322, was used to perform these tests. Single fiber samples from the 162 E-glass fabric and the TTI IM7/8HS fabric were tested to determine their contact angle with a dyed corn oil and Epon 815 resin.

For each test, several force values were taken during the lowering and raising of the sample into the liquid. Due to the highly viscous nature of the epoxy, the platform was stopped and the force was allowed to equilibrate prior to recording the value. An average contact angle was then determined from these values.

7.2 RESULTS

Shown in Figure 7.1 is a scanning electron micrograph of a single E-glass fiber. Likewise, a scanning electron micrograph of three IM7 carbon fibers is given in Figure 7.2. From these figures, it can be seen that the E-glass fiber is larger than the

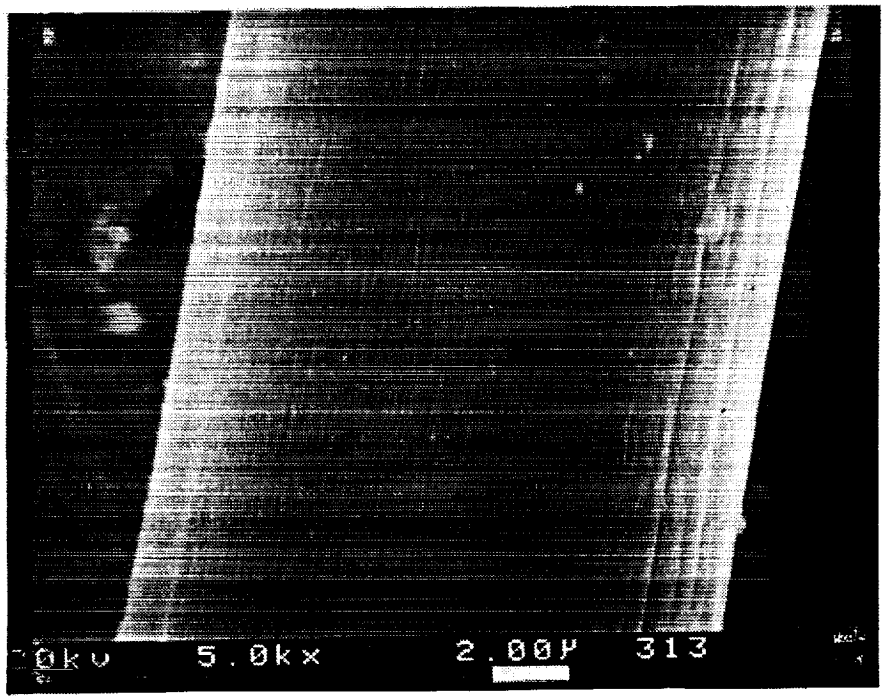

Figure 7.1: Scanning electron micrograph of a 162 E-glass fiber.

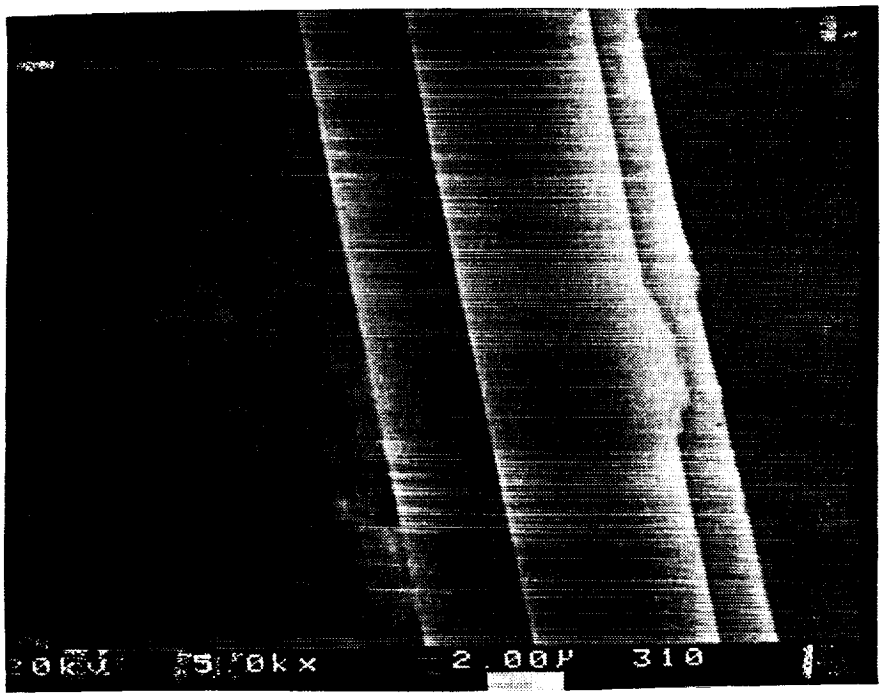

Figure 7.2: Scanning electron micrograph of three TTI IM7/8HS carbon fibers.

IM7 fiber. Also, the E-glass fiber has more surface ridges than the IM7 fiber. The smoother surface of the IM7 fiber could be the result of the sizing commonly used on these fibers.

The perimeter of the E-glass fiber was found to be 0.0231 mm and that of the TTI IM7/8HS fiber was 0.0193 mm. Using the technique described above, the surface tension for the dyed corn oil and Epon 815 resin was found to be 0.02654 and 0.03722 N/m, respectively.

Tests were then performed on single fibers to determine their contact angles. The results of these tests are presented in the Table 7.1. The results indicate that the EPON 815 wets out both the 162 E-glass and the TTI IM7/8HS fiber better than the corn oil. Also from Table 7.1, it can be seen that the 162 E-glass has a lower contact angle for both fluids than the IM7 fiber. Again, this could be the result of the sizing on the IM7 fiber.

Recalling equation (2.4.2), the capillary pressure, P_c, can be expressed as

$$P_c = \frac{\sigma \cos \theta}{m} \qquad (7.2.1)$$

where σ is the surface tension, θ is the contact angle, and m is the hydraulic radius.

The hydraulic radius, m, is defined as

$$m = \frac{d_f}{4} \frac{(1 - v_f)}{v_f} \qquad (7.2.2)$$

Table 7.1: Contact angle values for various fiber/resin systems.

	162 E-glass	TTI
Corn Oil	25.8	36.1
Epon 815	17.0	28.5

where d_f is the fiber diameter and ν_f is the fiber volume fraction.

For a TTI IM7/8HS preform with Epon 815 resin, the capillary pressure during injection is equal to approximately 24.5 kPa. A fiber diameter of 8.0E-6 meters and a fiber volume fraction of 60% was used in this calculation.

8.0 RESIN CHARACTERIZATION

This section will discuss the methods used to characterize the resin system used in the production of flat panels by the RTM method. Differential scanning calorimetry (DSC) experiments were conducted to establish the kinetic behavior of the resin. Cone and plate viscometer data provided by Shell Development Company was used for creating a rheological model. The results of these tests will be presented.

8.1 SHELL 1895/W RESIN SYSTEM

Shell 1895 resin is a high performance aerospace resin system designed for use in resin transfer molding and filament winding processes [56]. Shell 1895, an epoxy based system, was chosen for this investigation due to its ease of use and relatively low injection temperature (80 °C). The system consists of two parts, the epoxy base resin (1895) and the curing agent (W). Shell 1895/W has a viscosity of 300-350 poise at the injection temperature of 80 °C with a pot life of approximately 48 hours. Shell 1895/W also has a high stiffness and good moisture resistance, both of which are important properties for aerospace composites.

Shell 1895 is a combination of difunctional and multifunctional epoxy resins while Curing Agent W is a non-MDA, aromatic amine curing agent. The mixing ratio is 3:1, epoxy to curing agent.

8.2 DSC EXPERIMENTS

As mentioned earlier, DSC experiments were performed on the Shell 1895/W system to determine the kinetic behavior of the system. All tests were conducted on a DuPont 9900 DSC system. Sample sizes ranged from 5.0 to 7.0 mg and were

encapsulated in hermetically sealed pans. All samples were prepared under the same conditions and from the same batch of resin.

8.2.1 Experimental

Prior to the start of testing, the DSC chamber was heated to 500 °C to remove any possible sources of contamination. Then, the system was calibrated through the use of indium and lead samples. Isothermal runs were conducted at 100, 121, 135, 149, 160, and 177 °C until the reaction was judged complete. After the isothermal runs were completed, a dynamic scan from 50-300 °C at 5 °C/min was conducted to measure the residual heat of reaction remaining in the sample. Dynamic scans from 50-300 °C at rates of 1, 2.5, and 5 °C/min were also performed to compare with model predictions.

After all tests had been completed, the following model [57] was used to fit the data

$$\frac{d\alpha}{dt} = \frac{H_T}{H_U}\frac{d\beta}{dt} \qquad (8.2.1)$$

where H_U is the total heat of reaction determined from the sum of the isothermal and dynamic scans, H_T is the isothermal heat of reaction, and $d\beta/dt$ is the isothermal rate of cure. For this study, $d\beta/dt$ was assumed to have the following form

$$\frac{d\beta}{dt} = (K_1 + K_2\,\beta^m)\,(1-\beta)^n \qquad (8.2.2)$$

where m and n are constants with a slight dependence on temperature. The isothermal degree of cure, β, is related to the total degree of cure, α, by the expression

$$\alpha = \frac{H_T}{H_U}\,\beta \tag{8.2.3}$$

where α and β have the following definitions

$$\begin{aligned} \alpha &= \frac{H(t)}{H_U} \\ \beta &= \frac{H(t)}{H_T} \end{aligned} \tag{8.2.4}$$

where H(t) is the heat evolved per unit mass of resin.

K_1 and K_2 are rate constants which have an Arrhenius temperature dependence

$$\begin{aligned} K_1 &= A_1 \exp\left(-\frac{E_1}{RT}\right) \\ K_2 &= A_2 \exp\left(-\frac{E_2}{RT}\right) \end{aligned} \tag{8.2.5}$$

where A_1 and A_2 are pre-exponential factors, E_1 and E_2 are activation energies, R is the universal gas constant, and T is the temperature in degree Kelvin.

8.2.2 Results

Experimental data generated from the isothermal runs are presented in tabular form in Appendix A. From this data, values of H_T/H_U for each isothermal run were determined. A plot of H_T/H_U versus temperature for the six isothermal runs is shown in Figure 8.1. This ratio is used to relate the isothermal rate of cure, $d\beta/dt$, to the total cure rate, $d\alpha/dt$. A linear fit to this data yielded the following relationship

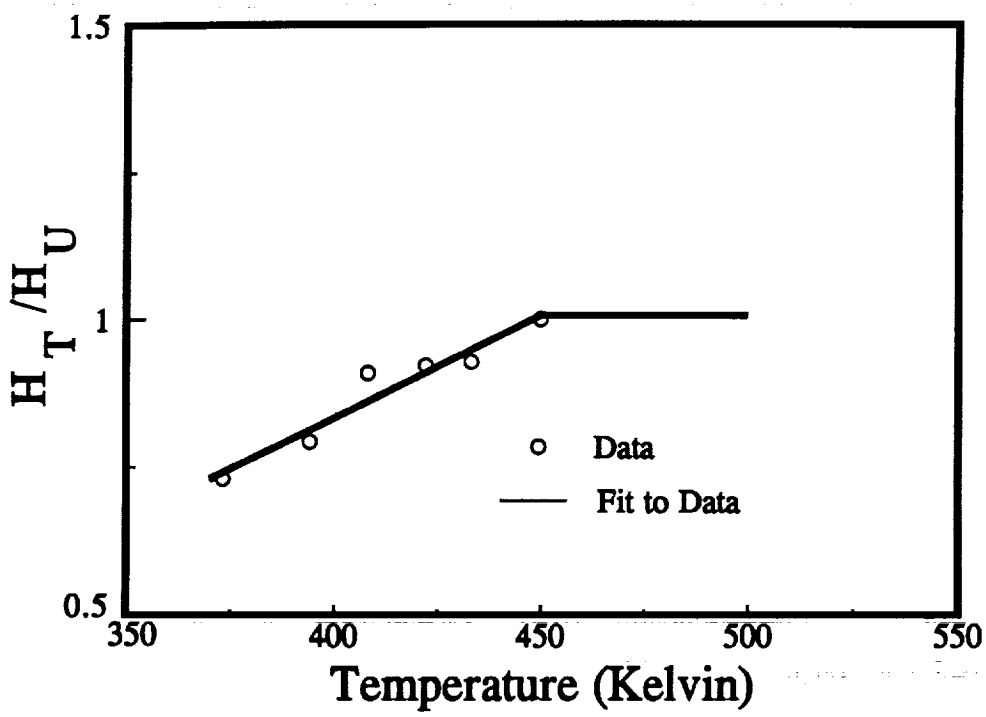

Figure 8.1: H_T/H_U as a function of temperature for the Shell 1895/W system.

$$\frac{H_T}{H_U} = 0.0033874(T) - 0.521654 \qquad T < 450\ ^\circ K$$
$$\frac{H_T}{H_U} = 1 \qquad T \geq 450\ ^\circ K \tag{8.2.6}$$

A non-linear curve fitting program utilizing the Marquardt-Levenberg algorithm was written to determine the values of m, n, A_1, A_2, E_1, and E_2 for each of the six isothermal runs. The program reads the values of β and $d\beta/dt$ from an input file and iteratively solves equation (8.2.2) until the solution with the desired degree of accuracy is obtained. The program then outputs the values for m, n, K_1, and K_2.

Values of m and n were plotted against inverse temperature. The data were fit with a linear least squares fit which resulted in the following equations

$$m = 1.4597 - 247.12\left(\frac{1}{T}\right)$$
$$n = 4.2432 - 1313.79\left(\frac{1}{T}\right) \tag{8.2.7}$$

where T is in degree Kelvin. A plot detailing this relationship is given in Figure 8.2.

The values of A_1, A_2, E_1, and E_2 were found by constructing Arrhenius plots of the natural log of the rate constants (K_1 and K_2) versus inverse temperature and fitting a linear least squares curve to the data. This plot is shown in Figure 8.3. The y-intercept is equal to the natural log of the pre-exponential constants (A_1 and A_2). The slope is equal to the value (-E/R). The resulting values are presented in Table 8.1.

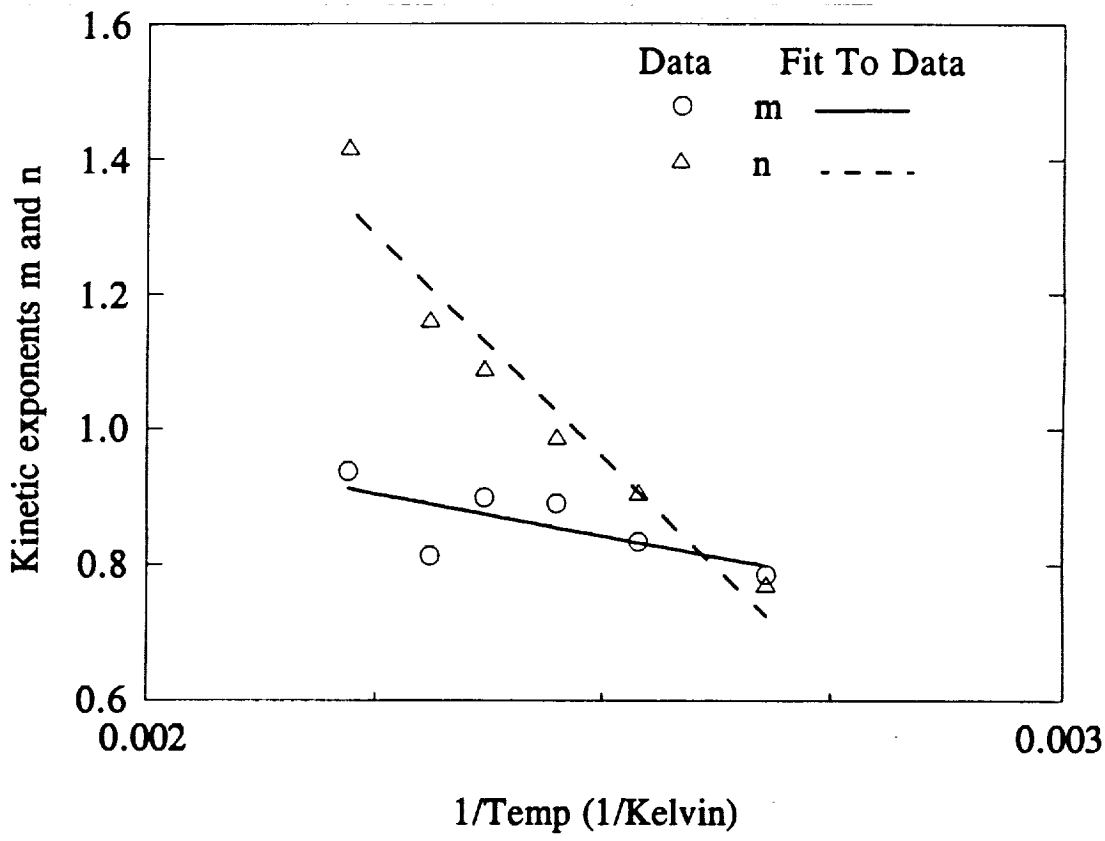

Figure 8.2: Kinetic exponents m and n as a function of inverse temperature.

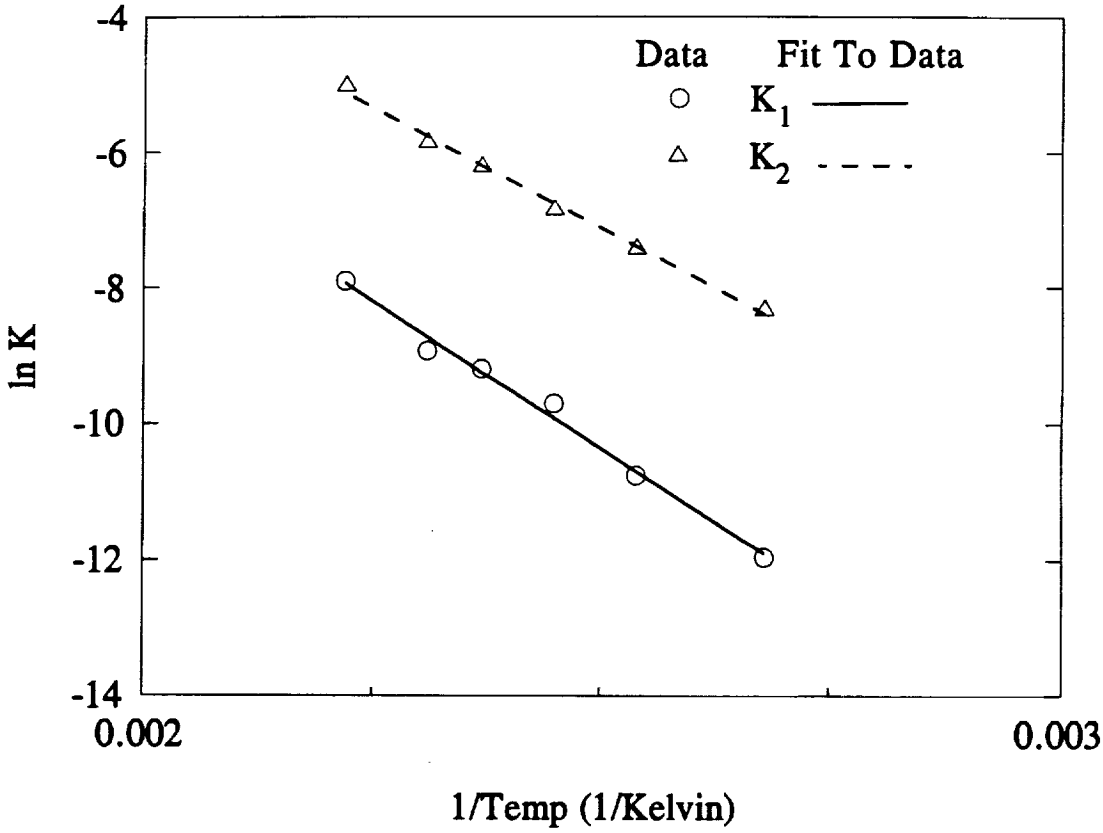

Figure 8.3: Arrhenius plots of the rate constants as a function of inverse temperature.

Table 8.1: Experimentally determined values for the pre-exponential constants and activation energies for the Shell 1895/W system.

	A_i (1/s)	E_i (J/mole)
i=1	76,496	71,840
i=2	39,140	58,833

Therefore, the rate constants K_1 and K_2 have the form

$$K_1 = 76{,}496 \exp\left(\frac{-71{,}840}{RT}\right)$$
$$K_2 = 39{,}140 \exp\left(\frac{-58{,}833}{RT}\right) \qquad (8.2.8)$$

where T is in degree Kelvin. A value of 8.31441 J/(mole °K) was used for the universal gas constant, R.

The isothermal reaction rates, $d\beta/dt$, as a function of the isothermal degrees of cure, β, are presented in Figures 8.4-8.6. The model-predicted values agreed well with experimental data. The model slightly under-predicts the reaction rate at 100 °C and 177 °C; but accurately predicts the reaction rate for the other four temperatures.

Comparisons between experimental and model-predicted isothermal (β) and total (α) degrees of cure are presented in Figures 8.7-8.12. The model-predicted values agreed well with experimental data. From these figures, it can be seen that the Shell 1895/W system cures out fully only at 177 °C. At the lower temperatures, the final degree of cure ranges from 0.7-0.9.

In Figures 8.13 and 8.14, the degree of cure (α) as a function of temperature for the dynamic scans are presented. Again, there is good agreement between the experimental and model-predicted values. Slight deviations are evident at the initial upturn in the degree of cure for the 1 °C/min and 2.5 °C/min scans. However, this difference is small and only exits over a narrow range. For the 5 °C/min scan, the model slightly over predicts the degree of cure for the range of 0.4-0.8. However, the trend for the experimental and model-predicted behavior are identical.

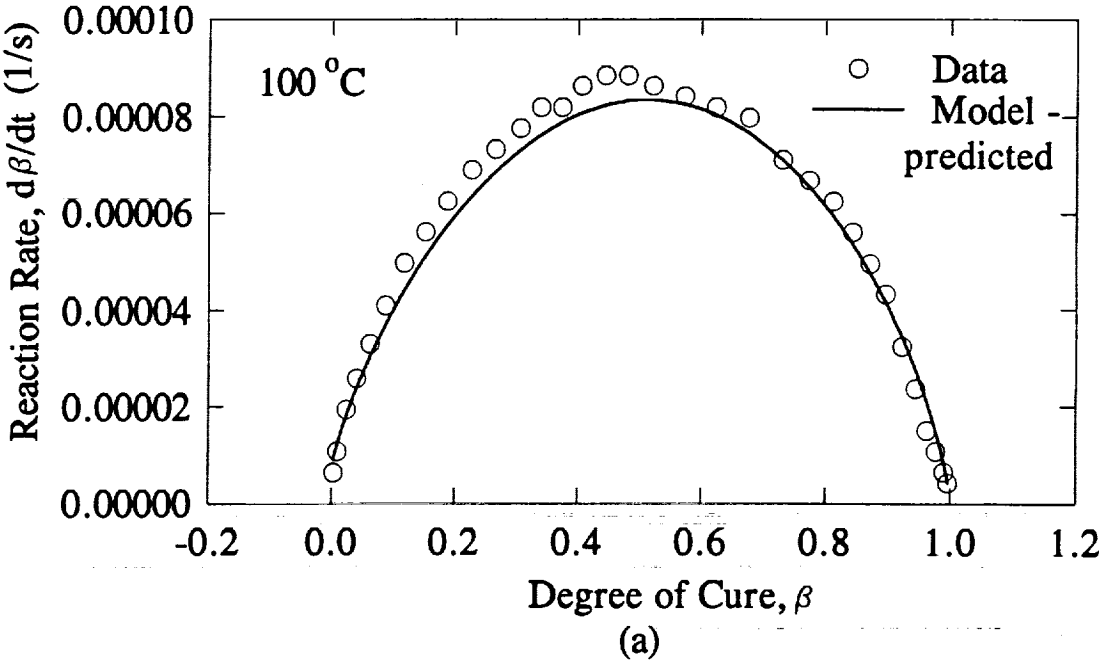

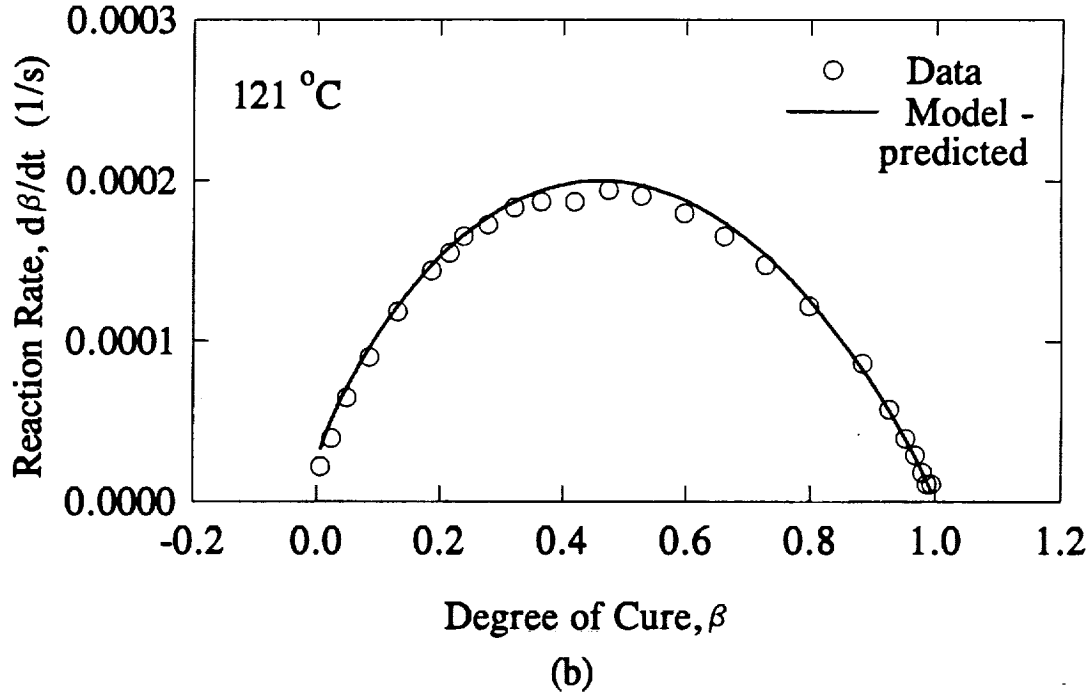

Figure 8.4: Comparison between experimental and model values for dβ/dt as a function of β for (a) 100 °C and (b) 121 °C.

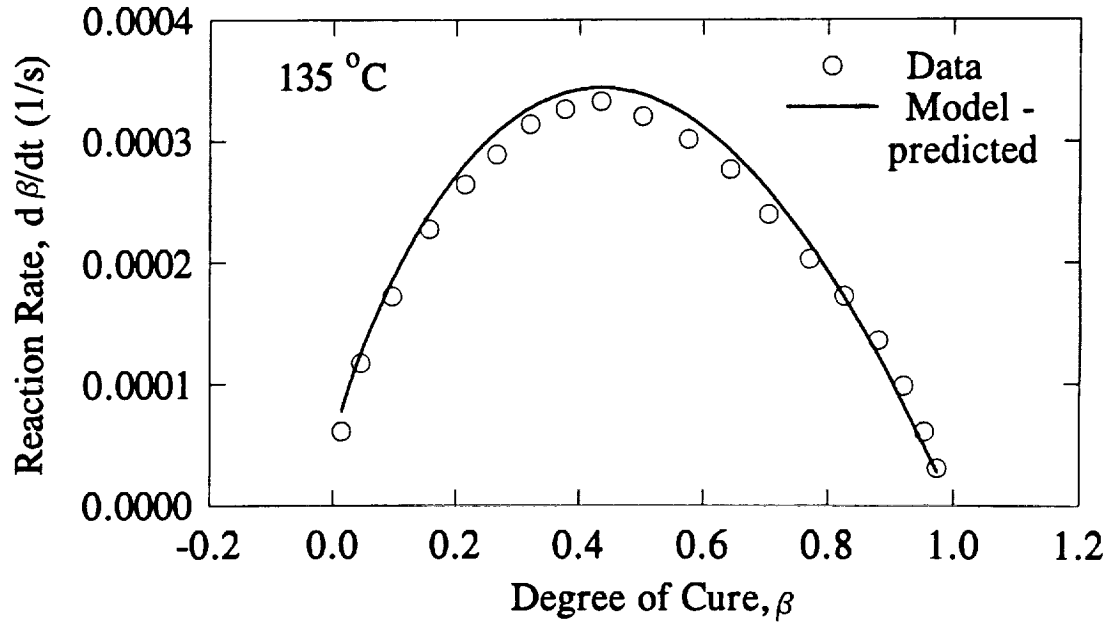

(a)

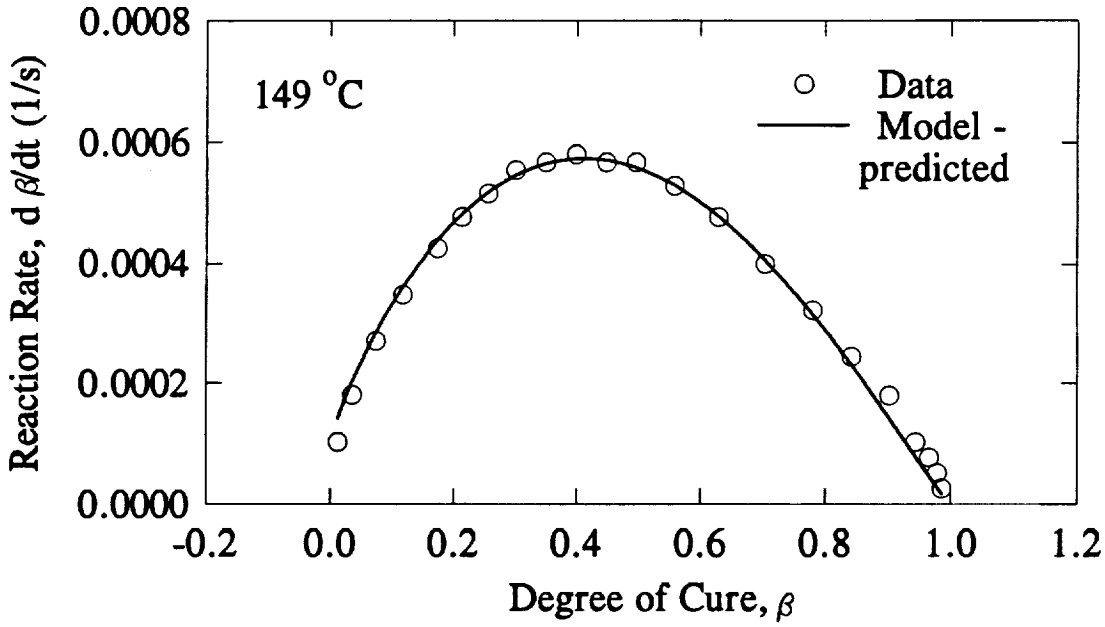

(b)

Figure 8.5: Comparison between experimental and model values for $d\beta/dt$ as a function of β for (a) 135 °C and (b) 149 °C.

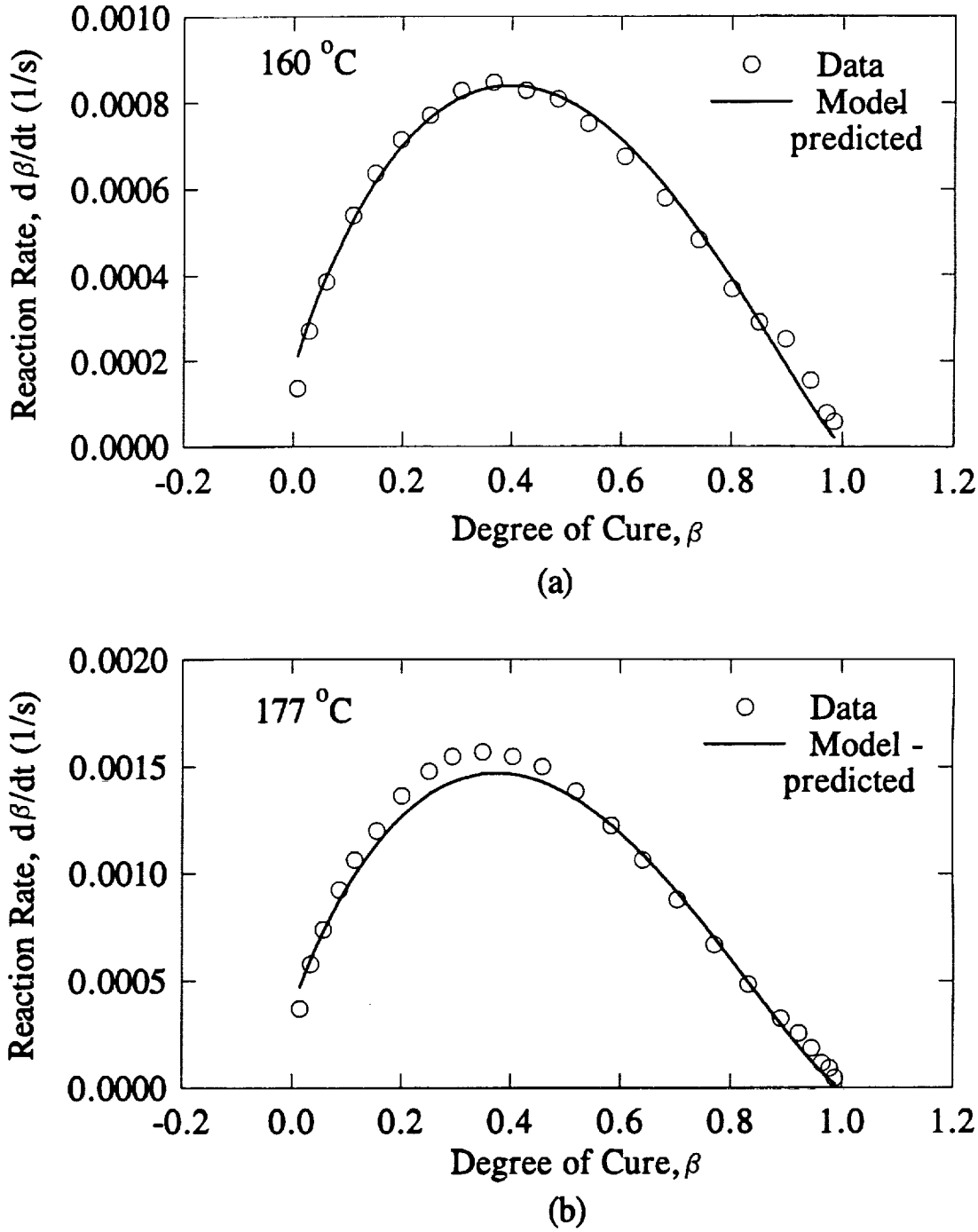

Figure 8.6: Comparison between experimental and model values for $d\beta/dt$ as a function of β at (a) 160 °C and (b) 177 °C.

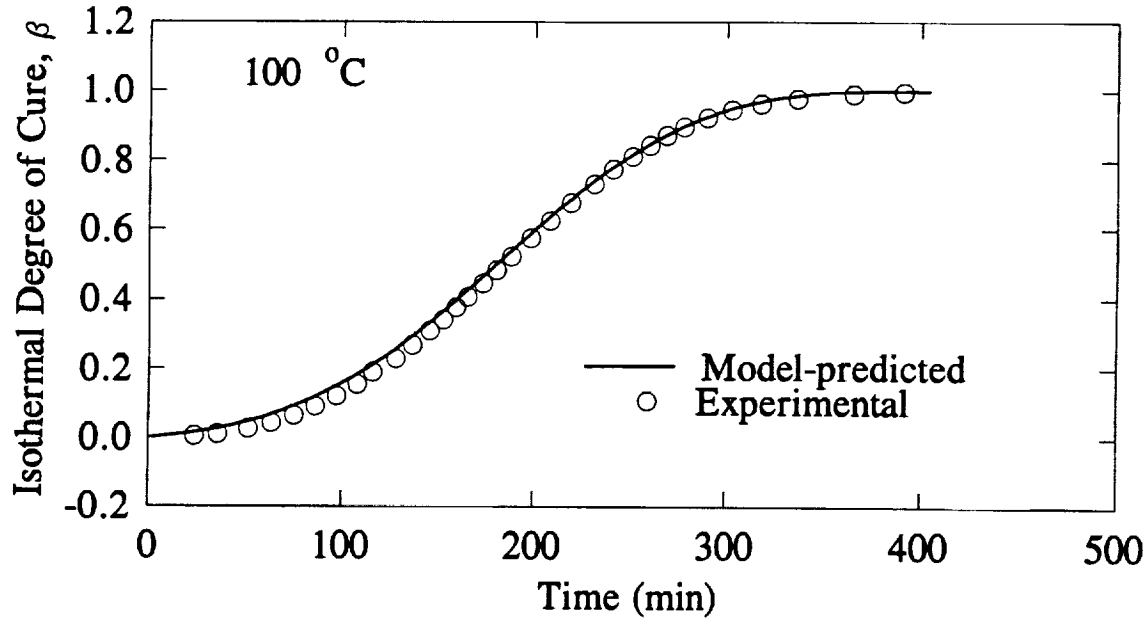

(a)

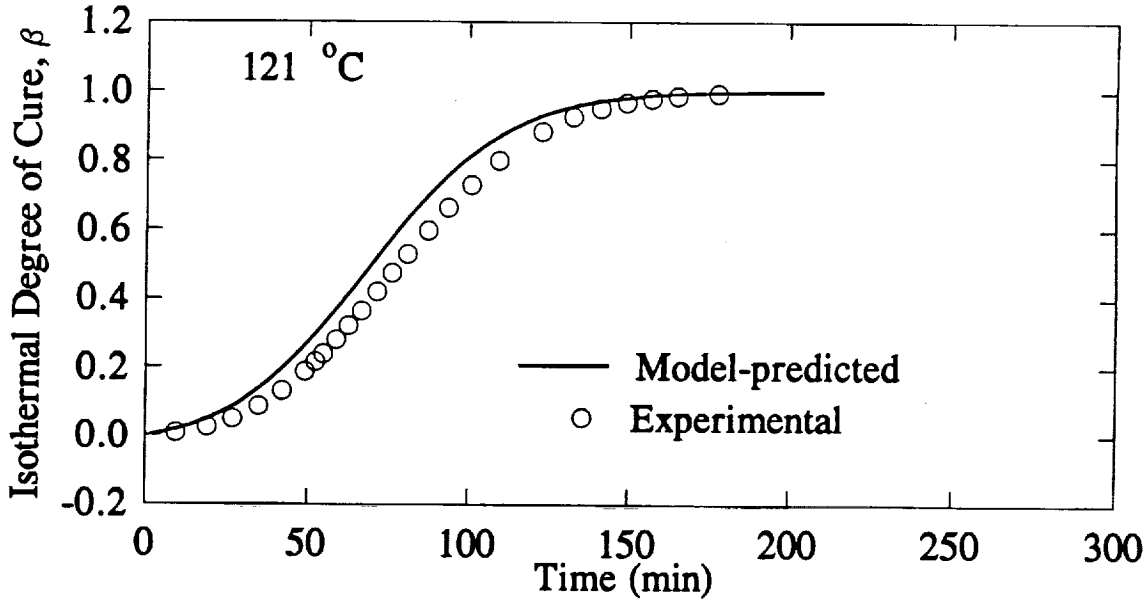

(b)

Figure 8.7: Comparison between experimental and model values for β as a function of time at (a) 100 °C and (b) 121 °C.

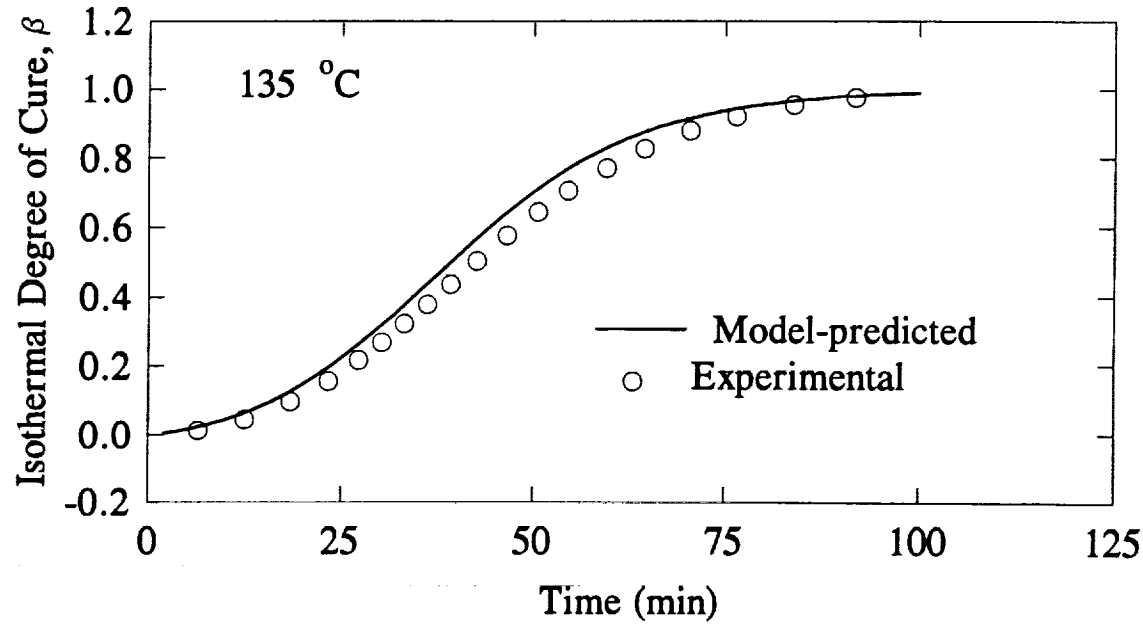

(a)

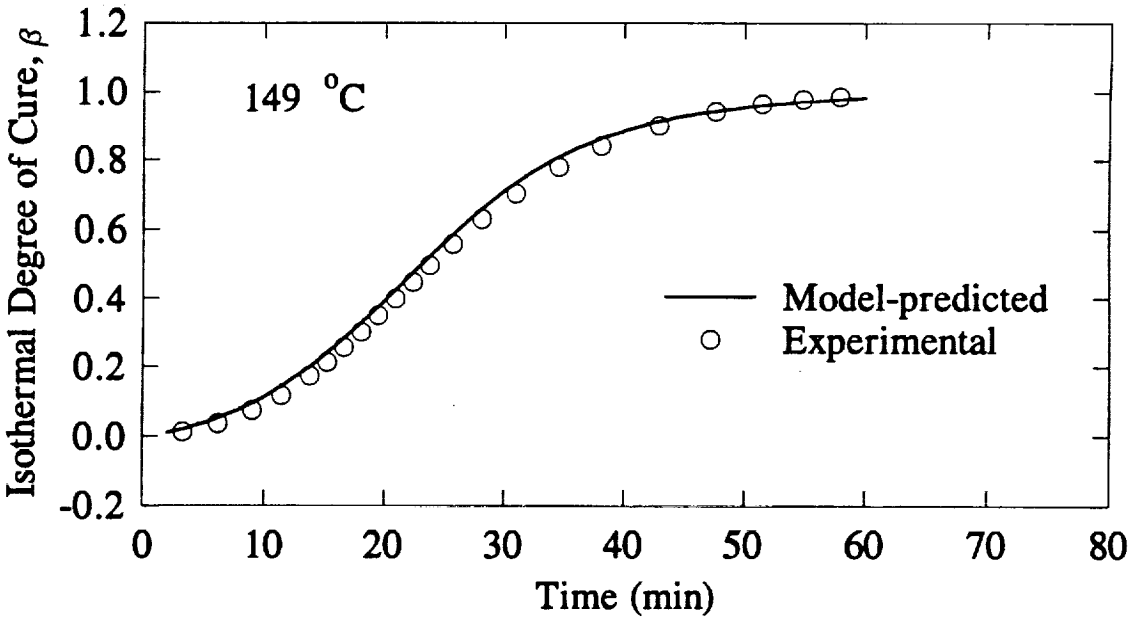

(b)

Figure 8.8: Comparison between experimental and model values for β as a function of time at (a) 135 °C and (b) 149 °C.

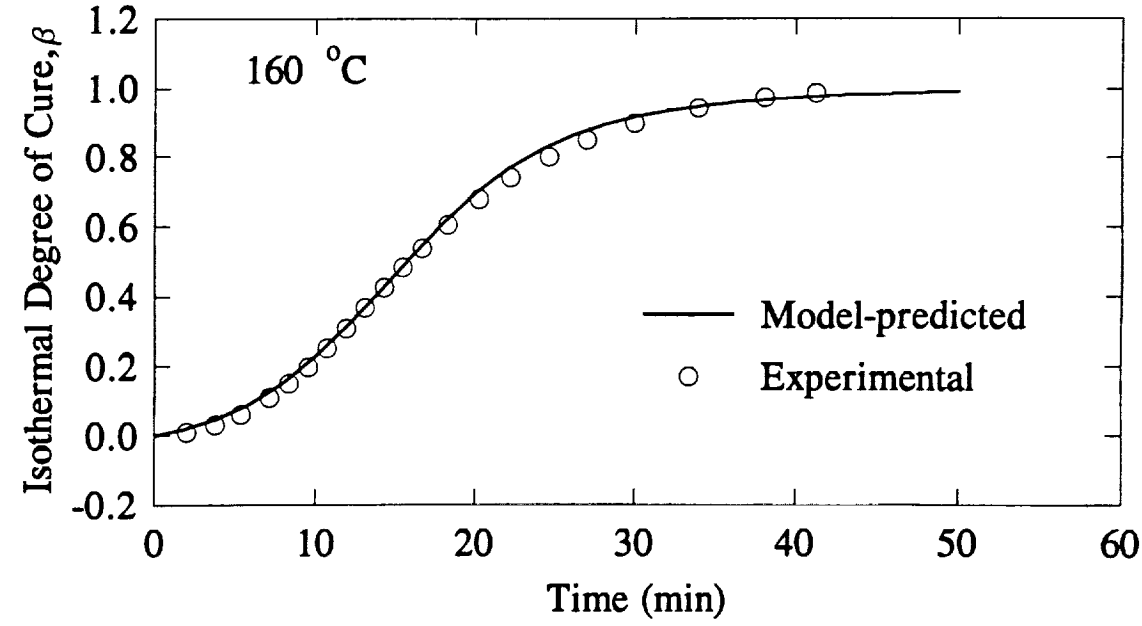

(a)

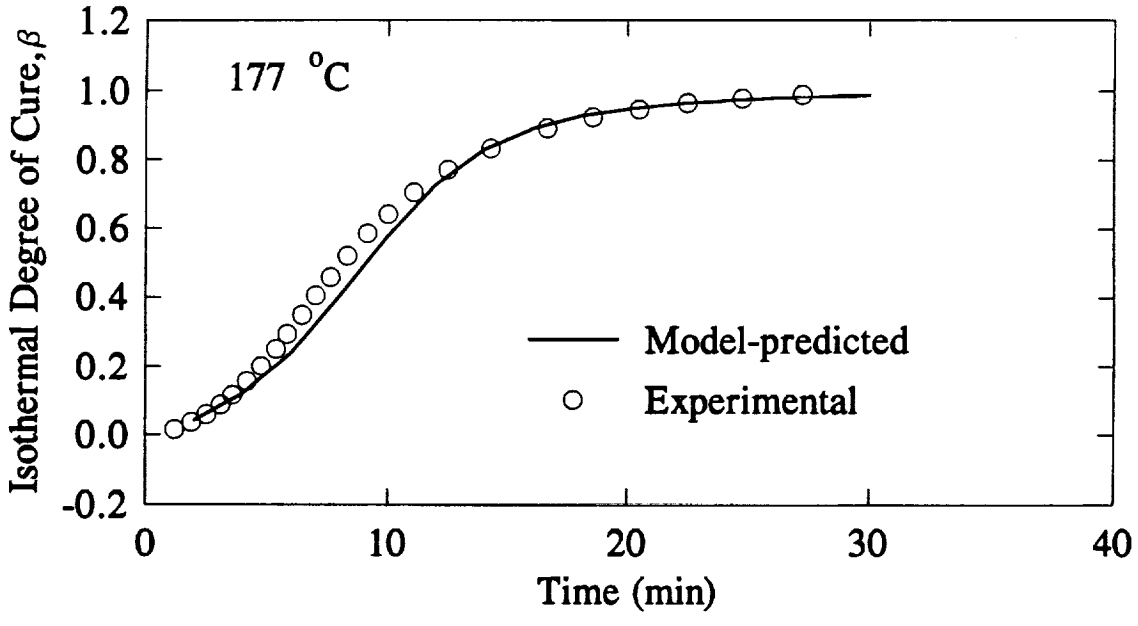

(b)

Figure 8.9: Comparison between experimental and model values for β as a function of time at (a) 160 °C and (b) 177 °C.

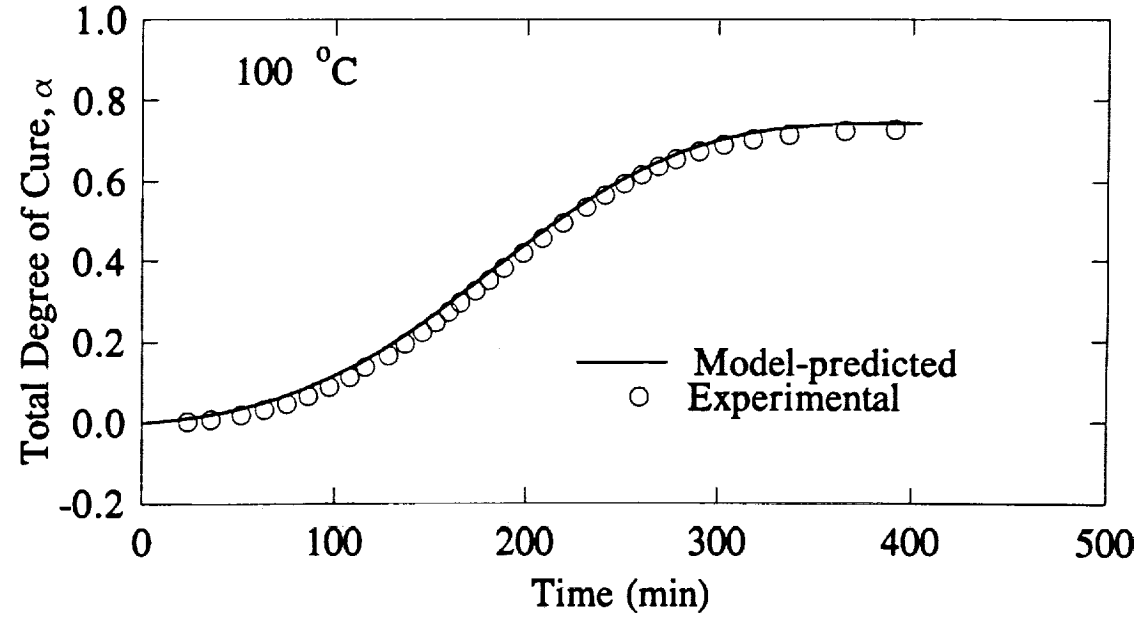

(a)

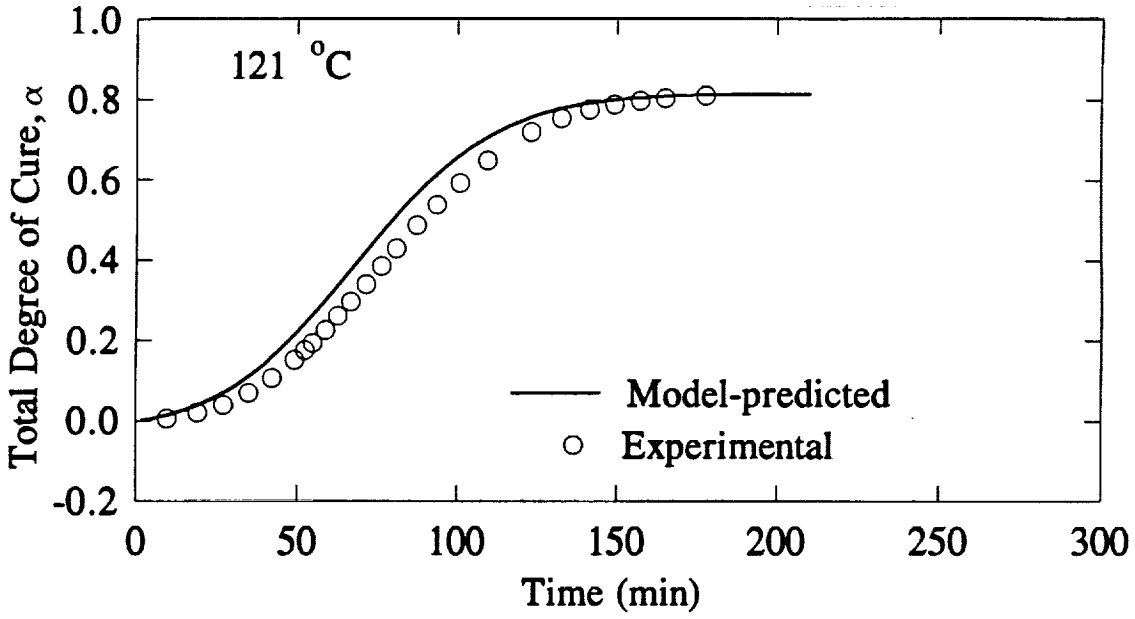

(b)

Figure 8.10: Comparison between experimental and model values for α as a function of time at (a) 100 °C and (b) 121 °C.

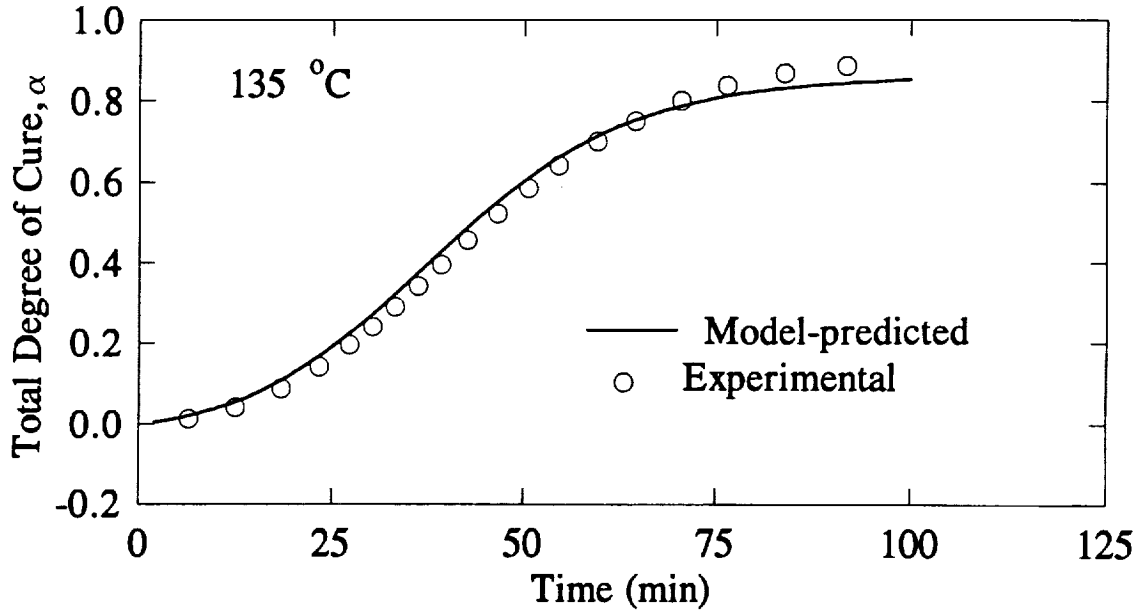

(a)

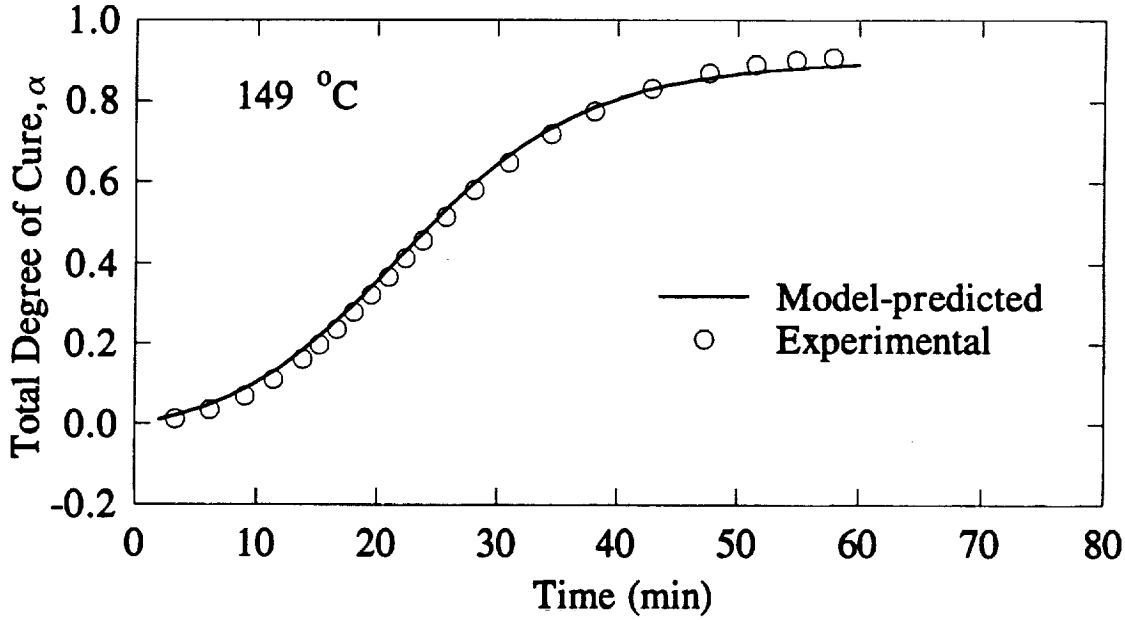

(b)

Figure 8.11: Comparison between experimental and model values for α as a function of time at (a) 135 °C and (b) 149 °C.

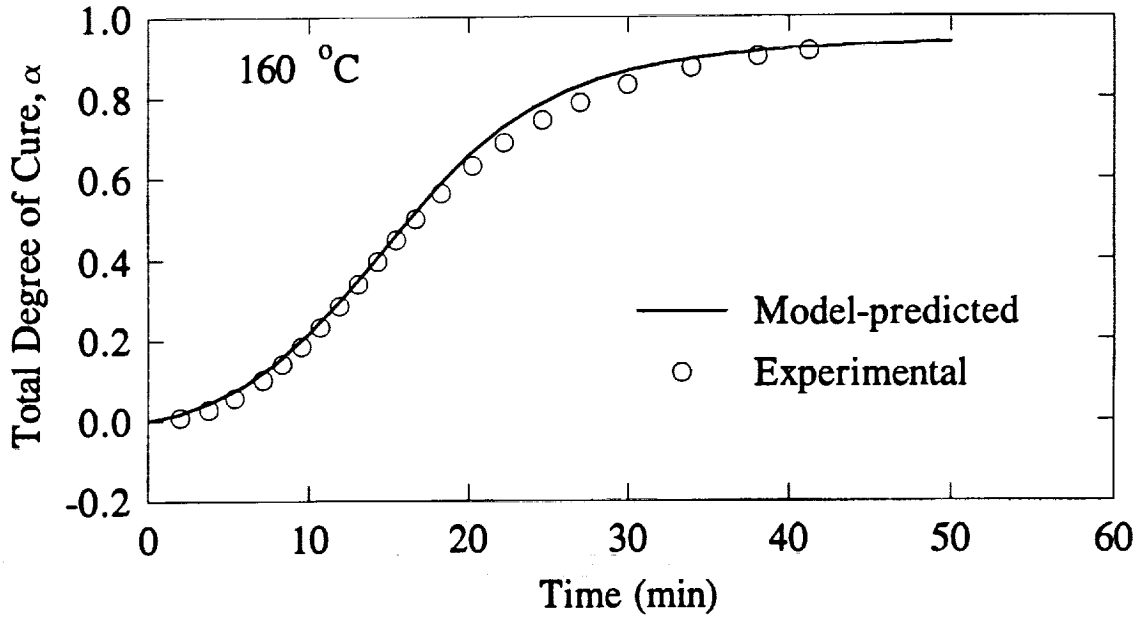

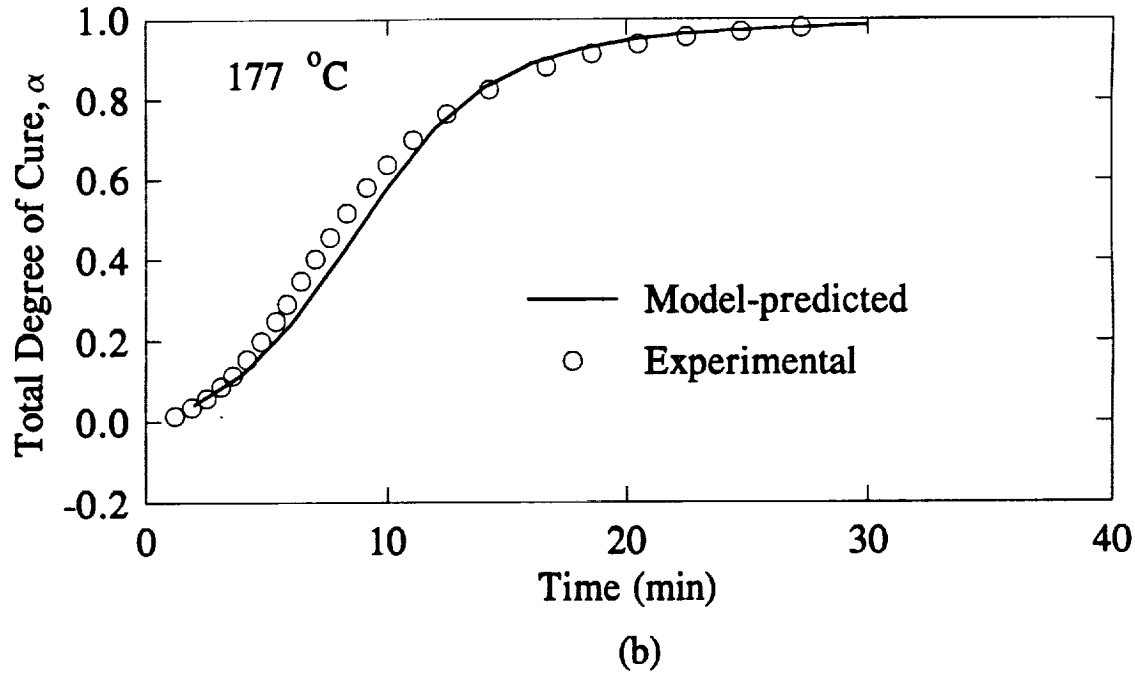

Figure 8.12: Comparison between experimental and model values for α as a function of time at (a) 160 °C and (b) 177 °C.

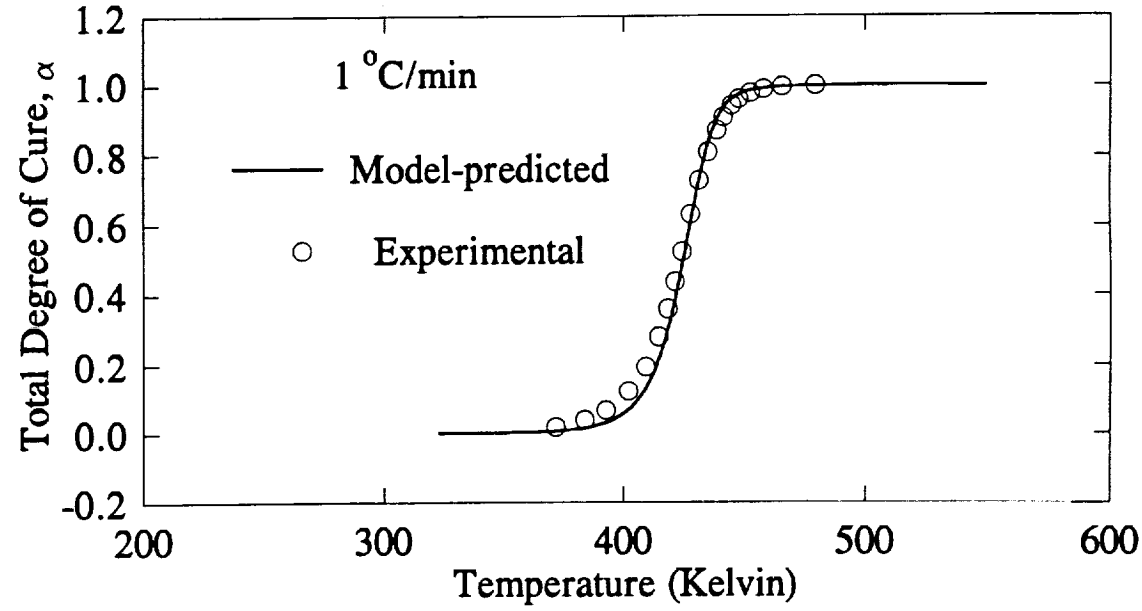

(a)

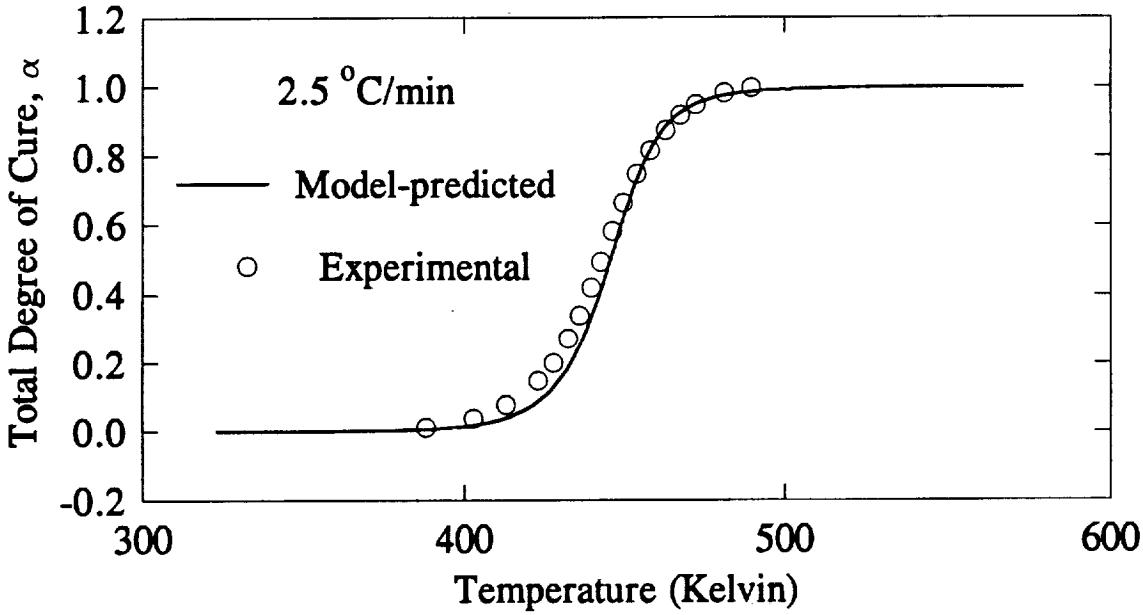

(b)

Figure 8.13: Comparison between experimental and model values for α as a function of temperature for dynamic scans at (a) 1 °C/min and (b) 2.5 °C/min.

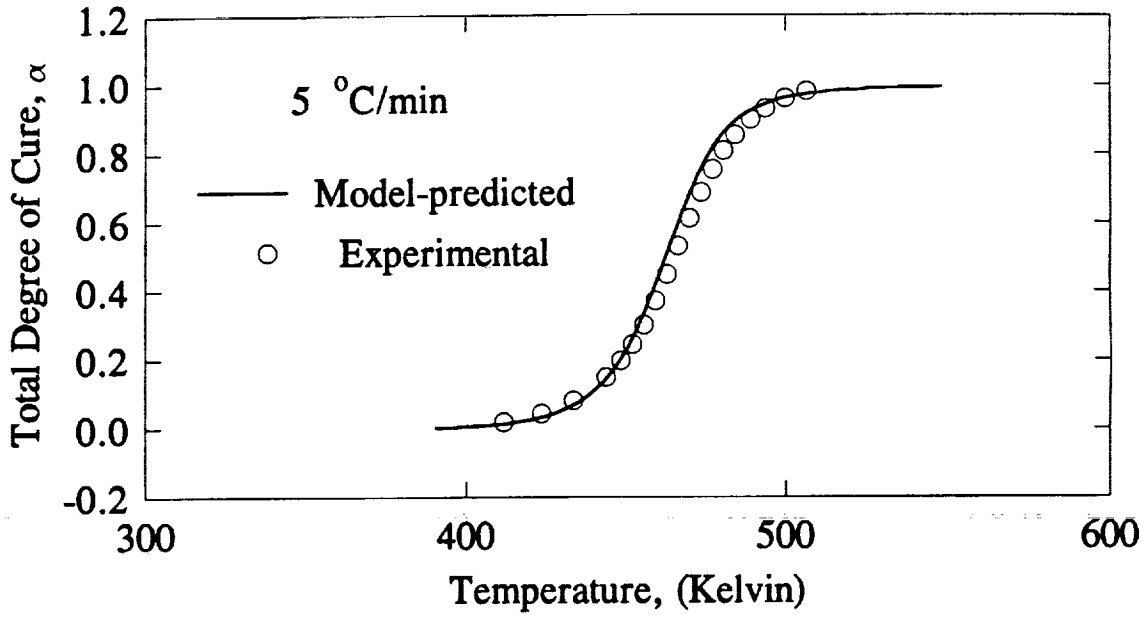

Figure 8.14: Comparison between experimental and model values for α as a function of temperature for dynamic scan at 5 °C/min.

8.3 VISCOSITY EXPERIMENTS

Just as it is critical to have an accurate kinetics model to predict the cure behavior of the resin after infiltration, it is equally important to have a viscosity model to predict the viscosity behavior during infiltration. An accurate viscosity model can be used to ensure that the part is completely infiltrated prior to the resin becoming too viscous to flow. This section will discuss the approach taken to model the Shell 1895/W system and present the results from this model.

8.3.1 Experimental

The viscosity data used in this work was provided by Shell Development Company. A Rheometrics RECAP II viscometer was used to measure the viscosity of the Shell 1895/W system. Isothermal runs were conducted at 60, 80, 100, 121, 149, and 177 °C. Dynamic heating runs were conducted with heating rates of 2 and 5 °C/min. The plate radius was 12.5 mm with a gap height of 1.0 mm. The rotational speed was set at 10 rad/s for all tests. The strain rate for the isothermal tests was 40%. For the dynamic runs, a maximum limit of 10% strain was imposed. There was a 1% initial strain present in the samples for the dynamic runs.

The following model [58] was used in fitting the data

$$\eta = \eta_0 \left[\frac{\alpha_g}{\alpha_g - \alpha} \right]^{f(\alpha,T)} \tag{8.3.1}$$

where α is the degree of cure, α_g is the degree of cure at the gel point, and η_0 is the initial viscosity. It has been shown [59] that the exponent f(α,T) is a function of the degree of cure of the resin and temperature.

The initial viscosity, η_0, is defined to be

$$\eta_0 = A_\eta \exp\left(\frac{E_\eta}{RT}\right) \tag{8.3.2}$$

where A_η is the pre-exponential constant, E_η is the activation energy, R is the universal gas constant, and T is temperature in degree Kelvin.

8.3.2 Results

An initial attempt has been made in creating a viscosity model for the Shell 1895/W system based on equation (8.3.1). For this model, the exponent $f(\alpha,T)$ was taken to be a linear function of temperature with the form A + BT. The value of α_g, or the degree of cure at gel, was determined from the two dynamic scans as the degree of cure value at which a sharp increase in viscosity occurred. These curves are given in Figure 8.15. From this figure, α_g was found to be 0.95. Although this value is very high, it did provide a good fit to the experimental data.

The values of A, B, and η_0 were determined by plotting the natural log of the viscosity as a function of the natural log of α'. α' is defined as

$$\alpha' = \frac{\alpha_g}{\alpha_g - \alpha} \tag{8.3.3}$$

where α_g is set to 0.95 and α is the degree of cure. The y-intercept of the log η versus log α' plot is equal to the natural log of the initial viscosity, η_0, while the slope is equal to the exponent $f(\alpha,T)$.

Then, by plotting the natural log of η_0 as a function of inverse temperature, the

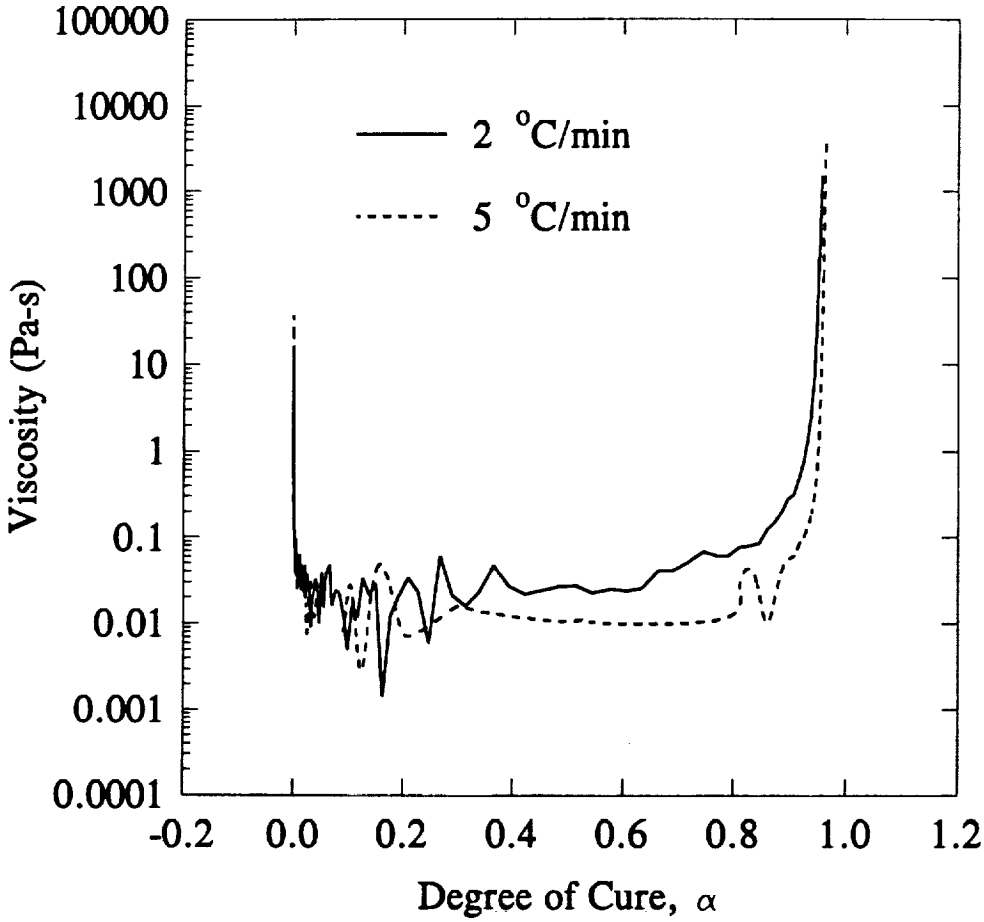

Figure 8.15: Viscosity as a function of the degree of cure for dynamic scans of 2 and 5 °C/min.

values for A_η and E_η were found. This plot is presented in Figure 8.16. Likewise, by plotting the exponent $f(\alpha,T)$ as a function of temperature, the values of A and B were found. This plot is shown in Figure 8.17. Values of these constants are presented in Table 8.2.

Comparisons between model-predicted and experimental viscosity are presented in Figures 8.18 and 8.19. It was found that the model was inaccurate at 60 °C and 80 °C. This is attributed to the slow reaction rate at these temperatures and the high value of α_g. Because the resin system does not gel at these low temperatures, the model is not well suited for use at these temperatures.

However, for temperatures equal to or greater than 100 °C, the model provides a fairly good representation of the viscosity behavior. Graphs comparing the model-predicted and experimental values for 100 °C and 121 °C are presented in Figure 8.18. Agreement for the 100 °C is excellent throughout the entire range of cure. For the 121 °C isotherm, however, the model over predicts the viscosity rise for the degree of cure greater than 0.3.

Comparisons for the 149 °C and 177 °C isotherms are given in Figure 8.19. Agreement between the model-predicted and experimental viscosities in the 149 °C case is very good until the resin degree of cure reaches 0.7. After this value, the model does not predict the sharp upturn in viscosity. Although the experimental data for the 177 °C isotherm is initially scattered, the model provides a fairly accurate prediction of the viscosity behavior until a degree of cure of 0.4 is reached. After this value, the model fails to capture the sharp upswing in viscosity.

The model was found to be acceptable for predicting the viscosity of the Shell 1895/W, at least for the infiltration aspect of the RTM process. Refinement of the

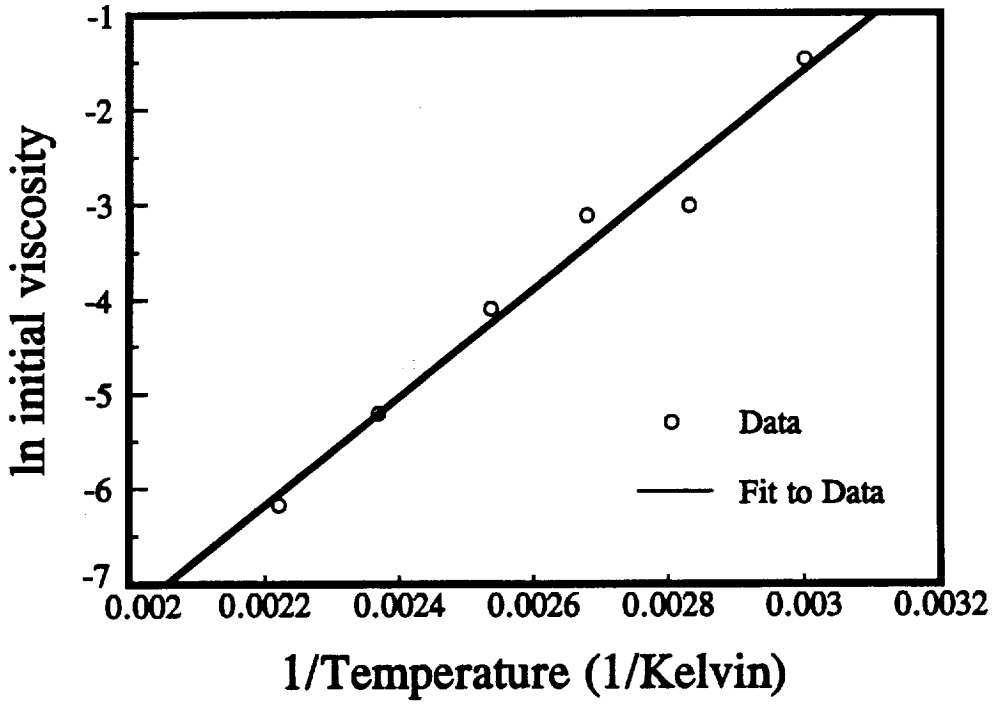

Figure 8.16: Arrhenius plot of the initial viscosity as a function of inverse temperature.

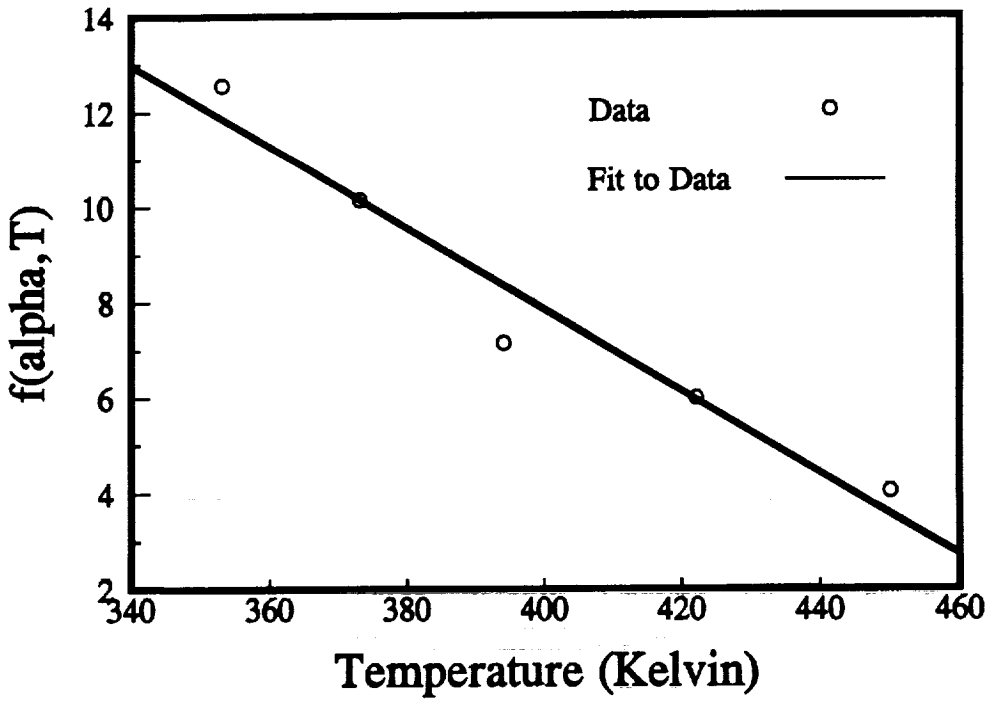

Figure 8.17: Plot of f(α,T) as a function of temperature.

Table 8.2: Experimentally determined values used in the viscosity model.

α_g	0.95
A_η (Pa•s)	7.201E-9
E_η (J/mole °K)	47,506
A	42.0644
B	-0.08554

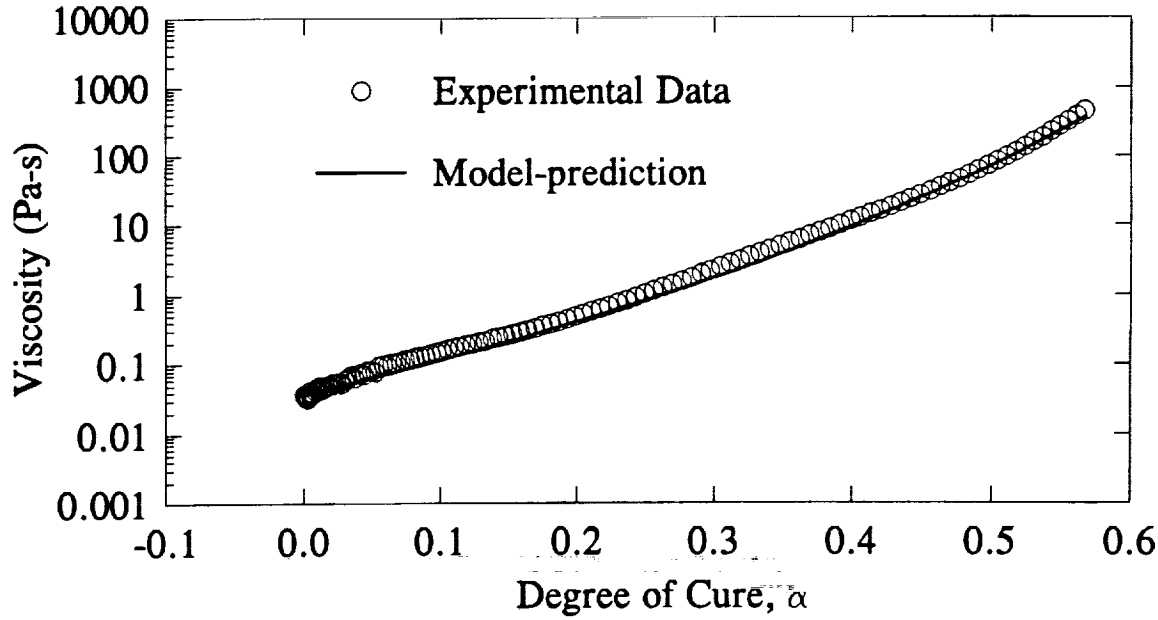

(a)

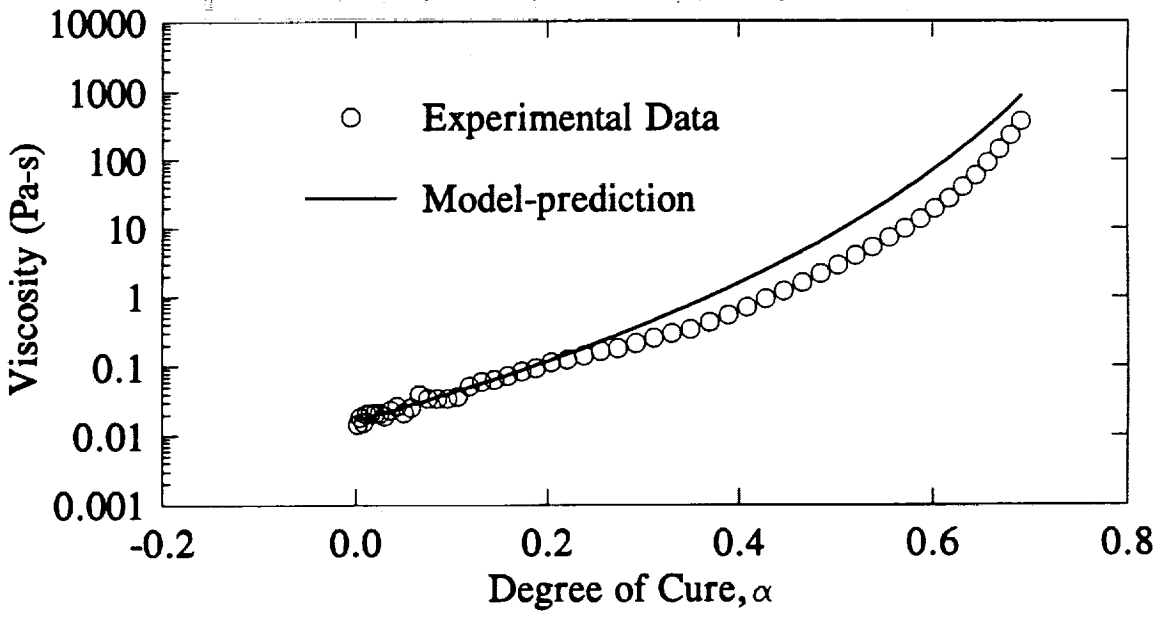

(b)

Figure 8.18: Comparison between model-predicted and experimental viscosity at (a) 100 °C and (b) 121 °C.

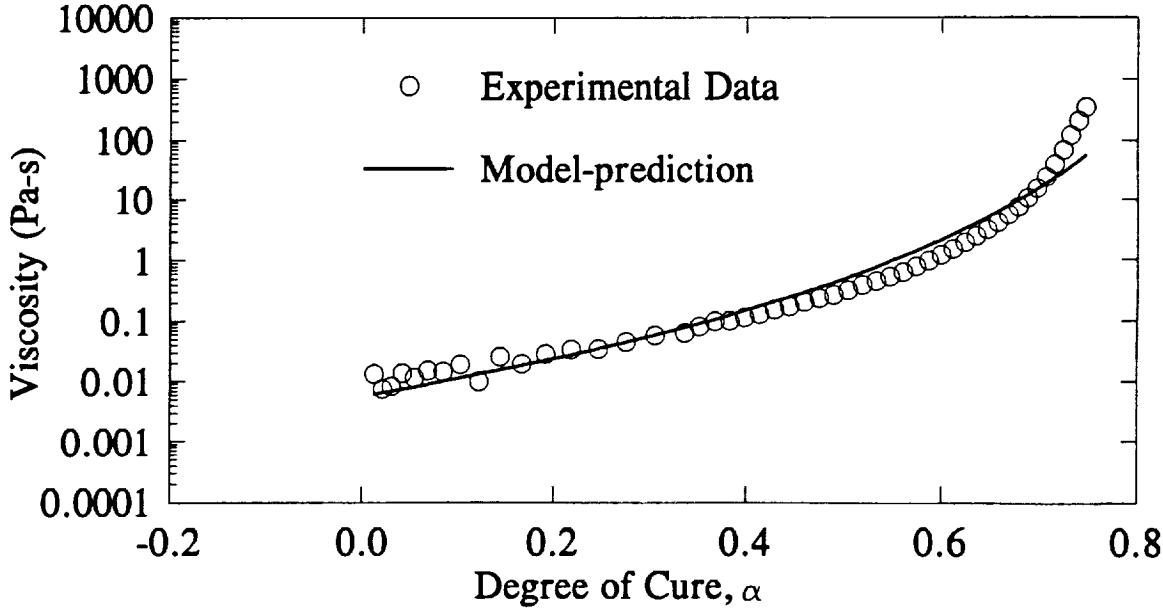

(a)

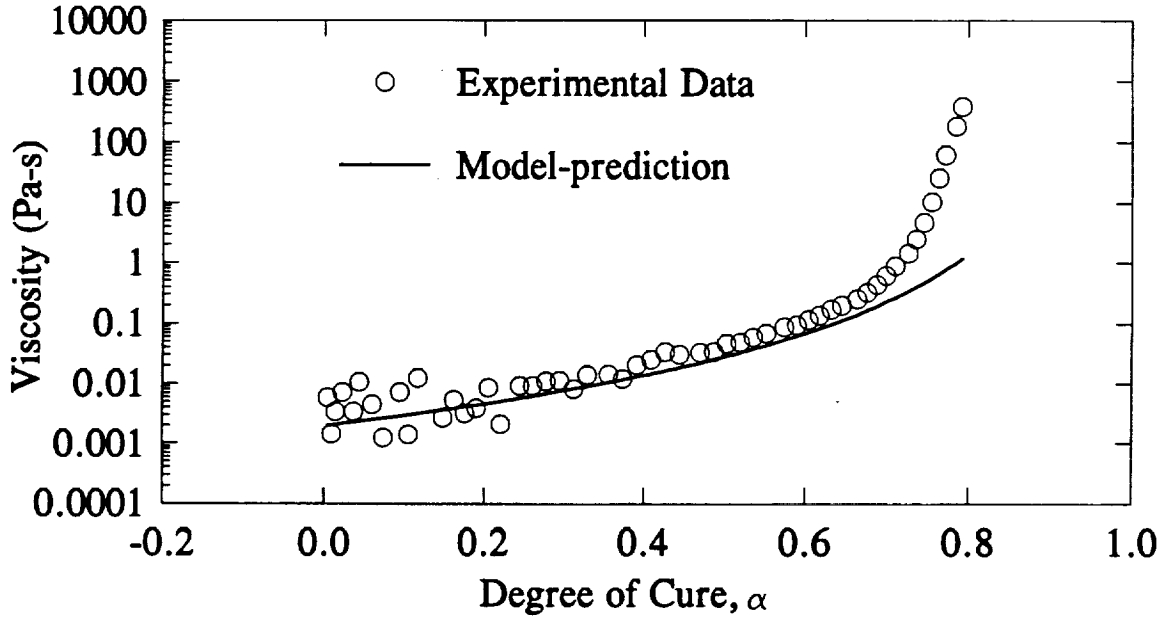

(b)

Figure 8.19: Comparison between model-predicted and experimental viscosity at (a) 149 °C and (b) 177 °C.

model is necessary to capture the resin gelation that occurs during the curing of the composite part. This can be done by performing viscosity experiments on the same batch of resin used for the DSC experiments. Also, more viscosity data should be collected at lower temperatures where infiltration is most likely to occur.

9.0 MODEL VERIFICATION

A major objective of this research was to verify an analytical computer model of the resin transfer molding process. The process modeled is the two-dimensional in-plane infiltration of a dry textile preform by a reactive epoxy resin. A schematic diagram illustrating the experimental set-up used in this study is provided in Figure 9.1.

Verification of the analytical model was accomplished through flow visualization and mold filling experiments. In this chapter, we will discuss the governing equations of the model and the experimental set-up. The results of the experiments will then be compared to model predictions.

9.1 MODEL DESCRIPTION

A two-dimensional flow model has been developed which can be used to simulate the infiltration behavior of a resin into a dry textile preform. The following assumptions were made in the development of the model: (1) the preform is a porous medium, (2) the preform is heterogeneous and anisotropic, (3) the resin is incompressible and low Reynolds number flow exists, (4) the mold filling process is isothermal, and (5) the mold filling velocity is low.

In this section the governing relationships used to calculate flow front position as a function of time will be presented. Also presented are the boundary conditions necessary for the solution of the governing equations.

9.1.1 Governing Equations

Darcy's Law was used as the governing equation to describe flow through an anisotropic porous medium. For a thin cavity mold, flow is two dimensional and

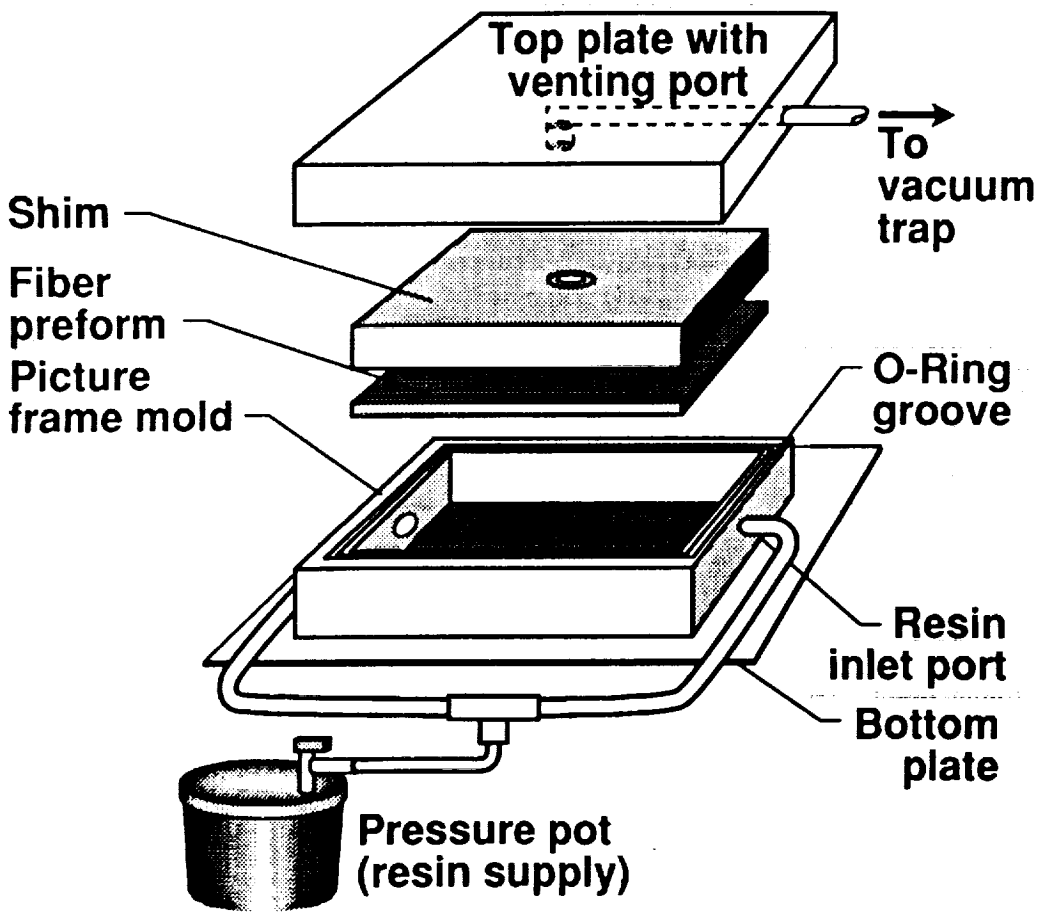

Figure 9.1: Schematic diagram of the Resin Transfer Molding process.

Darcy's Law is expressed as

$$\begin{bmatrix} q_x \\ q_y \end{bmatrix} = -\frac{1}{\mu} \begin{bmatrix} S_{xx} & S_{xy} \\ S_{xy} & S_{yy} \end{bmatrix} \begin{bmatrix} \frac{\partial P}{\partial x} \\ \frac{\partial P}{\partial y} \end{bmatrix} \qquad (9.1.1)$$

where q_x and q_y are the flow rates per unit area in the x and y coordinate directions, respectively. The permeability tensor of the preform is composed of S_{xx}, S_{xy}, and S_{yy} with μ representing the viscosity of the resin. The variables $\partial P/\partial x$ and $\partial P/\partial y$ represent the pressure gradients within the preform. A schematic diagram of the infiltration geometry is presented in Figure 9.2.

The governing equation for resin infiltration into a dry textile preform was then derived by combining Darcy's Law with the continuity equation. This equation has the form

$$\frac{\partial}{\partial x}\left[\frac{-S_{xx}}{\mu}\frac{\partial P}{\partial x} + \frac{-S_{xy}}{\mu}\frac{\partial P}{\partial y}\right] + \frac{\partial}{\partial y}\left[\frac{-S_{xy}}{\mu}\frac{\partial P}{\partial x} + \frac{-S_{yy}}{\mu}\frac{\partial P}{\partial y}\right] = 0 \qquad (9.1.2)$$

The pressure distribution in the infiltrated region of the preform is determined by solving equation (9.1.2). Then, once the pressure distribution is known, the resin velocity at any point within the preform can be calculated from Darcy's Law.

The boundary conditions associated with the governing equation for the model are as follows. For any instant of time, the pressure or flow rate must be specified at each resin inlet port. If the wetting force associated with the resin advancing through the dry preform is neglected, the pressure at the flow front can be set to zero.

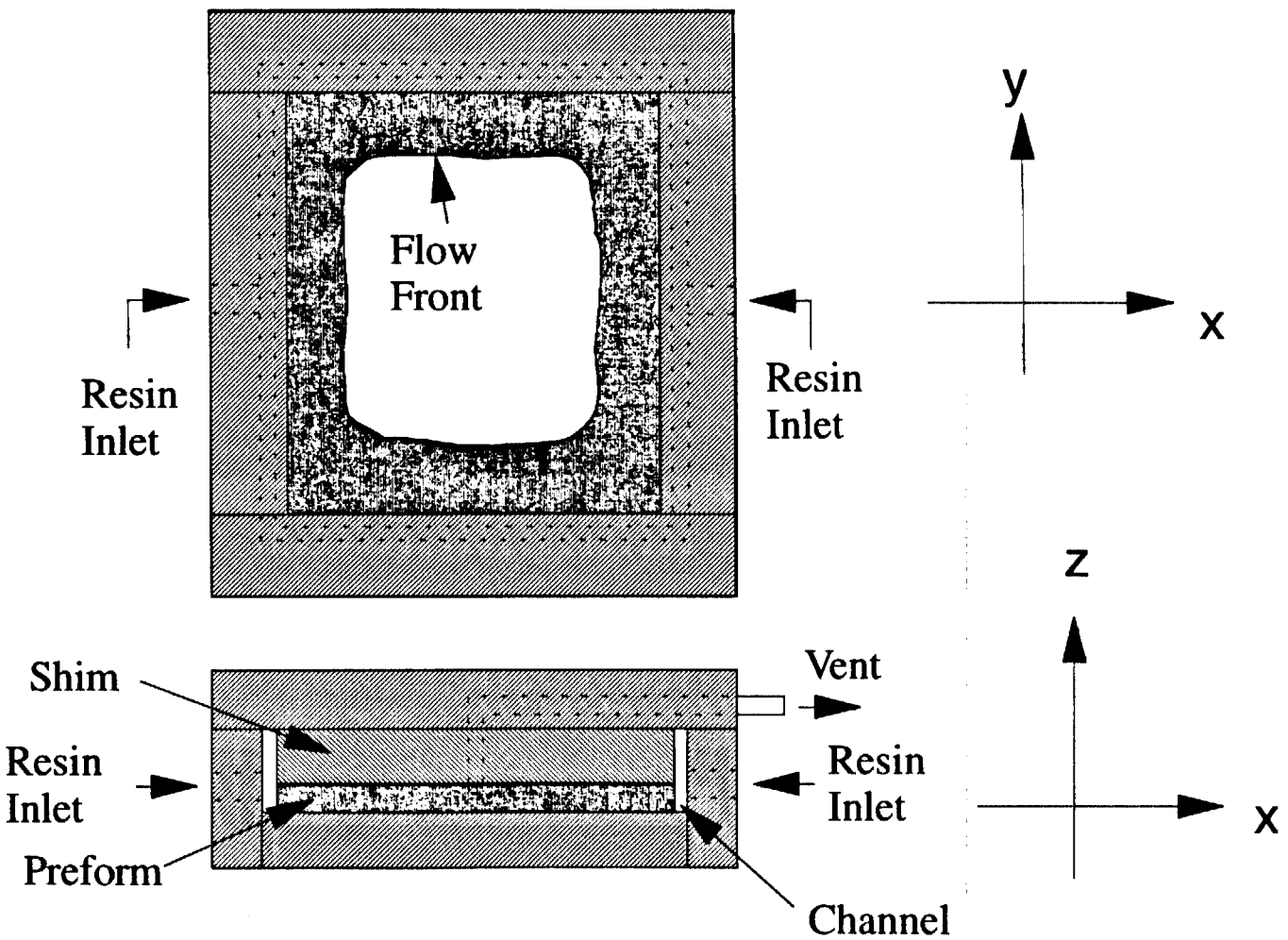

Figure 9.2: Schematic diagram of infiltration geometry.

No flow is allowed to cross the surfaces of the mold. The governing equation for this condition can be written as

$$q_n = -\frac{1}{\mu}\left(S_{nn}\frac{\partial P}{\partial n} + S_{nt}\frac{\partial P}{\partial t}\right) = 0 \qquad (9.1.3)$$

where q_n is the flow rate, and the subscripts n and t represent the directions normal and tangent to the mold walls, respectively.

The numerical solution procedure used in this investigation is based on the finite element/control volume technique [50-54]. The use of finite elements allows for variation in material properties throughout the domain. By using the control volume technique, a fixed mesh can be used to track the flow front position.

A fixed mesh of isoparametric quadrilateral elements are used in the finite element mesh with each element having constant properties. For convenience, the local cartesian coordinate system for each element is aligned with the global coordinate system. PATRAN is used as a pre and post processor for the simulation model.

In the control volume technique, a control volume is constructed around each node in the finite element mesh. This is done by connecting element midsides to element centroids. The amount of resin within each control volume is measured by the nodal fill factor. A fill factor of 0 implies an empty control volume while a fill factor of 1 represents a filled control volume. The flow front is assumed to pass through those control volumes where the fill factor is between 0 and 1.

Further details of the finite element approach and solution procedures can be found in reference [60].

9.1.2 Heat Transfer Analysis

As mentioned earlier, the mold filling process occurs under isothermal conditions. Therefore, a heat transfer analysis is not necessary until infiltration is completed and the resin saturated preform and mold assembly is heated to the final cure temperature. Then, the temperature distribution in the resin saturated preform and degree of cure of the matrix can be calculated from a heat transfer analysis coupled with a cure reaction kinetics model.

In the most general case, the temperature distribution in the preform/mold assembly is three-dimensional. However, since convection is negligible and the largest temperature gradient is in the thickness direction, the temperature distribution in any representative cross-section of the assembly can be determined through the use of a two-dimensional analysis. A schematic diagram of the heat transfer analysis geometry is given in Figure 9.3.

For this analysis, the temperature distribution in the resin saturated preform can be calculated from the transient heat transfer equation for an anisotropic media

$$\rho C_p \frac{\partial T}{\partial t} - \frac{\partial}{\partial x}\left[K_{xx}\frac{\partial T}{\partial x} + K_{xz}\frac{\partial T}{\partial z}\right] - \frac{\partial}{\partial z}\left[K_{xz}\frac{\partial T}{\partial x} + K_{zz}\frac{\partial T}{\partial z}\right] - \rho \dot{H} = 0 \quad (9.1.4)$$

where ρ is the density, C_p is the specific heat, and K_{xx}, K_{xz}, and K_{zz} are the components of the thermal conductivity tensor. The rate of heat generated due to exothermic chemical reactions is denoted by $\dot{H}$.

The transient heat conduction equation of the tool assembly may be written as

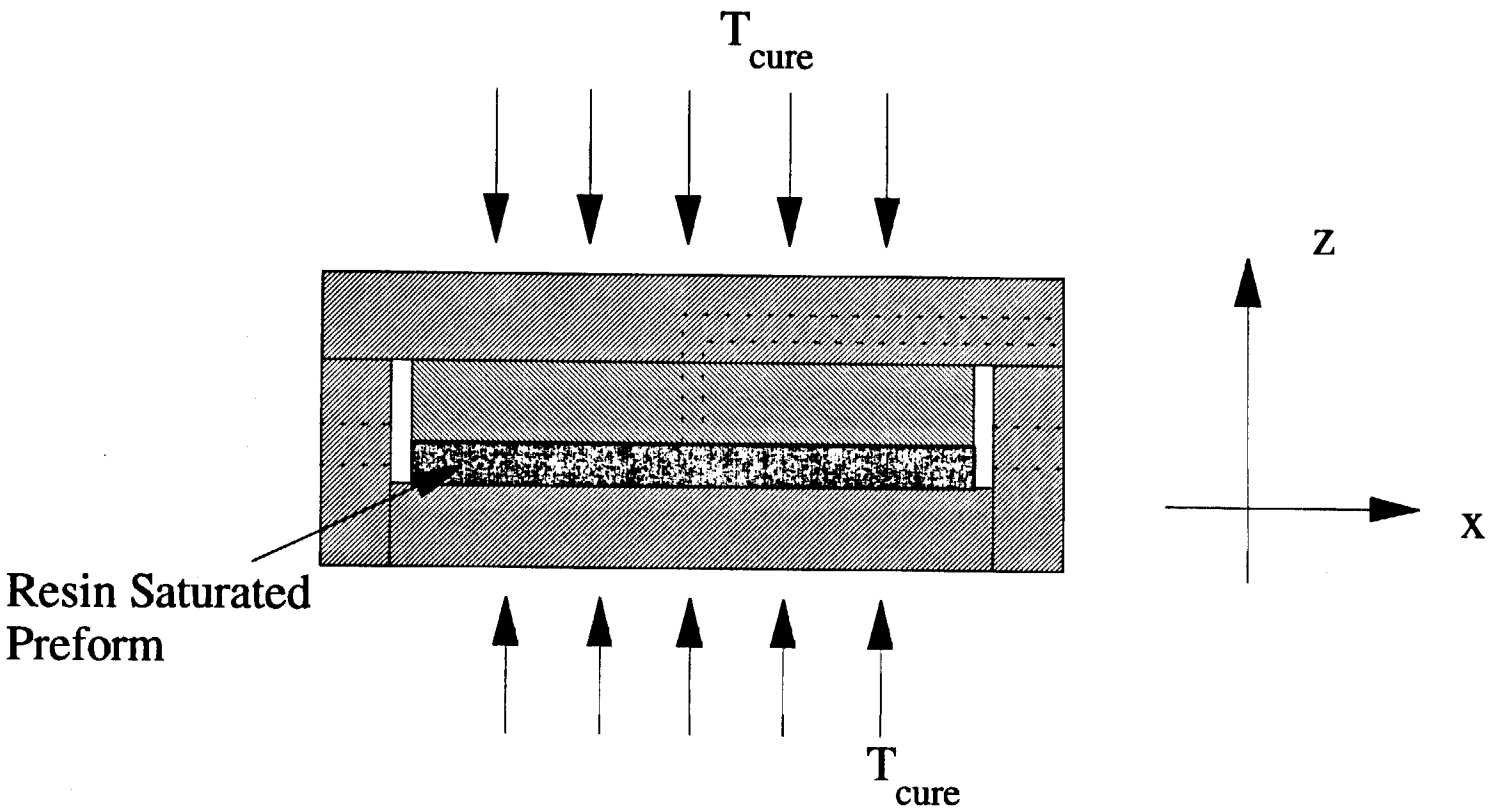

Figure 9.3: Schematic diagram of heat transfer geometry.

$$\rho C_p \frac{\partial T}{\partial t} - \frac{\partial}{\partial x}\left[K_T \frac{\partial T}{\partial x}\right] - \frac{\partial}{\partial z}\left[K_T \frac{\partial T}{\partial z}\right] = 0 \qquad (9.1.5)$$

where K_T is the thermal conductivity of the tool material.

Initial and boundary conditions associated with the heat transfer analysis are as follows. The initial conditions require that the temperature inside the mold assembly be specified prior to the infiltration process. The temperature at the top and bottom of the mold is assumed to be equal to the temperature of the press platens. This boundary condition can be written as

$$T_{top} = T_{bottom} = T_{cure} \qquad (9.1.6)$$

where T_{cure} is the temperature of the platens.

Also, boundary conditions require continuity of temperature and heat flux at the interfaces between different regions of the tool assembly. Heat transfer at the edges is assumed to occur by forced convection with the governing equation written as

$$-\left(K_{nn} \frac{\partial T}{\partial n} + K_{nt} \frac{\partial T}{\partial t} \right)_o = h \left(T_o - T_\infty \right) \qquad (9.1.7)$$

where K_{nn} and K_{nt} are components of the anisotropic thermal conductivity tensor for the solid boundaries. The temperature of the solid boundaries is denoted by T_o, the ambient temperature is denoted by T_∞, and h is the heat transfer coefficient. The subscripts n and t represent the directions normal and tangent to the solid boundaries, respectively.

The finite element method is used to solve the above equations for the heat transfer that occurs during processing. Further details regarding the heat transfer analysis and solution techniques can be found in reference [60].

9.2 EXPERIMENTAL SETUP

In order to verify the accuracy of the infiltration model, flow visualization tests and mold filling experiments were performed. From these tests, data detailing the flow front position as a function of time were recorded to compare to model predictions. This was accomplished through the use of frequency dependent electromagnetic sensors and, for the flow visualization tests, a video camera and a high resolution tape recorder.

9.2.1 Flow Visualization Tests

For the flow visualization tests, a 60.96 cm x 60.96 cm aluminum frame mold was used. The top of the mold was made of 3.81 cm thick poly (methyl methacrylate) to allow for easy observation of the flow front during infiltration. The plexiglas lid was secured in place through the use of an aluminum "picture frame" bolted to the fixture base. The mold had a constant cavity depth of 0.381 cm.

For these tests, a preform composed of eleven (11) layers of style 162 E-glass fabric was used. The use of 11 plies yielded a nominal fiber volume fraction of 43.1%. A 0.3175 cm channel around the preform was utilized to aid in the initial infiltration of the mold. A dyed corn oil was injected into the mold through the use of a constant pressure injection pot. The viscosity of the corn oil was measured with a Brookfield DV-II viscometer.

The infiltration pattern was recorded through the use of a video camera and high

resolution tape recorder. A picture showing the major components of the flow visualization experiments - the flow visualization fixture, the video camera and high resolution tape recorder, and the air pressurized resin pot - is given in Figure 9.4.

The position of the flow front as a function of time was also recorded with Frequency Dependent Electromagnetic Sensing (FDEMS) to further verify the model [54]. Nine sensors were inserted into the bottom plate of the mold in a square array. A diagram illustrating the location of the FDEMS sensors in the visualization fixture is given in Figure 9.5. The sensors were able to monitor the flow front position by detecting a change in capacitance between the dry and wet sensors.

9.2.2 Mold Filling Experiments

For the mold filling tests, a 35.56 cm x 35.56 cm steel picture frame mold was used. The mold had a fixed cavity depth of 0.635 cm with a nominal preform size of 30.48 cm by 30.48 cm. A 0.3175 cm channel surrounded the preform to aid in the initial infiltration. After the preform was placed inside the picture frame, a shim was placed on top of the preform to ensure that the desired fiber volume fraction was reached. A top plate with a venting port connected to a vacuum pump was placed on top of the shim. A diagram illustrating the complete RTM assembly was given earlier in Figure 9.1.

The entire mold assembly was placed in a press and pre-heated to 90 °C. The resin was transferred from the constant displacement injection pump to the mold in high-temperature plastic tubing pre-heated to 90 °C. Vacuum was applied in order to remove any entrapped air in the preform assembly and plastic tubing. Resin injection was started 30 minutes after the application of vacuum. The injection process continued until a steady flow of resin was seen in the exit hose.

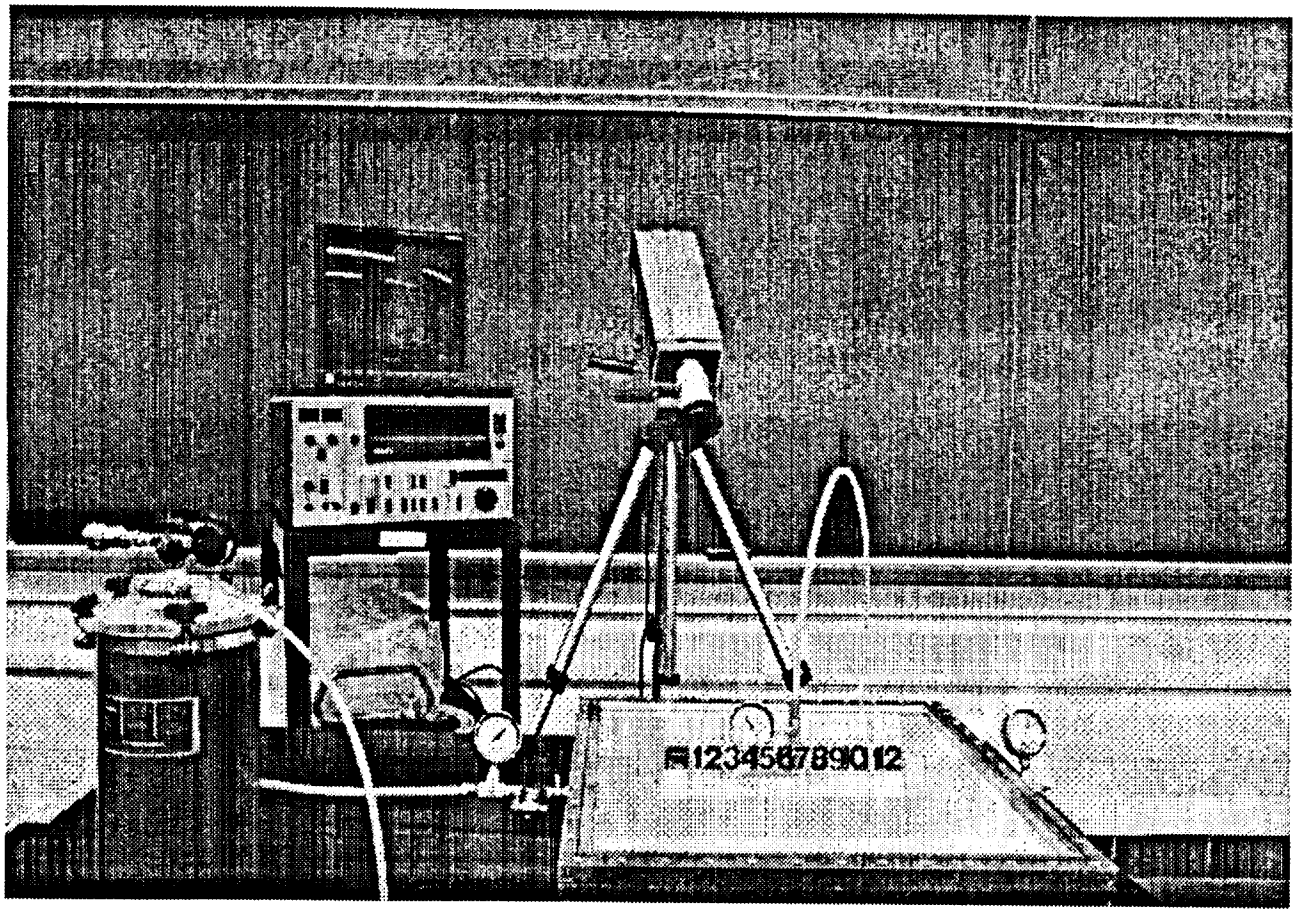

Figure 9.4: Photograph of the major components used in the flow visualization experiments.

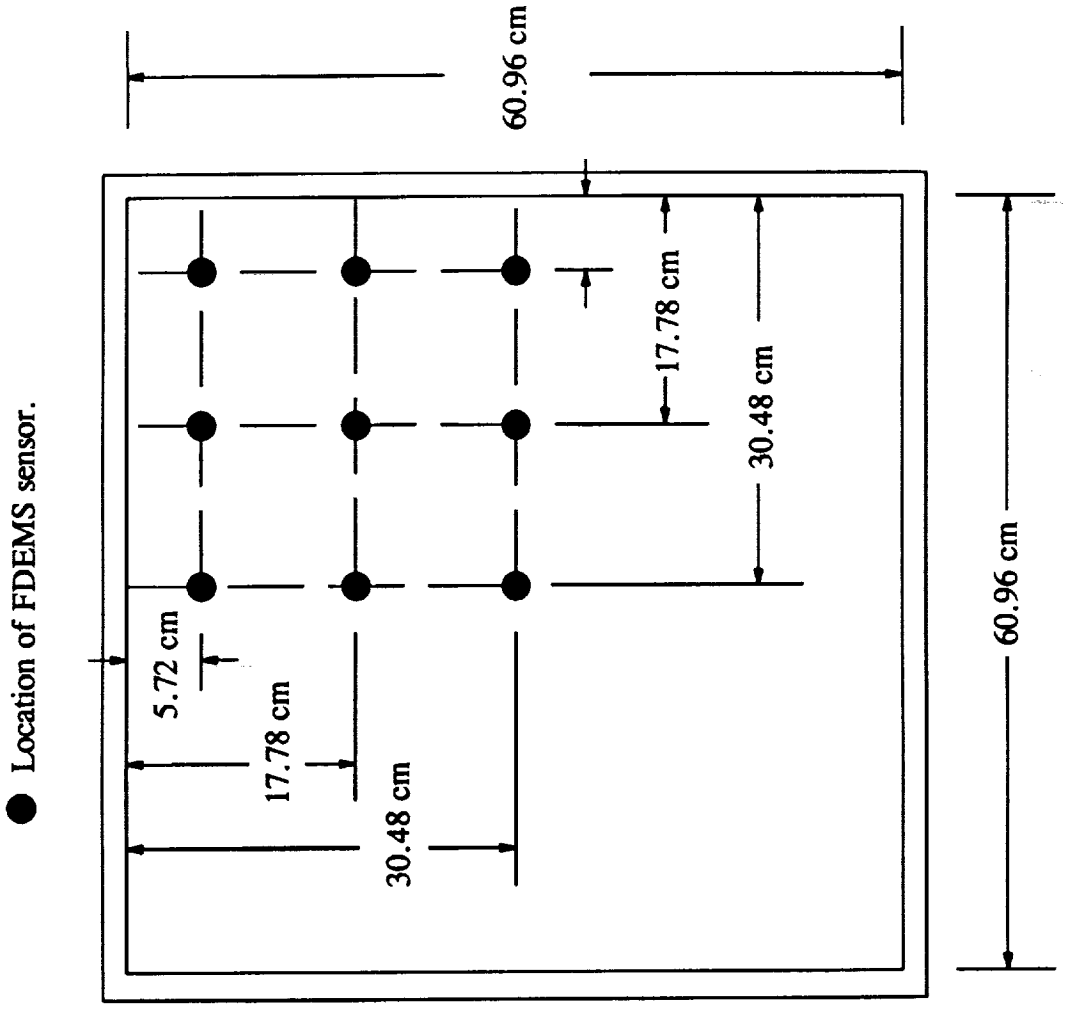

Figure 9.5: Location of FDEMS sensors for flow visualization experiment.

The infiltration pattern as a function of time was monitored through the use of frequency dependent electromagnetic sensors. Six sensors were inserted into the bottom mold plate. Three sensors were placed along the edge of the preform. Two sensors were placed inside the preform with the last sensor placed directly below the exit port located in the center of the top shim plate. An illustration depicting the location of the FDEMS sensors in the bottom plate of the RTM mold is given in Figure 9.6.

Sixteen (16) plies of the TTI IM7/8HS fabric was used to make up the preform. The compacted preform had a nominal fiber volume fraction of 60%. The resin system used in these experiments was Shell 1895/W, mixed in a 3:1 ratio.

9.3 RESULTS

This section will present results from the different flow visualization and mold filling experiments performed to verify the model. Comparisons will be drawn between model-predicted and experimental flow fronts as a function of time. Data gathered from FDEMS sensors used to monitor resin position will also be presented. In addition, the actual degree of cure as measured by the FDEMS sensors will be compared with the degree of cure predicted by the kinetics model presented in chapter 8.

9.3.1 Flow Visualization Experiments

As mentioned earlier, a flow visualization test was performed with corn oil and style 162 E-glass fabric preforms. The viscosity of the corn oil was measured to be 39.6 cp with the fiber volume fraction of the preform equal to 43.1%. The fluid was injected into the mold through a single side port with the injection pressure set at approximately 37.9 kPa. Upon entering the mold cavity, the corn oil fills the 0.3175

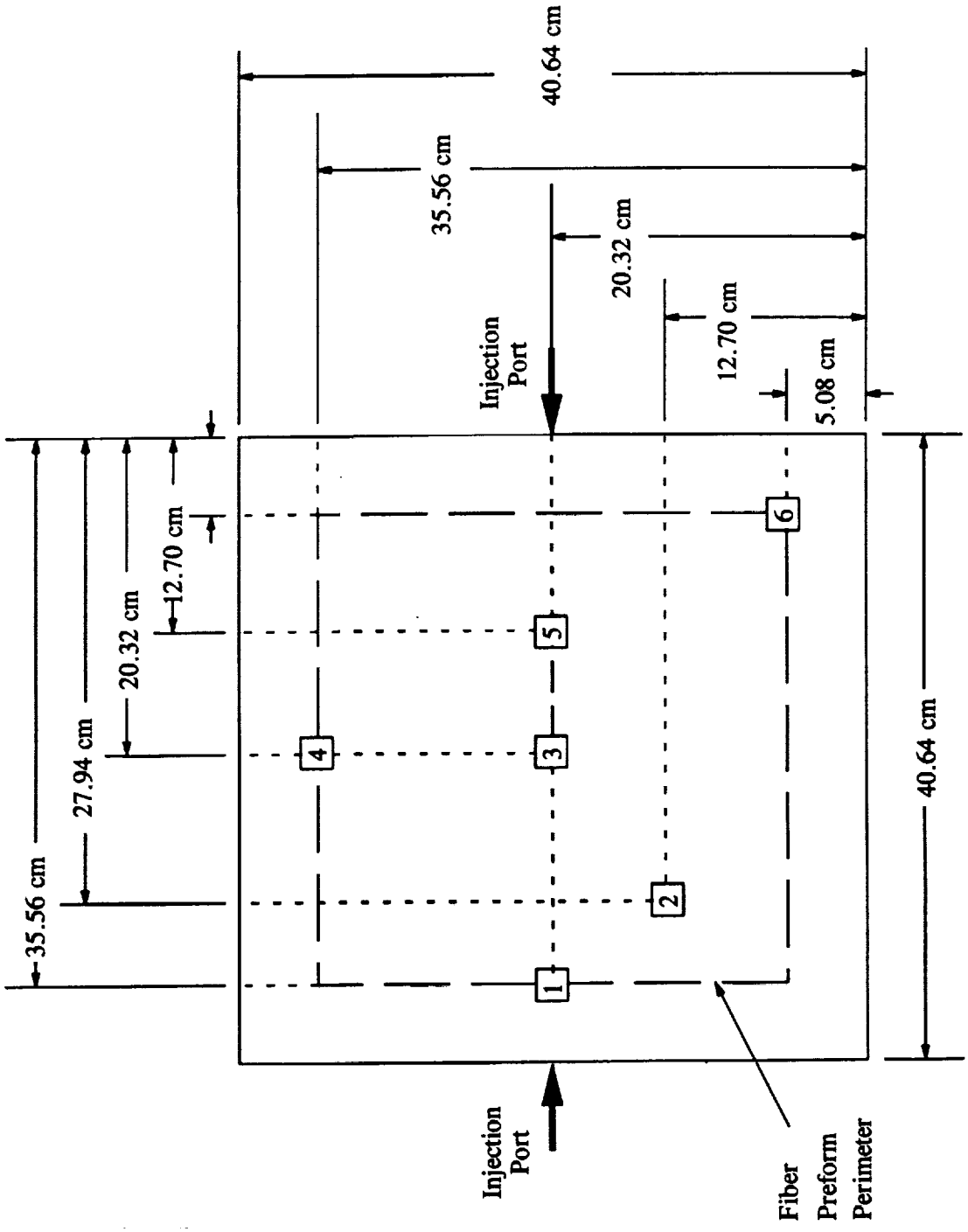

Figure 9.6: Location of FDEMS sensors for mold filling experiments.

cm channel surrounding the preform. The corn oil then infiltrates the preform and exits through the center port located in the plexiglas lid. A diagram of the flow visualization experiment is given in Figure 9.7.

The finite element mesh for the resin infiltration model consisted of 2707 isoparametric quadrilateral elements and a total of 2816 nodes. Because the coordinate axes were coincident with the principal material directions of the fabric, the elements are orthotropic. The measured E-glass fabric warp and fill direction permeabilities at 43% fiber volume fraction were input for each element. One difficulty in modeling this experiment was the drop in resin pressure below the specified injection pressure at the fixture inlet port at the beginning of the test. The pressure at the inlet port remained low until the channel was completely filled with resin. Once resin began to infiltrate the preform, the inlet port pressure increased to the specified injection pressure. Therefore, the inlet port pressure was measured as a function of time during the experiment and the data input into the model as boundary conditions.

Shown in Figures 9.8-9.10 are comparisons between the actual and model-predicted flow fronts at increasing time values. The time at which the image was taken is given in each figure. In each figure, the solid line represents the flow front position predicted by the model for that time value. The dark area of the preform has been saturated by the resin. The dry region of the preform is represented by the white area inside the mold.

From the figures, it can be seen that the model-predicted flow fronts matched the experimental results at the three infiltration times very well. The wavy nature of the experimental flow fronts during infiltration is attributed to the waviness inherent in the plexiglas top plate.

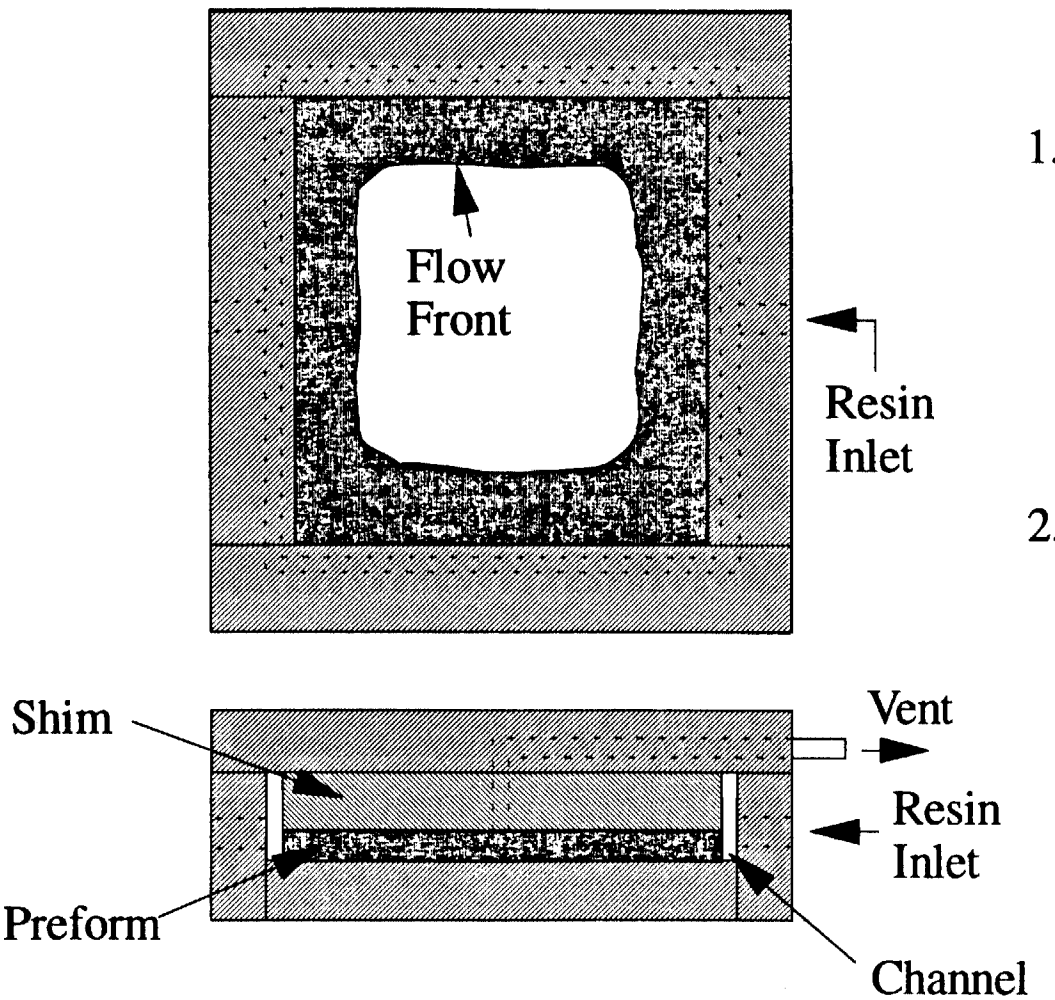

Data

1. Preform
   - 162 E-glass
   - plain weave
   - Thickness =3.81 mm
   - $v_f = 43.1\%$
2. Fluid
   - Dyed corn oil
   - Viscosity = 39.6 cps
   - Injection pressure = 37.9 kPa

Figure 9.7: Schematic diagram of flow visualization experiment.

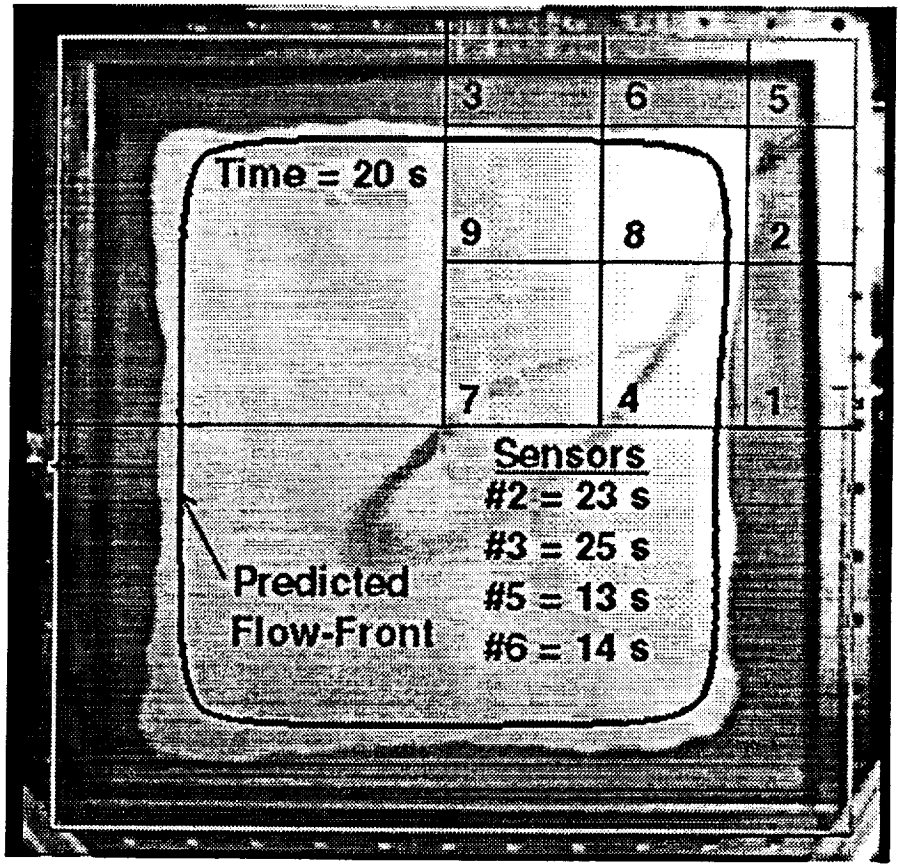

Figure 9.8: Comparison between experimental and model-predicted flow fronts at 20 seconds.

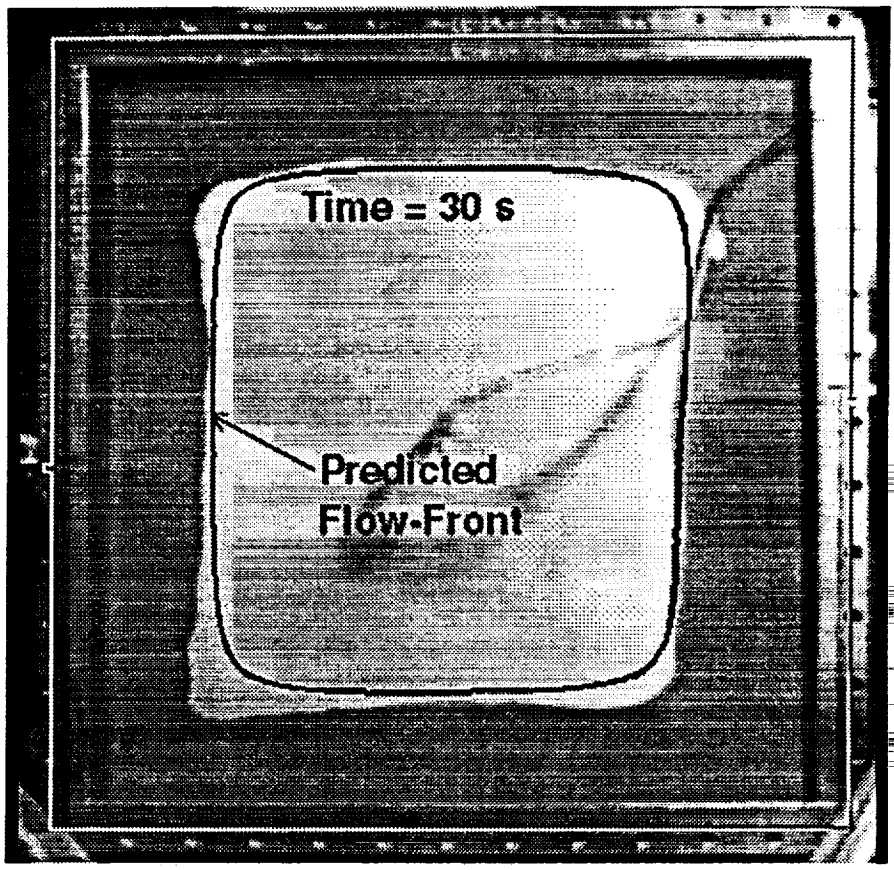

Figure 9.9: Comparison between model-predicted and experimental flow fronts at 30 seconds.

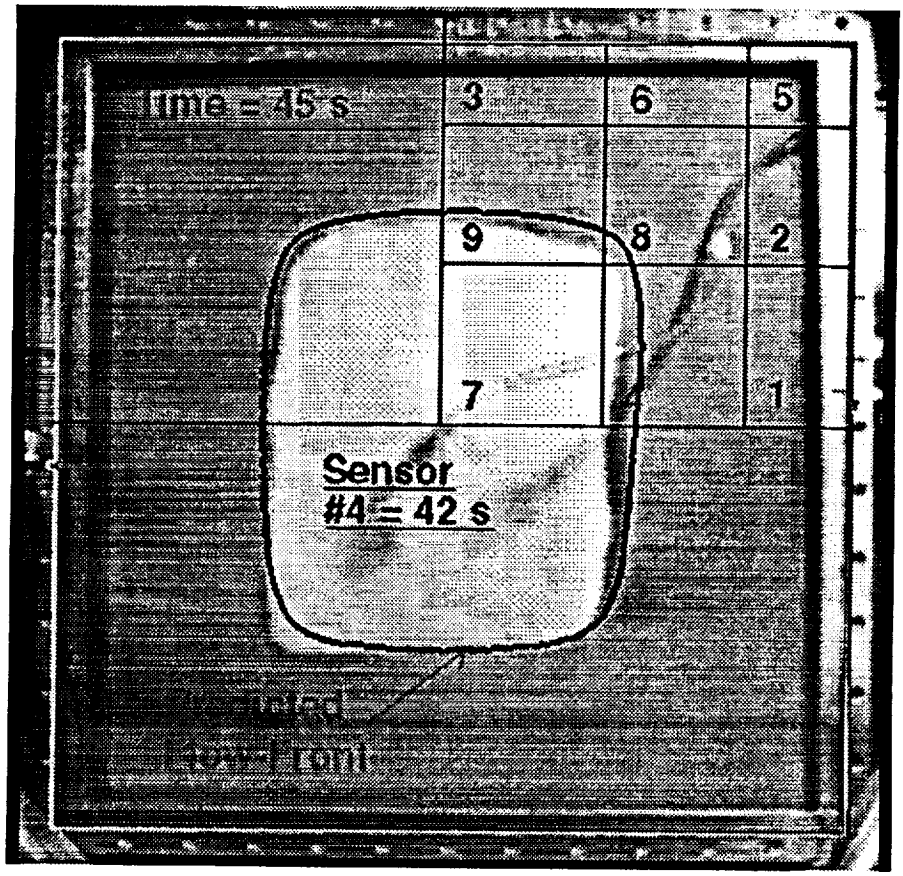

Figure 9.10: Comparison between model-predicted and experimental flow fronts at 45 seconds.

In Figures 9.8 and 9.10, the sensor locations along with sensor wet-out times have been overlaid in order to compare these values with the actual and model-predicted results. The sensors were numbered in the order that they are scanned by the computer measuring system. As can be seen from the figures, the sensors can detect the location of the resin flow front to within 5 seconds of the measured infiltration times.

9.3.2 Mold Filling Experiments

To further verify the model, two mold filling experiments were performed with Shell 1895/W resin and TTI IM7/8HS preforms. A schematic diagram further detailing the mold filling experiments is given in Figure 9.11. The viscosity of the Shell 1895/W system was approximately 120 centipoise. The nominal fiber volume fraction of the TTI preform was 60%. Flow rates of 10 and 20 cc/min were used for these tests. The flow front was tracked as a function of time through the use of six FDEMS sensors.

The results for the 20 cc/min injection experiment are presented in Figure 9.12. The location of the six FDEMS sensors and the corresponding wet-out times are denoted on the figure. The wet-out of sensor #1 was used to approximate the start of the infiltration process. Wet-out times for the internal sensors (#2, 3, and 5) agreed well with model predictions with a maximum error of 13% between model predictions and experimental values at sensor #2. Sensors located along the perimeter of the preform wet-out much faster than predicted by the model. This may be attributed to the difficulty in accurately measuring the dimensions of the channel around the preform in the mold. When the mold is closed and pressure applied, the preform has a tendency to shift which affects the channel dimensions. The edges of the preform tended to be nonuniform.

A comparison of model-predicted and experimental pressure values is presented in

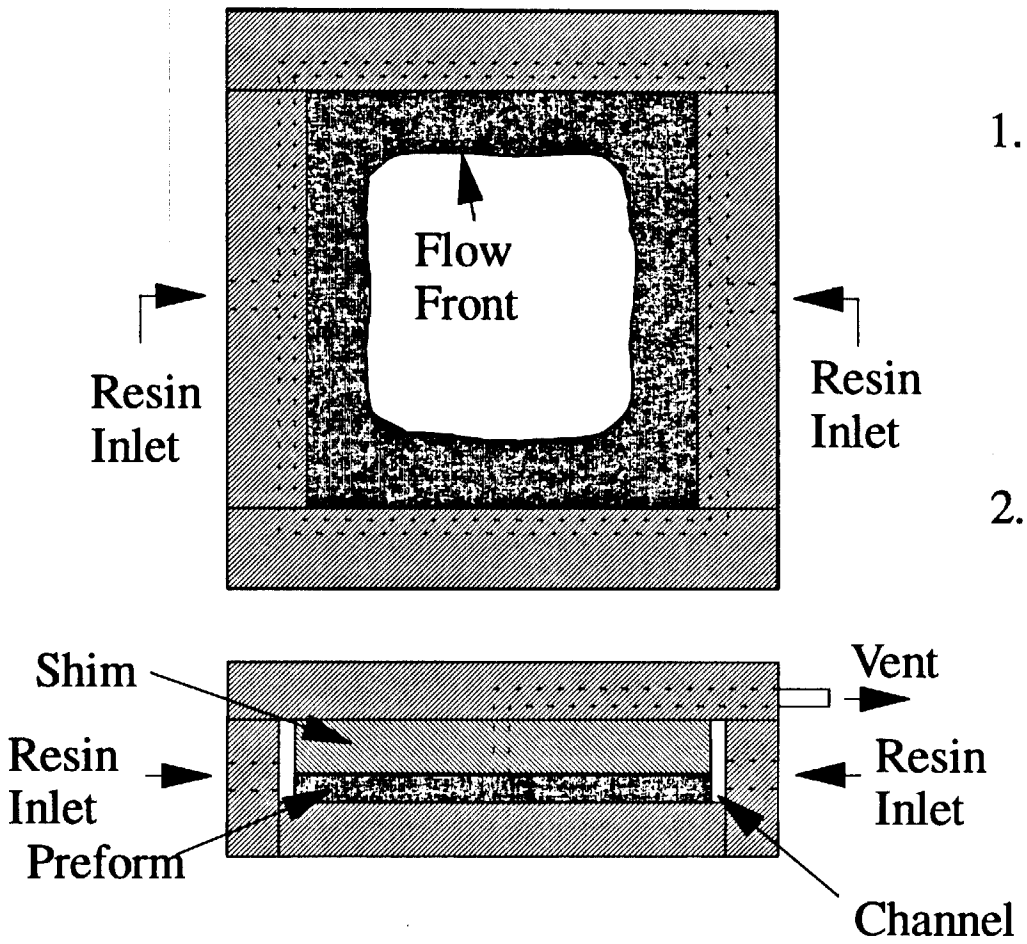

Data

1. Preform
   - IM7 graphite (0^{o})
   - 8-Harness satin
   - Thickness =6.25 mm
   - $\nu_f = 60\%$
2. Fluid
   - Shell 1895/W
   - Viscosity = 120 cps
   - Injection flow rates = 10 and 20 cc/min

Figure 9.11: Schematic diagram of mold filling experiments.

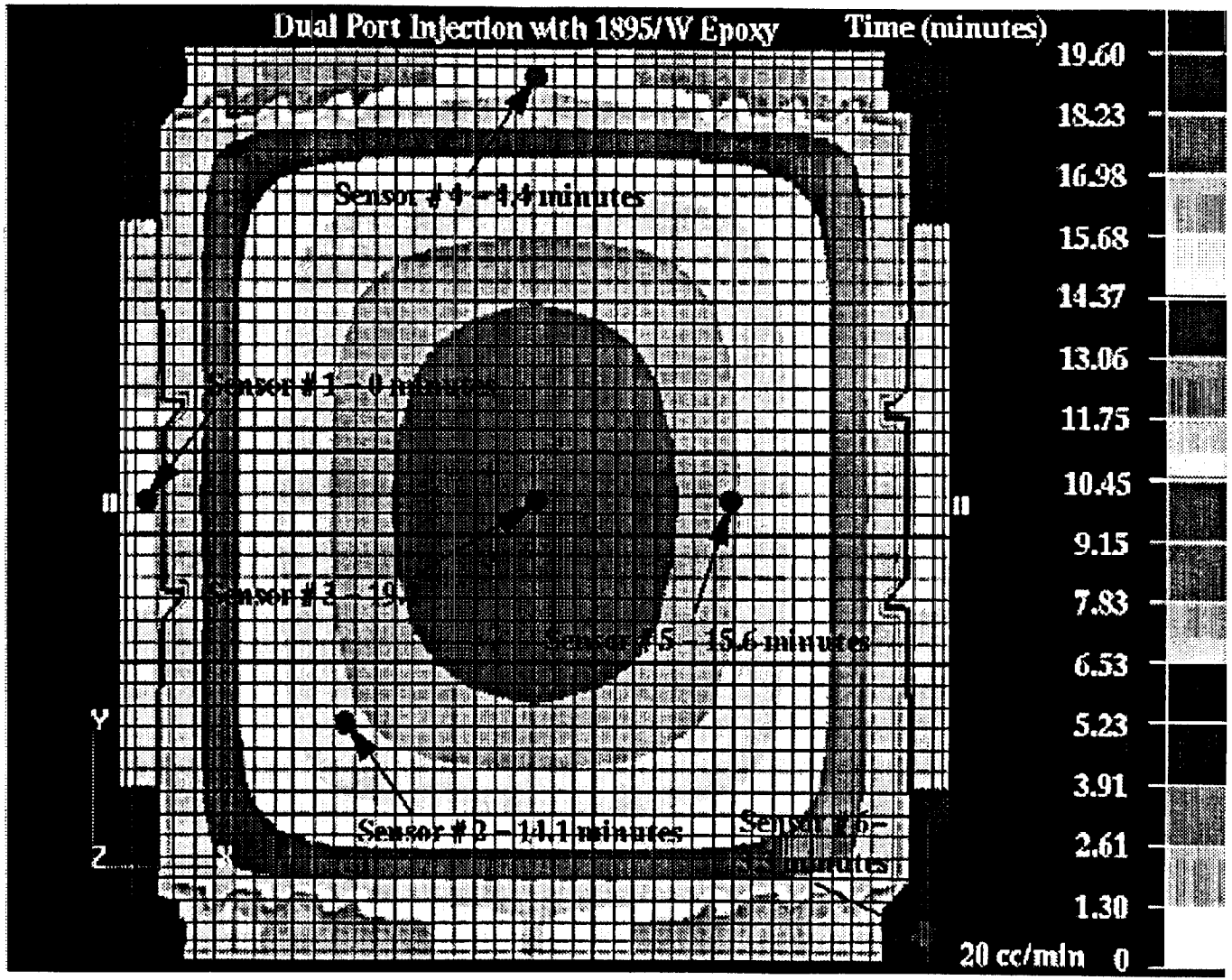

Figure 9.12: Model-predicted and experimental infiltration patterns for a flow rate of 20 cc/min. Sensor locations and wet-out times are shown.

Figure 9.13. In general, there is good agreement between the model generated and experimental values. The difference between the measured and predicted pressure may be attributed to the uncertainty of when mold filling actually begins.

Shown in Figure 9.14 is the predicted infiltration patterns for the flow rate of 10 cc/min. The location of the six FDEMS sensors and the associated wet-out times for each sensor are also given. Again, sensor #1 was used to approximate the beginning of the mold filling process. There is excellent agreement between model-predicted and experimental flow front position as measured by the sensors. Note the skewed flow pattern due to the shifting of the preform during mold closing. By carefully measuring the channel dimensions upon completion of the test, a more accurate prediction of the flow patterns at the beginning of infiltration was obtained.

A comparison between measured and model-predicted mold inlet pressure is shown in Figure 9.15. Pressure readings were taken in the channel adjacent to sensor #4 and in an identical location on the opposite side of the mold. The data indicate that there is virtually no pressure drop within the channel. The model provides an accurate prediction of the rise in inlet pressure as a function of infiltration time. The fluctuations in the model pressure values are attributable to variations in injection flowrates.

After complete infiltration, the manufacturer recommended cure cycle was applied to the saturated preform. The degree of cure as a function of time was recorded through the use of the centrally located FDEMS sensor (sensor #3, Figure 9.6). The experimental values are presented as a function of time in Figure 9.16. Also shown in this figure is the predicted degree of cure using the kinetics model presented in the previous chapter. The agreement between the model-predicted and FDEMS measured degree of cure is very good. For the processing cycle selected, the model

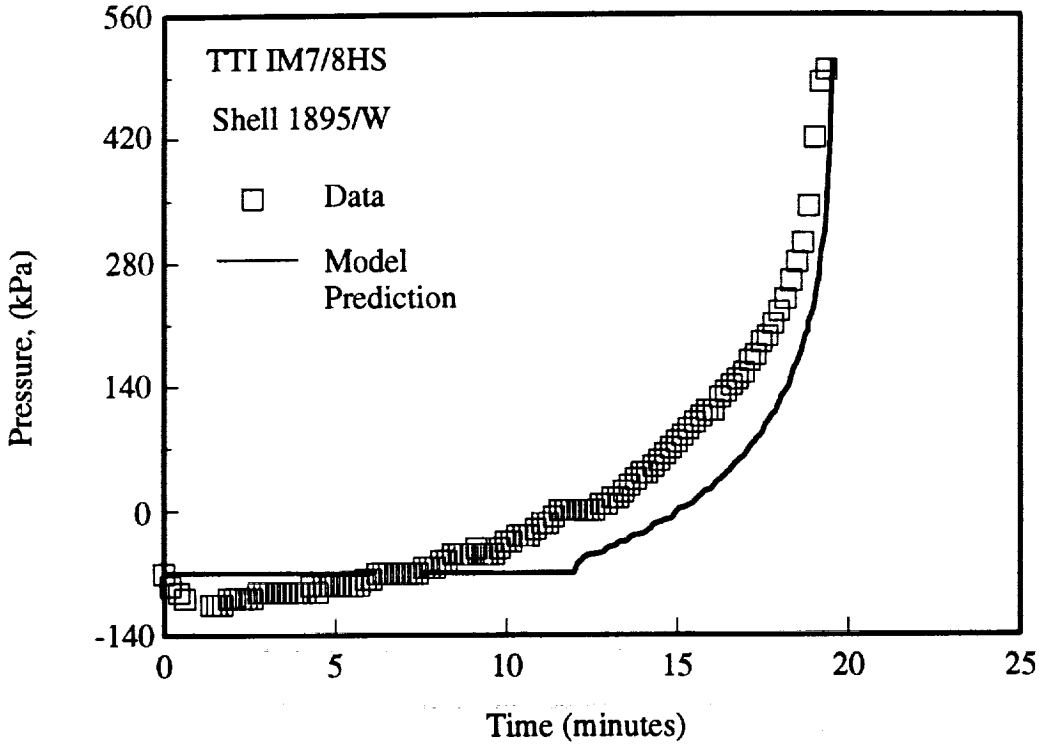

Figure 9.13: Comparison between model-predicted and experimental pressure values at the inlet for a flow rate of 20 cc/min.

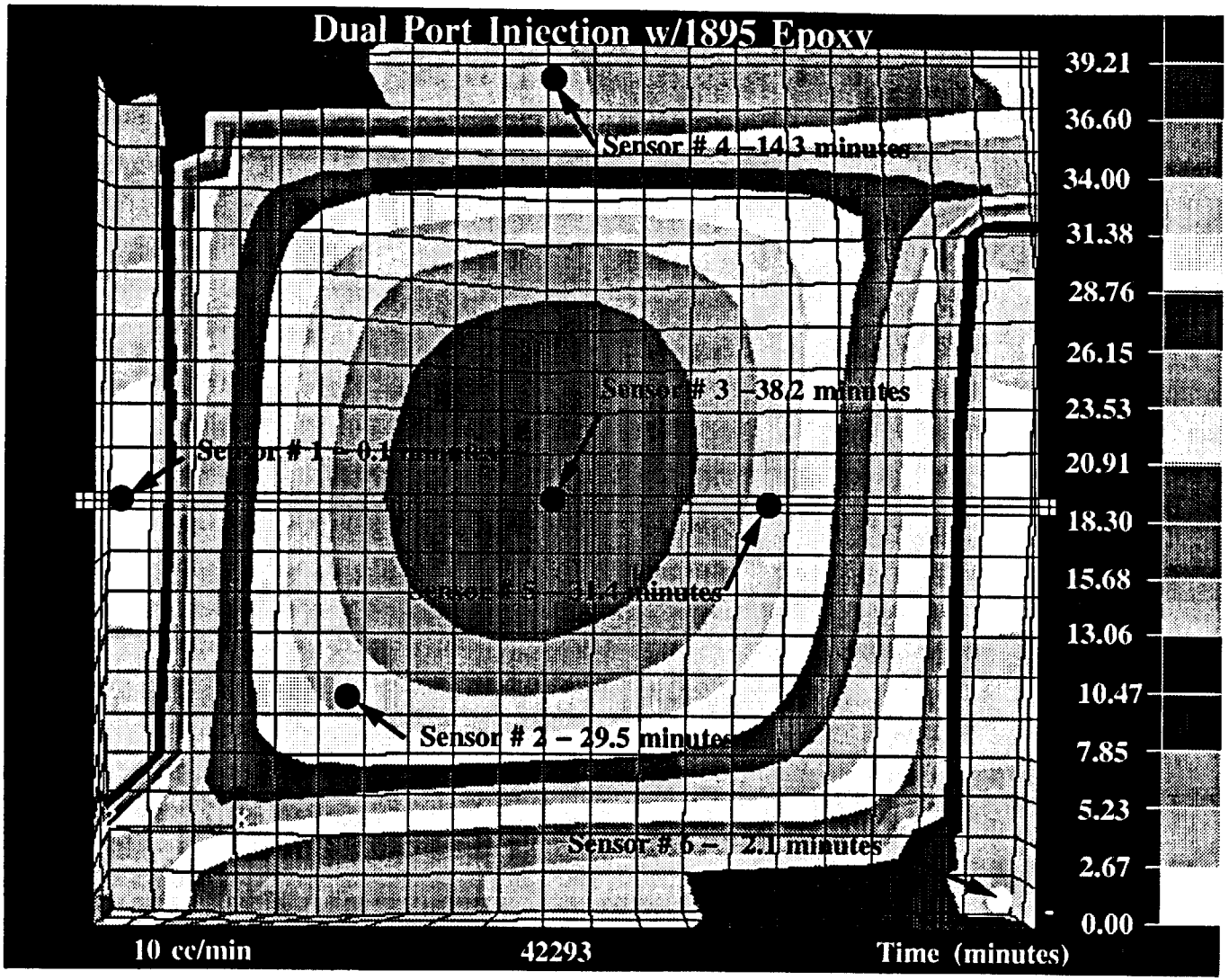

Figure 9.14: Model-predicted and experimental infiltration patterns for a flow rate of 10 cc/min. Sensor locations and wet-out times are shown.

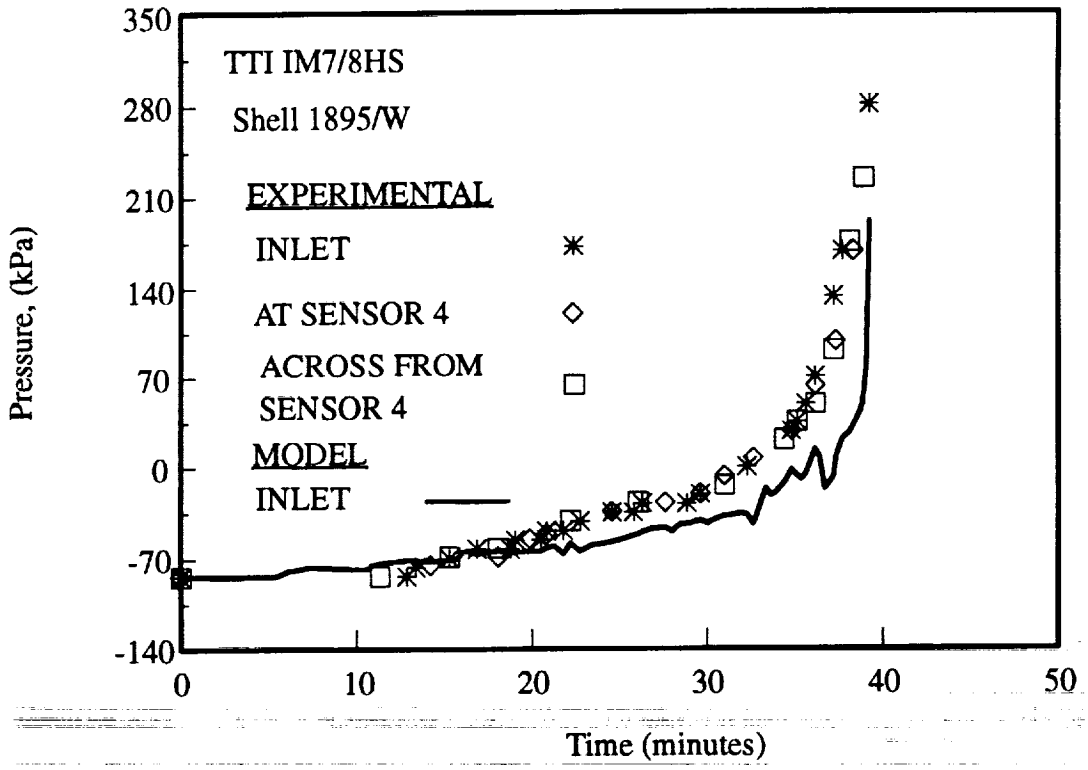

Figure 9.15: Comparison between model-predicted and experimental pressure values at the indicated locations for a flow rate of 10 cc/min.

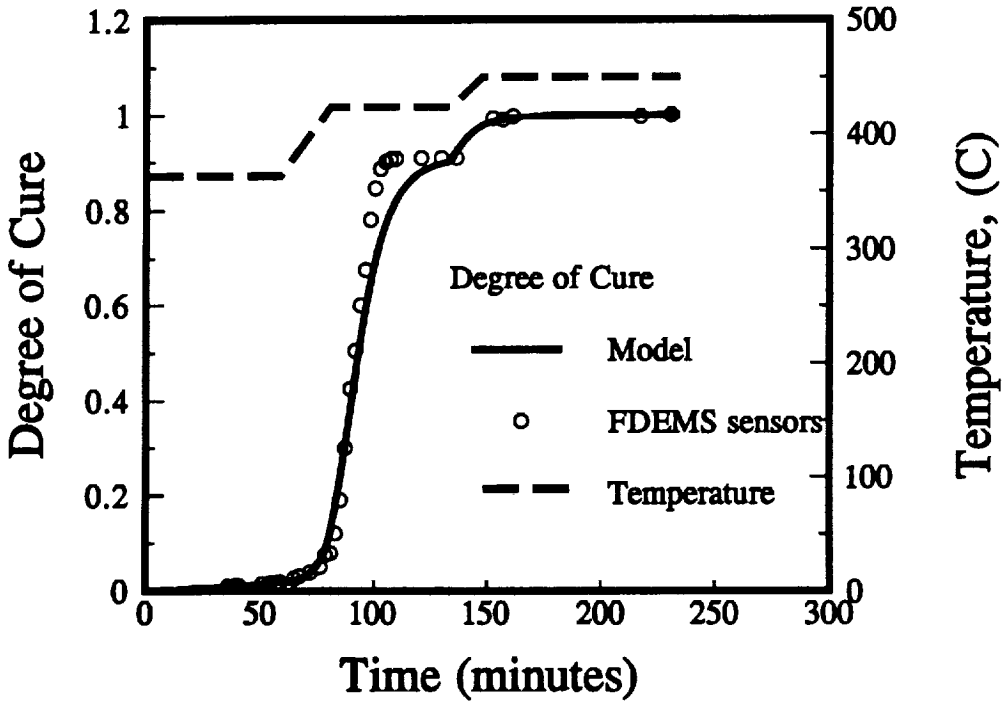

Figure 9.16: Comparison between model-predicted and FDEMS measured degree of cure for the given cure cycle.

predicts that the resin will be fully cured after 150 minutes.

10.0 CONCLUSIONS AND FUTURE WORK

The focus of this research was to verify an analytical model of two-dimensional infiltration of a textile preform. The primary application of this model is the Resin Transfer Molding process. To this end, preform compaction and permeability behavior were experimentally determined. Also, the degree of resin/fiber interaction was measured. Flow visualization and mold filling tests were conducted to verify the computer model. This chapter will discuss conclusions drawn from this research and also recommend possible directions for future work in this area.

10.1 CONCLUSIONS

The compaction and permeability behavior of several textile preforms have been evaluated through the use of experimental test methods. A power law regression model was used to relate fiber volume fraction to compaction pressure. Likewise, a power law regression model was used to correlate permeability to fiber volume fraction. These relationships were then used to provide input data for the two-dimensional infiltration model.

From the compaction tests, it was found that the simple weave pattern of the 162 E-glass fabric required more compaction pressure than that of the 8 harness satin weave used in the TTI IM7/8HS and Fiberite HMF 2474 preforms.

Through-the-thickness permeability tests showed that the 162 E-glass preform had a greater permeability than either the TTI IM7/8HS or the Fiberite HMF 2474 preforms. In the case of the Saerbeck preform tested with corn oil, through-the-thickness stitching was found to increase the permeability by approximately 5 times due to the creation of flow pathways not available in the unstitched preform.

Steady state permeability tests conducted with both corn oil and Epon 815 indicated that fluid viscosity did not significantly influence the permeability behavior of a TTI IM7/8HS or 162 E-glass preform. In addition, permeability values determined from steady state and advancing front tests were similar. This behavior was found for the warp direction of the 162 E-glass fabric when tested with both corn oil and Epon 815. This behavior was also found to occur for TTI IM7/8HS fabrics tested with corn oil.

The amount of interaction between the two fibers, glass and carbon, with corn oil and epoxy was determined by measuring the contact angle for the different systems. It was found that the Epon 815 wets out both fibers better than the corn oil. The contact angles for the 162 E-glass fiber was lower than that of the TTI IM7/8HS fiber for both the Epon 815 and corn oil. This may result from the sizing commonly used on the carbon fiber.

A kinetics model for the Shell 1895/W system has been developed based on isothermal DSC data. The accuracy of the kinetics model was verified through comparison with both dynamic DSC scans and experimental data gathered during the RTM process. The experimental RTM data were gathered by FDEMS sensors inserted into the bottom tool plate of the RTM mold. A viscosity model for the Shell 1895/W system was also generated. The viscosity model was used primarily to ensure that complete infiltration would occur prior to resin gel.

A two-dimensional model for use in simulating the infiltration of a resin into a dry textile preform. It has been shown through flow visualization and mold filling experiments that the analytical computer model can successfully predict resin flow front position and total infiltration time for the RTM process. The model can also accurately predict the rise in fluid pressure that occurs during injection.

10.2 FUTURE WORK

The next step in this research is to use the resin transfer molding process to manufacture flat panels. These panels should be evaluated for manufacturing defects and mechanical properties. Once the standard injection procedure is perfected, work should focus on optimizing both the injection process and following cure cycle to minimize the processing cycle while maximizing composite properties. Studies could also be performed to correlate injection temperatures and flow rates to mechanical properties.

In addition, work should continue in characterizing emerging preforms and resin systems for possible use in the resin transfer molding process. This would result in a large data base available to composite manufacturers for future reference.

The effect of sample size on the in-plane permeability behavior should be further investigated. Also, further steady state permeability tests with an epoxy based fluid are necessary to substantiate the early findings reported in this work. More advancing front tests are necessary at higher fiber volume fractions to determine if the similarity between steady state and advancing front permeability values exist at the higher fiber volume fractions. These advancing front tests need to be done in all of the primary directions of the textile preform.

REFERENCES

[1] Johnson, C. F. "Resin Transfer Molding." Engineered Materials Handbook, Volume 1: Composites. Metals Park, Ohio: ASM International, 1987.

[2] Darcy, H. Les Fontaines Publiques de la Villa de Dijon. Dalmount: 1856.

[3] Gali, E. "Resin Transfer Molding: A Cost Effective Alternative," Plastic Design Forum, March/April 1982, 47-56.

[4] Kim, Y. R., S. P. McCarthy, J. P. Fanucci, S. C. Nolet, and C. Koppernaes. "Resin Flow Through Fiber Reinforcements During Composite Processing," in L. D. Michelove et al. (eds.), 22nd International SAMPE Technical Conference, SAMPE, Covina, Ca., 1990, 709-723.

[5] Gutowski, T. G., T. Morigaki, and Z. Cai. "The Consolidation of Laminate Composites." Journal of Composite Materials, Vol. 21 (1987): 172-188.

[6] Gutowski, T. G., Z. Cai, S. Bauer, D. Boucher, J. Kingery, and S. Wineman. "Consolidation Experiments For Laminate Composites." Journal of Composite Materials, Vol. 21 (1987): 650-669.

[7] Gebart, B. R. "Permeability of Unidirectional Reinforcements for RTM." Journal of Composite Materials, Vol. 26 (1992): 1100-1133.

[8] Skartsis, L., J. L. Kardos, and B. Khomami. "Resin Flow Through Fiber Beds During Composite Manufacturing Processes. Part I: Review of Newtonian Flow Through Fiber Beds." Polymer Engineering and Science, Vol. 32, No. 4 (February 1992): 221-230.

[9] Adams, K. L., B. Miller, and L. Rebenfeld. "Forced In-plane Flow of an Epoxy Resin in Fibrous Networks." Polymer Engineering and Science, Vol. 26, No. 20 (Mid-November 1986): 1434-1441.

[10] Lam, R. C. and J. L. Kardos. "The Permeability of Aligned and Cross-Plied Fiber Beds During Processing of Continuous Fiber Composites," Proceedings of the American Society for Composites Second Technical Conference, 1988, 3-11.

[11] Molnar, J. A., L. Trevino, and L. J. Lee. "Mold Filling in Structural RIM and Resin Transfer Molding," Proceedings of the 44th Annual Conference, February 6-9, 1989, Composites Institute, Society of the Plastics Industry, 1989, Session 20A.

[12] Adams, K. L. and L. Rebenfeld. "Permeability Characteristics of Multilayer Fiber Reinforcements. Part I: Experimental Observations." Polymer Composites, Vol. 12, No. 3 (June 1991): 179-185.

[13] Trevino, L., K. Rupel, W. B. Young, M. J. Liou, and L. J. Lee. "Analysis of Resin Injection Molding in Molds with Preplaced Fiber Mats. I: Permeability and Compressibility Measurements." Polymer Composites, Vol. 12, No. 1 (February 1991): 20-29.

[14] Molnar, J. A., L. Trevino, and L. J. Lee. "Mold Filling in SRIM and RTM: Controlling a Critical Process Parameter," Modern Plastics, September 1989, 120-126.

[15] Weideman, M. H. "An Infiltration/Cure Simulation Model for Manufacture of Fabric Composites by the Resin Infusion Process." Master's Thesis, Virginia Polytechnic Institute and State University, 1992.

[16] Batch, G. L. and S. Cumiskey. "Multilayer Compaction and Flow in Composites Processing," Proceedings of the 45th Annual Conference, February 12-15,1990, Composites Institute, Society of the Plastics Industry, 1990, Session 9A.

[17] Williams, J. G., C. E. M. Morris, and B. C. Ennis. "Liquid Flow Through Aligned Fiber Beds." Polymer Engineering and Science, Vol. 14, No. 6 (June 1974): 413-419.

[18] Foley, M. F. and T. Gutowski. "The Effect of Process Variables on Permeability in the Flexible Resin Transfer Molding (FRTM) Process," in R. L. Carri, L. M. Poveromo, and J. Gauland (eds). 23rd International SAMPE Technical Conference, SAMPE, Covina, Ca., 1991, 326-340.

[19] Ahn, K. J., J. C. Seferis, and J. C. Berg "Simultaneous Measurements of Permeability and Capillary Pressure of Thermosetting Matrices in Woven Fabric Reinforcements." Polymer Composites, Vol. 12, No. 3 (June 1991): 146-152.

[20] Peterson, R. C. and R. E. Robertson. "Flow Characteristics of Polymer Resin Through Glass Fiber Preforms in Resin Transfer Molding," Advanced Composite Materials: New Developments and Applications: Proceedings of the Seventh Annual ASM/ESD Advanced Composites Conference, ASM International, Materials Park, Ohio, 1991, 203-208.

[21] Skartsis, L., B. Khomami, and J. L. Kardos. "The Effect of Capillary Pressure on the Impregnation of Fibrous Media." SAMPE Journal, Vol. 28, No. 5 (September/October 1992): 19-24.

[22] Dave, R. and S. Houle. "The Role of Permeability During Resin Transfer Molding," Proceedings of American Society for Composites Fourth Technical Conference: Composite Materials Systems, 1990, 539-547.

[23] Bear, Jacob, Carol Braester, and Pascal C. Menier. "Effective and Relative Permeabilities of Anisotropic Porous Media," Transport in Porous Media 2, D. Reidel Publishing Company, (1987), pp. 301-316.

[24] Odeh, A. S. "Effect of Viscosity Ratio on Relative Permeability." Petroleum Transactions, AIME, Vol. 216 (1959): 346-353.

[25] McCaffery, F. G. and D. W. Bennion. "The Effect of Wettability on Two-Phase Relative Permeabilities." The Journal of Canadian Petroleum Technology, (October-December, 1974): 42-53.

[26] Dave, R. "A Unified Approach to Modeling Resin Flow During Composite Processing." Journal of Composite Materials, Vol. 24 (1990): 22-41.

[27] Martin, G. Q. and J. S. Son. Advanced Composites, the Latest Developments; Proceedings of the Second Conference on Advanced Composites, ASM International, 1986, 149.

[28] Pollard, M. "Permeabilities of Fiber Mats Used in Resin Transfer Molding," in T. S. Reinhart et al. (eds.), 24th International SAMPE Technical Conference, SAMPE, Covina, Ca., 1992, T408-T420.

[29] Cercon, L. "Optimizing Fiber Wetout for Composites Manufacturing." Polymer Composites, Vol. 12, No. 2 (April 1991): 81-86.

[30] Patel, N., M. J. Perry, and L. J. Lee. "Influence of RTM and SRIM Processing Parameters on Molding and Mechanical Properties." Advanced Composite Materials: New Developments and Applications; Proceedings of the Seventh Annual ASM/ESD Advanced Composites Conference, ASM International, Materials Park, Ohio, 1991, 105-113.

[31] Patel, N., V. Rohatgi, and L. J. Lee. "Influence of Processing and Material Variables on Resin-Fiber Interface in Liquid Composite Molding." Polymer

Composites, Vol. 14, No. 2 (April 1993): 161-172.

[32] Gauvin, R. and M. Chibani. "Analysis of Composites Molding with Woven and Non Woven Reinforcements," Proceedings of the 45th Annual Conference, February 12-15, 1990, Composites Institute, Society of the Plastics Industry, 1990, Session 9F.

[33] Greve, B. N. and J. K. Soh. "Directional Permeability Measurement of Fiberglass Reinforcements," Polymer Composites for Structural Automotive Applications, 1990, 101-113.

[34] Parnas, R. S. and F. R. Phelan, Jr. "The Effects of Heterogeneities in Resin Transfer Molding Preforms on Mold Filling," in J. Stinson, R. Adsit, and F. Gordaninejad (eds.), 36th International SAMPE Symposium, SAMPE, Covina, Ca., 1991, 506-520.

[35] Phelan, Jr, F. R. "Modeling of Microscale Flow in Fibrous Porous Media," Advanced Composite Materials: New Developments and Applications; Proceedings of the Seventh Annual ASM/ESD Advanced Composites Conference, ASM International, Materials Park, Ohio, 1991, 175-185.

[36] Sadiq, T., R. Parnas, and S. Advani. "Experimental Investigation of Flow in Resin Transfer Molding," in T. S. Reinhart et al. (eds.), 24th International SAMPE Technical Conference, SAMPE, Covina, Ca., 1992, T660-T674.

[37] Bruschke, M. V. and S. G. Advani. "Flow of Generalized Newtonian Fluids Across a Periodic Array of Cylinders." Journal of Rheology, Vol. 37, Issue 3, (May/June 1993): 479-498.

[38] Berdichevsky, A. and Z. Cai. "Preform Permeability Predictions by Self-Consistent Method and Finite Element Simulation." Polymer Composites, Vol. 14, No. 2 (April 1993): 132-143.

[39] Astrom, B. T., R. B. Pipes, and S. G. Advani. "On Flow Through Aligned Fiber Beds and its Applications to Composite Processing." Journal of Composite Materials, Vol. 26 (1992): 1351-1373.

[40] Loos, A. C. and M. H. Weideman. "RTM Process Modeling for Advanced Fiber Architectures," Advanced Composite Materials: New Developments and Applications; Proceedings of the Seventh Annual ASM/ESD Advanced Composites Conference, ASM International, Materials Park, Ohio, 1991, 209-

216.

[41] Young, W. B., K. Rupel, K. Han, L. J. Lee, and M. J. Liou. "Simulation and Experimental Verification of Mold Filling in Resin Transfer Molding and Structural RIM," Proceedings of the 45th Annual Conference, February 12-15, 1990, Composites Institute, Society of the Plastics Industry, 1990, Session 9D.

[42] Chan, A. W. and R. J. Morgan. "Modeling Preform Impregnation and Void Formation in Resin Transfer Molding of Unidirectional Composites." SAMPE Quarterly, (April 1992): 48-52.

[43] Cai, Z. "Mold Filling Analysis of RTM Process." Journal of Composite Materials, Vol. 26 (1992): 1310 - 1338.

[44] Coulter, J. P. and S. I. Guceri. "Resin Impregnation During the Manufacturing of Composite Materials Subject to Prescribed Injection Rate." Journal of Reinforced Plastics and Composites, Vol. 7 (May 1988): 200-219.

[45] Coulter, J. P. and S. I. Guceri. "Resin Impregnation During the Manufacture of Thermoplastic Matrix Composite Materials," **Advances in Thermoplastic Matrix Composite Materials**, ASTM STP 1044, 1989, 14-32.

[46] Coulter, J. P. and S. I. Guceri. "Resin Impregnation During Composite Manufacturing: Theory and Experimentation." Composites Science and Technology, Vol. 35 (1989): 317-330.

[47] Li, S. and R. Gauvin. "Numerical Analysis of the Resin Flow in Resin Transfer Molding." Journal of Reinforced Plastics and Composites, Vol. 10 (May 1991): 314-327.

[48] Trochu, F. and R. Gauvin. "Limitations of a Boundary Fitted Finite Difference Method for the Simulation of the Resin Transfer Molding Process." Journal of Reinforced Plastics and Composites, Vol. 11 (July 1992): 772-786.

[49] Chan, A. W. and S. T. Hwang. "Modeling Nonisothermal Impregnation of Fibrous Media With Reactive Polymer Resin." Polymer Engineering and Science, Vol. 32, No. 5 (Mid-March 1992): 310-318.

[50] Fracchia, C. A., J. Castro, and C. L. Tucker, III. "A Finite Element/Control Volume Simulation of Resin Transfer Mold Filling," Proceedings of the American Society for Composites Third Technical Conference: Integrated

Composites Technology, 1989, 157-166.

[51] Osswald, T. A. and C. L. Tucker, III. "Compression Mold Filling Simulation for Non Planar Parts." International Polymer Processing V, 1990, 79-87.

[52] Bruschke, M. V. and S. G. Advani. "A Finite Element/Control Volume Approach to Mold Filling in Anisotropic Porous Media." Polymer Composites, Vol. 11, No. 6 (December 1990): 398-405.

[53] Bruschke, M. V. and S. G. Advani. "RTM: Filling Simulation of Complex Three Dimensional Shell-Like Structures." SAMPE Quarterly (October 1991): 2-11.

[54] Loos, A. C., J. D. MacRae, V. H. Hammond, D. E. Kranbuehl, S. M. Hart, G. H. Hasko, and A. M. Markus. "Analytical Modeling and Sensor Monitoring for Optimal Processing of Advanced Textile Structural Composites by Resin Transfer Molding," Third NASA Advanced Composite Technology Conference, NASA-CP-3178, 1992, 361-379.

[55] Dexter, H. B. and G. H. Hasko. "Performance of Resin Transfer Molded Multiaxial Warp Knit Composites," Third NASA Advanced Composite Technology Conference, NASA-CP-3178, 1992, 231-261.

[56] Shell Chemical Company, Preliminary Technical Bulletin SC: 1376-92, Houston, Texas, 1992.

[57] Dusi, M. R., W. I. Lee, P. R. Ciriscioli, and G. S. Springer. "Cure Kinetics and Viscosity of Fiberite 976 Resin." Journal of Composite Materials, Vol. 21 (March 1987): 243-261.

[58] Chen, Y.-T. and C. W. Macosko. "Chemorheology of Polycyanate for Resin Transfer Molding," in T. S. Reinhart et al. (eds.), 24th International SAMPE Technical Conference, SAMPE, Covina, Ca., 1992, T630-T644.

[59] Lin, R. J., L. J. Lee, and M. J. Liou. "Mold Filling and Curing Analysis in Liquid Composite Molding." Polymer Composites, Vol. 14, No. 1 (February 1993): 71-81.

[60] MacRae, J. D. "Development and Verification of a Resin Film Infusion/Resin Transfer Molding Simulation Model for Fabrication of Advanced Textile Composites." Master's Thesis, Virginia Polytechnic Institute and State University, 1993.

APPENDIX A: DSC DATA FOR SHELL 1895/W SYSTEM

The data gathered from DSC experiments on the Shell 1895/W system will be presented in this chapter. This data will include the elapsed time of the scan, the area under the curve, β, and $d\beta/dt$. Also, the isothermal heat of reaction, H_T, and total heat of reaction, H_U, will be given for each temperature.

Table A.1: Values of H_T and H_U for the six isothermal scans of Shell 1895/W.

Temperature (°C)	H_T	H_U
100	257.5	352.62
121	309.1	389.83
135	361.1	397.09
149	344.8	373.98
160	346.1	373.00
177	336.7	339.44

Table A.2: Experimental data for the 100 °C DSC scan.

Time (min.)	Area (J/g)	Beta	dBeta/dt
23.810	0.8216	0.00320	6.447E-6
35.720	2.4636	0.00960	1.080E-5
51.590	6.3886	0.02480	1.942E-5
63.500	10.6566	0.04140	2.586E-5
75.400	16.1236	0.06260	3.305E-5
86.310	22.6066	0.08780	4.097E-5
97.230	30.4716	0.11830	4.963E-5
108.140	39.3426	0.15280	5.612E-5
115.990	48.4246	0.18810	6.256E-5
127.980	58.6046	0.22760	6.901E-5
136.901	68.5656	0.26630	7.336E-5
145.840	79.0456	0.30700	7.767E-5
152.780	87.5536	0.34000	8.198E-5
159.730	96.3356	0.03741	8.198E-5
165.680	104.0956	0.04043	8.629E-5
173.620	114.6356	0.04452	8.847E-5
180.560	123.9456	0.48130	8.847E-5
188.500	134.4956	0.52230	8.629E-5
198.420	147.7156	0.57370	8.416E-5
208.340	160.6656	0.62390	8.198E-5
219.250	174.3656	0.67710	7.984E-5
231.160	188.4256	0.07317	7.118E-5
241.080	199.3256	0.77410	6.687E-5
251.000	209.1806	0.81240	6.256E-5
259.930	217.3426	0.84000	5.608E-5
268.860	224.6636	0.87250	4.959E-5
277.790	231.0146	0.89770	4.315E-5
289.690	237.7576	0.92330	3.235E-5
302.590	243.3136	0.94490	2.373E-5
317.470	247.8026	0.96230	1.511E-5
336.320	251.6406	0.97720	1.080E-5
365.090	254.9486	0.99010	6.485E-6
390.880	256.4806	0.99600	4.311E-6

Table A.3: Experimental data for the 121 °C DSC scan.

Time (min.)	Area (J/g)	Beta	dBeta/dt
9.52	2.149	0.0070	2.155E-5
19.04	7.453	0.0241	3.957E-5
26.98	15.152	0.0490	6.470E-5
34.92	26.552	0.0859	8.987E-5
42.06	40.572	0.1313	1.186E-4
49.20	57.902	0.1873	1.438E-4
52.38	66.689	0.2158	1.545E-4
54.76	73.688	0.2384	1.654E-4
58.73	86.058	0.2784	1.726E-4
62.69	99.118	0.3207	1.833E-4
66.66	112.768	0.3648	1.869E-4
71.43	129.488	0.4189	1.869E-4
76.19	146.388	0.4736	1.941E-4
80.95	163.138	0.5278	1.905E-4
87.30	184.628	0.5973	1.797E-4
93.65	204.638	0.6620	1.654E-4
100.79	225.078	0.7282	1.474E-4
109.52	246.828	0.7985	1.222E-4
123.01	273.148	0.8837	8.628E-5
132.53	286.188	0.9259	5.752E-5
141.26	294.199	0.9518	3.957E-5
149.20	299.161	0.9678	2.876E-5
157.14	302.599	0.9790	1.798E-5
165.07	304.929	0.9865	1.079E-5
177.77	307.329	0.9943	1.079E-5

C-3

Table A.4: Experimental data for the 135 °C DSC scan.

Time (min.)	Area (J/g)	Beta	dBeta/dt
6.45	5.041	0.0140	6.148E-5
12.41	16.381	0.0454	1.169E-4
18.36	34.901	0.0967	1.723E-4
23.32	56.431	0.1563	2.278E-4
27.29	77.741	0.2153	2.647E-5
30.26	95.841	0.2654	2.893E-4
33.24	115.431	0.3197	3.137E-4
36.21	136.021	0.3767	3.261E-4
39.19	157.021	0.4347	3.324E-4
42.66	181.341	0.5022	3.200E-4
46.63	207.961	0.5759	3.016E-4
50.60	232.551	0.6440	2.770E-4
54.57	254.621	0.7051	2.400E-4
59.53	278.441	0.7711	2.031E-4
64.49	298.441	0.8264	1.724E-4
70.44	317.831	0.8802	1.353E-4
76.39	332.471	0.9207	9.845E-5
83.83	344.501	0.9540	6.153E-5
91.77	351.855	0.9744	3.077E-5

Table A.5: Experimental data for the 149 °C DSC scan.

Time (min.)	Area (J/g)	Beta	dBeta/dt
3.33	4.391	0.0127	1.032E-4
6.19	12.548	0.0364	1.807E-4
9.04	25.628	0.0743	2.706E-4
11.42	40.838	0.1184	3.480E-4
13.80	60.128	0.1744	4.252E-4
15.23	73.588	0.2134	4.771E-4
16.66	88.308	0.2561	5.157E-4
18.09	104.058	0.3018	5.542E-4
19.52	120.588	0.3497	5.673E-4
20.95	137.518	0.3988	5.800E-4
22.38	154.488	0.4481	5.670E-4
23.80	171.208	0.4965	5.671E-4
25.71	192.568	0.5585	5.284E-4
28.09	217.098	0.6296	4.770E-4
30.95	242.798	0.7042	3.996E-4
34.52	269.208	0.7808	3.223E-4
38.09	290.080	0.8413	2.450E-4
42.87	311.148	0.9024	1.805E-4
47.61	325.508	0.9440	1.031E-4
51.50	332.988	0.9657	7.735E-5
54.83	337.184	0.9779	5.157E-5
57.89	339.825	0.9856	2.578E-5

Table A.6: Experimental data for the 160 °C DSC scan.

Time (min.)	Area (J/g)	Beta	dBeta/dt
1.99	3.069	0.0089	1.349E-4
3.77	10.443	0.0302	2.699E-4
5.36	21.033	0.0608	3.851E-4
7.15	37.863	0.1094	5.394E-4
8.34	52.033	0.1503	6.357E-4
9.53	68.403	0.1976	7.128E-4
10.72	86.693	0.2505	7.706E-4
11.91	106.403	0.3074	8.284E-4
13.10	126.913	0.3667	8.477E-4
14.29	147.523	0.4262	8.281E-4
15.48	167.613	0.4843	8.090E-4
16.67	186.673	0.5394	7.512E-4
18.26	209.963	0.6067	6.741E-4
20.24	235.273	0.6798	5.779E-4
22.23	256.523	0.7412	4.816E-4
24.61	277.383	0.8015	3.661E-4
26.99	294.133	0.8498	2.889E-4
29.96	310.643	0.8976	2.503E-4
33.93	326.373	0.9430	1.541E-4
38.10	336.543	0.9724	7.706E-5
41.27	340.982	0.9852	5.779E-5

Table A.7: Experimental data for the 177 °C DSC scan.

Time (min.)	Area (J/g)	Beta	dBeta/dt
1.19	5.098	0.0151	3.698E-4
1.90	11.767	0.0349	5.777E-4
2.50	19.510	0.0579	7.392E-4
3.09	29.337	0.0871	9.243E-4
3.57	38.713	0.1150	1.063E-3
4.16	52.273	0.1553	1.201E-3
4.76	67.683	0.2010	1.363E-3
5.36	84.633	0.2514	1.478E-3
5.83	99.003	0.2940	1.548E-3
6.43	117.533	0.3491	1.571E-3
7.02	136.173	0.4044	1.548E-3
7.62	154.383	0.4585	1.501E-3
8.33	175.063	0.5199	1.386E-3
9.16	197.003	0.5851	1.225E-3
10.0	216.323	0.6425	1.062E-3
11.07	237.353	0.7049	8.779E-4
12.50	259.683	0.7713	6.700E-4
14.28	280.483	0.8330	4.852E-4
16.66	299.803	0.8904	3.234E-4
18.56	310.663	0.9227	2.539E-4
20.47	318.606	0.9463	1.849E-4
22.49	324.656	0.9642	1.155E-4
24.76	329.231	0.9778	9.252E-5
27.26	332.521	0.9876	4.606E-5

BIBLIOGRAPHIC DATA SHEET	1. Report No. CCMS-93-15, VPI-E-93-09	2.	3. Recipient's Accession No.

4. Title and Subtitle
Verification of a Two-Dimensional Infiltration Model for the Resin Transfer Molding Process

5. Report Date
August 1993

6.

7. Author(s)
Vincent H. Hammond, Alfred C. Loos, H. Benson Dexter, Greg H. Hasko

8. Performing Organization Rept. No.
VPI-E-93-09, CCMS-93-15

9. Performing Organization Name and Address
Virginia Polytechnic Institute and State University
Department of Engineering Science and Mechanics
Blacksburg, VA 24061-0219

10. Project/Task/Work Unit No.

11. Contract/Grant No.
NAG-1-343

12. Sponsoring Organization Name and Address
Polymeric Materials Branch
National Aeronautics and Space Administration
Langley Research Center
Hampton, VA 23681-0001

13. Type of Report & Period Covered
Interim Report 94
August 1990 - August 1993

14.

15. Supplementary Notes

16. Abstract

A two-dimensional finite element model for the infiltration of a dry textile preform by an injected resin has been verified. The model, which is based on the finite element/control volume technique, determines the total infiltration time and the pressure increase at the mold inlet associated with the RTM process. Important input data for the model are the compaction and permeability behavior of the preform along with the kinetic and rheological behavior of the resin.

The compaction behavior for several textile preforms was determined by experimental methods. A power law regression model was used to relate fiber volume fraction to the applied compaction pressure. Results showed a large increase in fiber volume fraction with the initial application of pressure. However, as the maximum fiber volume fraction was approached, the amount of compaction pressure required to decrease the porosity of the preform rapidly increased.

Similarly, a power law regression model was used to relate permeability to the fiber volume fraction of the preform. Two methods were used to measure the permeability of the textile preform. The first, known as the steady state method, measures the permeability of a saturated preform under constant flow rate conditions. The second, denoted the advancing front method, determines the permeability of a dry preform to an infiltrating fluid. Water, corn oil, and an epoxy resin, Epon 815, were used to determine the effect of fluid type and viscosity on the steady state permeability behavior of the preform. Permeability values measured with the different fluids showed that fluid viscosity had no influence on the permeability behavior of 162 E-glass and TTI IM7/8HS preforms.

Permeabilities measured from steady state and advancing front experiments for the warp direction of 162 E-glass fabric were similar. This behavior was noticed for tests conducted with corn oil and Epon 815. Comparable behavior was observed for the warp direction of the TTI IM7/8HS preform and corn oil.

Mold filling and flow visualization experiments were performed to verify the analytical computer model. Frequency dependent electromagnetic sensors were used to monitor the resin flow front as a function of time. For the flow visualization tests, a video camera and high resolution tape recorder were used to record the experimental flow fronts. Comparisons between experimental and model predicted flow fronts agreed well for all tests. For the mold filling tests conducted at constant flow rate injection, the model was able to accurately predict the pressure increase at the mold inlet during the infiltration process. A kinetics model developed to predict the degree of cure as a function of time for the injected resin accurately calculated the increase in the degree of cure during the subsequent cure cycle.

17. Key Words and Document Analysis. **17a. Descriptors**
Resin transfer molding, permeability, flow visualization, textile composites, computer modeling

17b. Identifiers/Open-Ended Terms

17c. COSATI Field/Group

18. Availability Statement	19. Security Class (This Report) UNCLASSIFIED	21. No. of Pages 198
	20. Security Class (This Page) UNCLASSIFIED	22. Price

VIRGINIA TECH CENTER FOR COMPOSITE MATERIALS AND STRUCTURES

201 HANCOCK HALL, BLACKSBURG, VA 24061-0257 PHONE: (703) 231-4969 FAX: (703) 231-9452

The Center for Composite Materials and Structures (CCMS) is a supporting and coordinating organization for composite materials research and educational programs at Virginia Tech. The Center is designed to encourage and promote continued advances in the science and technology of composite materials and structures and to enhance the transfer and utilization of these new developments in industries and government organizations in Virginia, the nation, and the world.

The CCMS functions through an annually elected Administrative Board and a Director who is elected for a three-year term. Members of the Center include 46 faculty members in 11 academic departments in the College of Engineering and College of Arts and Sciences; 14 associate members; five technical staff members; approximately 130 graduate students; nine Industrial Affiliates representing a variety of composite materials interests at the national level; and government and industrial Research Sponsors currently supporting more than 55 research grants and contracts exceeding $7 million annually on composite materials and structures.

Specific objectives of the CCMS under this program include:

- providing a formal, interdisciplinary partnership between faculty, technical staff, and students who have active and complementary interests in composite materials and structures;
- providing leadership and coordination to enhance development and promote general success of research and educational activities in composite materials by shared responsibility, cooperative action, interdisciplinary support, and unified service;
- providing a means for the Virginia Tech composite materials and structures program to interact with university, state, national and international agencies, organizations, and industries; and
- promoting continued national and international recognition of the excellence in educational and research programs in composite materials and structures at Virginia Tech.

The CCMS has developed and operates a Composites Fabrication Laboratory to provide composite material fabrication capabilities. This facility is also available for conducting basic and applied research in composite processing and manufacturing. The Laboratory supports the educational and research programs of its membership. It also provides technical assistance to various research programs.

The educational mission of the CCMS is conducted by its members, in concert with the academic departments, at the undergraduate and graduate levels. This mission prepares students for careers in composites research, development, and application. More than 250 graduates of the Virginia Tech composites program have joined industries, government agencies, and universities. These individuals have provided significant advances to the science and technology of composite materials, and have attained positions of national leadership in the field.

The comprehensive research programs of the CCMS members cover the full range of composites science and technology. This includes the development and fabrication of new, improved constituents and material systems to the design and analysis of optimized composite components and structures. The most recent composites research accomplishments are reported in CCMS member's authored refereed papers and technical reports.

In addition to the CCMS Report Series, the CCMS administers:

- a vigorous Seminar Series featuring prominent speakers from leading laboratories and companies around the world, as well as CCMS students and faculty members;
- an Administrative Database to manage general information about the CCMS faculty and students, seminars, reports, alumni, company contacts, and Industrial Affiliates;
- a sesquiannual Technical Review/Workshop with the Center for Adhesive and Sealant Science; and
- the CCMS Bulletin, a bi-monthly newsletter of current events, notices, research opportunity announcements, and technical interest articles.

MEMBERS OF THE CENTER

Aerospace and Ocean Engineering

Raphael T. Haftka
Eric R. Johnson
Rakesh K. Kapania

Chemical Engineering

Donald G. Baird
Richey M. Davis
Garth L. Wilkes

Chemistry

John G. Dillard
James E. McGrath
Thomas C. Ward
James P. Wightman

Civil Engineering

Richard M. Barker
Richard E. Weyers

Electrical Engineering

Ioannis M. Besieris
Richard O. Claus
Douglas K. Lindner

Engineering Fundamentals

Deidre A. Hirschfeld

Engineering Science and Mechanics

David A. Dillard
John C. Duke, Jr.
Daniel Frederick
O. Hayden Griffin, Jr.
Zafer Gürdal

Engineering Science and Mechanics (continued)

Robert A. Heller
Edmund G. Henneke, II
Michael W. Hyer
Robert M. Jones
Ronald D. Kriz
Liviu Librescu
Alfred C. Loos
Don H. Morris
John Morton
Ali H. Nayfeh
J. N. Reddy
Kenneth L. Reifsnider
C. W. Smith
Wayne W. Stinchcomb
Surot Thangjitham

Industrial and Systems Engineering

Joel A. Nachlas

Materials Science & Engineering

Seshu B. Desu
D. P. H. Hasselman
Robert W. Hendricks
Ronald G. Kander

Mathematics

Werner E. Kohler

Mechanical Engineering

Charles J. Hurst
Charles E. Knight
Craig A. Rogers
Curtis H. Stern